Microwave to Telecom Wavelength Transduction

by

Hugh Ramp

A thesis submitted in partial fulfillment of the requirements for the degree of

Doctor of Philosophy

Department of Physics

University of Alberta

Abstract

Wavelength transduction of light, specifically between the microwave and telecom regimes, has received a great deal of attention from the cavity optomechanics community as a landmark application for optomechanical systems. Mechanical systems are uniquely suited to wavelength transduction, as photon-phonon momentum transfer allows mechanical motion to couple to light throughout the electromagnetic spectrum. The use of cavities to contain both electromagnetic and mechanical energy in resonators allows for enhanced interaction between light and matter, creating a viable path to high efficiency energy conversion.

For a device to act as an ideal transducer, it must satisfy three key parameters: low-noise, high-efficiency, and coherence. In this work we explore gallium arsenide optomechanical crystals as a candidate for microwave-to-telecom wavelength transduction, tackling the basic characteristics of the devices as optomechanical resonators and profiling their noise and efficiency characteristics.

To demonstrate transduction efficiency and coherence, we combine the optomechanical crystals with a 3D microwave cavity, and use the piezoelectric properties of gallium arsenide to couple the microwave mode to the gallium arsenide mechanical mode [1]. By injecting a signal into the microwave cavity and measuring it using the gallium arsenide telecom mode, we demonstrate microwave-to-telecom transduction and measure both the efficiency and the coherence of the transducer.

To demonstrate the low-noise capabilities, we use a dilution refrigerator to cool the optomechanical crystal to a temperature on the order of 10 mK, where we show that the mechanical mode is in the ground state with an average thermal phonon

population below one [2]. For the transduction protocol described in this thesis, a ground state mechanical resonator is critical to low-noise transduction, as thermal phonons are transduced in the same way as signal phonons and become added signal at the output of the transducer. We use these low-temperature measurements to estimate the number of added noise photons in a transduced signal.

These experiments are the foundation upon which future microwave-to-telecom transduction experiments in the Davis lab will be predicated. The methods described in this thesis, particularly the gigahertz optomechanics measurement techniques and apparatus, will act as a guide to future students who pursue the ultimate goal of transduction: the entanglement of superconducting qubits through a telecom link.

Preface

Many of the members of the (extended) Davis lab have contributed to my research, including, but not limited to, Bradley Hauer (BH), Callum Doolin (CD), Tommy Clark (TC), Paul Kim (PK), Allison MacDonald (AM), Clinton Potts (CP), Vaisakh Vadakkumbatt (VV), Fabien Souris (FS), Xavier Rojas (XR), Greg Popowich (GP), James Chaulk (JC), and the man himself, John Davis (JD).

Chapter 5 is based upon the publication H. Ramp, T. J. Clark, C. Doolin, B. D. Hauer, K. C. Balram, K. Srinivasan, and J. P. Davis, "Wavelength transduction from a 3D microwave cavity to telecom using piezoelectric optomechanical crystals", *Appl. Phys. Lett.* **116**, 174005 (2020). This work was assisted by the groundwork laid by TC regarding the use of 3D microwave cavities in the Davis lab, and the data collection was based on the code foundation built by CD. Noise isolation was achieved with the help of JC. The explicit derivation of the piezomechanical coupling rate was the combined effort of BH and myself.

The low temperature experiments in Chapter 6 are based on the publication H. Ramp, B. D. Hauer, K. C. Balram, T. J. Clark, K. Srinivasan, and J. P. Davis, "Elimination of Thermal Noise in Optomechanical Crystals", *Phys. Rev. Lett.*, **123**, 093603 (2018). This work was to some degree a continuation the work that had been accomplished by BD for silicon optomechanics. Much of the code that I used to run these experiments was built upon the foundation that CD had created. The homodyne measurement system was developed in our lab by TC. During these experiments, BD, TC, VV, FS, and especially GP and JD all assisted me in running and maintaining the dilution refrigerator. The electronics experience provided by JC was invaluable, as he built several amplifiers to make this experiment possible.

Yet even though light is so weightless
we have given its name to that condition,
it presses against what it falls on,
just as wind, which we cannot see,
pushes the arms of a mill.

Gene Wolfe, *Book of the New Sun* (1980-1983)

Acknowledgements

The work of this thesis represents a collaborative effort that spans not only members of the Davis group, which is the laboratory that I call my home, but also includes collaboration with a number of external groups, including Ray DeCorby's group in Electrical & Computer Engineering at the University of Alberta, and Kartik Srinivasan's group at the National Institute of Standards of Technology in Gaithersburg, Maryland. Most importantly, in addition to assembling an incredible team that has supported me in my research, John Davis has provided ideas, lasers, support, and enthusiasm. John is truly the heart of his lab, and I can never thank him enough for his part in my growth as a scientist and as a person. Without the help of all of these extraordinary scientists, this research would not have been possible.

A number of specific credits are due. First, Krishna Balram from the Srinivasan group fabricated the gallium arsenide optomechanical crystals that my thesis was predicated on. Together, Balram and Srinivasan helped guide me through the initial steps of making measurements of gigahertz-frequency mechanical modes on the devices they so generously gave us as part of our collaboration. Secondly, Mohammad Bitarafan and Clinton Potts from the DeCorby lab fabricated the buckled-dome Fabry Pérot cavities that are used to introduce optomechanics in Chapter 2. The 'domes' were my first undertaking as an experimental physicist, and I immensely value the experience I gained from working with them and the DeCorby lab.

Optomechanics research in the Davis lab would not be possible without the hard work of the graduate students who came before me. They not only built the foundation for the research that I have done, but also taught me how to do my own research in the lab. I owe many of my skills as an experimental physicist to

Allison, Brad, Callum, Greg, James and John. Broadening the umbrella, I would like to thank David Naylor and Mark Walton for beginning my career in physics research. A special thank-you goes to Hadi Kharaghani, who started my research career, taught me so much, and truly set me on my current path.

Finally, one of my mantras throughout graduate school is that it is not a sprint but a marathon, and the ones who make it to the end are not necessarily the smartest, but the most tenacious. Thus, I owe a great deal of thanks to the people who have kept me sane during the course of my graduate career: Mom, Dad, my sisters and their ridiculous number of pets; my many friends who have kept me active and social, and given me so many incredible memories and experiences; Ian and Asher, whom I have now lived with for seven years(!), and Ben and Alistair, whose tenure has been slightly shorter but no less significant; and my climbing partners who catch me when I fall, then tell me to get back on the wall. There are too many of you to name individually, but know that I wouldn't have made it without each and every one of you.

Contents

List of Tables

List of Figures

xvii

List of Symbols

Chapter 1

Introduction

1.1 A Motivation for Wavelength Transduction

Wavelength transduction is motivated primarily by the field of quantum computing. Qubits, which are quantum bits, store quantum information in a system where there are two possible configurations. A typical example is a two-level system with a ground and excited state where the superposition of the energy levels allows linear combination states to exist. This broad description of a qubit has allowed quantum computing technologies to evolve in a plethora of physical systems. Individual atoms emerged as an initial candidate for qubits, as their their electronic configuration can be manipulated into two level systems with energy separations in the visible to telecom bands. Atomic qubits benefit from indistinguishability—a quantum computer made from a single isotope of atom will have a set of identical qubits that all behave and interact in the same way. However, atomic quantum computers face a scalability challenge due to the delicate control required to trap many atoms in an optical lattice to form a large-scale quantum computer.

More recently, fabricated superconducting circuits have made an impact on the quantum computing field as "designer" qubits, which have characteristics that can be controlled through architecture and fabrication processes. Moreover, superconducting qubits are designed on-chip with operation frequencies in the GHz regime to allow for qubits to be interfaced with existing microwave-frequency electronics equipment. The result is a state-of-the-art quantum processor capable of entangling 53 individual qubits together to perform quantum algorithms faster than a classical computer [3].

The transmon qubit, which is a variation on a charge qubit, has become increasingly prevalent in the quantum computing industry as a basis for gate-model quantum computing, wherein quantum states are manipulated using quantum logic gates. In this architecture, each qubit is controlled by its own RF transmission line, which becomes prohibitive when scaling the quantum computer to many-qubit systems. Scalability issues arise in part due to sheer size of the transmission lines, but also because each line carries a heat load from room temperature to the millikelvin temperatures within the dilution refrigerator [4], which are required to operate the superconducting qubits in the thermal ground state. A potential way to circumvent size requirements is to build multiple quantum computers housed in separate dilution refrigerators, then network them using entanglement protocols. This draws direct comparison to classical grid computing, in which multiple computers are networked together to create a much more powerful supercomputer. On the largest of scales, this heralds the creation of a quantum internet.

Thermal noise is the primary obstacle that makes the realization of a quantum internet difficult. For communication to occur, the qubits are linked via superconducting circuitry, which allows them to exchange states via microwave photons that have energy equal to the transition energy between the qubit ground and excited states. These microwave transmission lines can also act as hosts to thermal noise; their average thermal photon population for a resonant mode at the transition energy is given by Bose-Einstein statistics to be

$$\bar{n}_{\mathrm{th}} = \frac{1}{e^{\frac{\hbar\omega}{k_{\mathrm{B}}T}} - 1},$$
(1.1)

where $\bar{n}_{\mathrm{th}}$ is the average thermal population, $\hbar\omega$ is the photon energy, which is given by Plank's constant multiplied by the photon frequency, and $k_{\mathrm{B}}T$ is the thermal energy, which is given by Boltzmann's constant k_{B}, multiplied by the bath temperature T. At the millikelvin temperatures of dilution refrigerators, the thermal population at the microwave photon and qubit transition frequency is far below one, implying the microwave superconducting circuitry is in the thermal ground state. However, when temperature increases, as it would if the microwave circuitry were extended outside of the dilution refrigerator, the transmission lines become increasingly populated with thermal photons. Thus, connecting two qubits

in separate dilution refrigerators via a room temperature microwave link results in the microwave photon carrying the quantum state being washed out by thousands of room temperature thermal photons.

The thermal photon population problem can only be solved in two ways: either create a millikelvin superconducting network [5], which would be impossibly costly over any significant distance, or increase the frequency of the messenger photon carrying the quantum state to an energy high enough that room temperature has a ground state thermal photon population. At room temperature, the telecom frequency $\omega/2\pi = 194.3$ THz is deep in the ground state, with an average thermal photon population $\bar{n}_{\text{th}} = 2 \times 10^{-14}$. As a result, transducing quantum information from a microwave photon to a telecom photon would allow for quantum communication channels between superconducting qubits in separated dilution refrigerators, allowing for entanglement of separated quantum processors, and ultimately the creation of a quantum internet.

Beyond the creation of the quantum internet, microwave to telecom transduction offers many other promising applications. Integrating microwave quantum technology with existing optical quantum technologies such as quantum memories [6], high-precision atomic clocks [7], and high-efficiency single photon detectors [8] would allow for the emergence of new hybrid quantum technology including microwave quantum radar [9] and microwave quantum repeaters [10]. As such, the creation of a microwave-to-telecom transducer is of paramount importance to quantum technology research and application.

1.2   Roads to Wavelength Transduction

Microwave-to-telecom wavelength transduction has now been established as a crucial part of the developing quantum toolbox, which will allow for the development of new technologies within the broad quantum community. As such, the task of transduction has been approached using a wide array of physical systems and techniques [11, 12]. In this thesis we choose to approach the problem using a piezo-optomechanical system, in which microwaves are transduced into telecom photons via a mechanical intermediary. This draws upon the optomechanics expertise that

3

has been established in the Davis lab, and links it to the 3D-microwave cavity platform that was developed concurrently by other students in the Davis lab. The rest of this thesis will develop the ideas of piezo-optomechanics in detail. Here we will take a brief moment to survey other approaches to microwave-to-telecom transduction to serve as context.

Our survey begins with an industry standard for microwave-to-telecom transduction, where non-linear electro-optic materials such as lithium niobate are used in electro-optic phase modulators to convert microwave tones into optical sidebands. We will later make extensive use of electro-optic modulators for calibration purposes, but recognise that commercially available modulators have transduction efficiencies ($\eta \approx 10^{-7}$ [12]) too low for quantum state transduction [13]. State-of-the-art research into cavity enhanced electro-optic modulators have demonstrated significant improvements in this respect reaching efficiencies of $\eta = 0.02$ [14–16]. Other options include using Rydberg transitions in cold atoms [17–19], or using magnons [20], which are collective spin excitations in a magnetic material, as an intermediary between microwave and telecom light. The majority of transduction experiments, however, use a mechanical intermediary, which opens a wide array of approaches to microwave-to-telecom transduction due to the many ways of coupling electromagnetic energy (light) to mechanical energy (motion). In the next chapter we will begin our introduction to light-matter interaction, which is described by the field of optomechanics. In doing so, we will continue our survey of wavelength transduction in the context of mechanical mediators between microwave and telecom light.

In the chapters that follow, we will use the theoretical understanding of optomechanics developed in Chapter 2 to characterize the devices at room temperature in Chapter 3, where we will further describe the setup created for measuring the high-frequency mechanical modes of our optomechanical devices. Chapter 4 then introduces the piezo-optomechanical theory that will be used for the realization of microwave-to-telecom transduction [1] in Chapter 5. In Chapter 6, the tansduction device used in this thesis is cooled to millikelvin temperatures in a dilution refrigerator in order to explore the low-temperature optomechanical characteristics [2].

Chapter 2

Optomechanics

2.1 Introduction to Optomechanics

The term optomechanics is often used as a broad description of the interactions between two harmonic oscillators: one mechanical, which stores energy in the form of vibrational motion (phonons), and one electromagnetic, which stores energy in the form of light (photons). In this thesis we separate the unified optomechanics into three major subfields:

1. Optomechanics (infrared and visible optomechanics)

2. Electromechanics (microwave optomechanics)

3. Piezomechanics (microwave optomechanics using piezoelectric interaction)

The first subfield of unified optomechanics describes the quadratic interaction of mechanical resonators and optical cavities populated with light from lasers with wavelengths between ~ 780 nm and ~ 1630 nm. As the origin of the broad field of optomechanics, this subfield is simply referred to eponymously, both in literature and in this thesis. For mechanically-mediated microwave-to-telecom transduction, the quadratic interaction described by optomechanics is always used to convert energy between mechanical motion and telecom light. In contrast, the interactions used to convert energy between microwave light and mechanical motion are more diverse.

Electromechanics takes advantage of the same quadratic interaction as optomechanics, but makes use of an LC-microwave resonator instead of an optical

cavity to store microwave electromagnetic energy. These LC resonators often take the form of on-chip circuitry, where a vibrating membrane forms one plate of the LC resonator capacitor [21]. These membranes typically have low-frequency mechanical modes, which cause them to have a significant thermal phonon population even at dilution refrigerator temperatures [22]. Electro-optomechanics, which uses a mechanical resonator quadratically coupled to both microwave and telecom light has been used as a vehicle to achieve high-efficiency wavelength transduction [23–25]. The thermal population of the mechanical resonator, however, resulted in thermal noise entering the transduced signal.

Piezomechanical theory is similar to electromechanics, in that it describes the coupling between microwaves (both directly and through microwave resonators) and mechanical resonators. The piezomechanical interaction however is linear in nature, and must be treated differently as a result. We will explore the piezomechanical interaction in Chapter 4, and a complete piezo-(telecom)-optomechanical picture in Chapter 5. Here we note that piezo-optomechanics is by far the most thoroughly investigated method of transducing microwave light to the telecom domain. The most common example of piezo-optomechanics uses the piezoelectric effect to generate surface acoustic waves that interact with the mechanical mode of an optomechanical device [26–31]. In this thesis, however, we forgo the use of surface acoustic waves and choose to directly drive the mechanical mode with an electric field generated by a 3D microwave cavity [1]. In both cases, the piezomechanical interaction allows for more straightforward integration of high-frequency mechanical resonators, which implies reduced thermal phonon populations and therefore reduced thermal noise in the transduced signal. We will fully explore piezomechanical coupling using 3D microwave cavities in Chapter 5, where we use it to realize microwave-to-telecom transduction.

In this Chapter, we will introduce the theory of quadratically coupled harmonic oscillators, which mathematically describes both optomechanics and electromechanics. The example used to illustrate the interactions, however, will be specific to an optomechanical device that is illuminated using a coherent, monochromatic source—an infrared laser. We begin with an independent treatment of both the mechanical and optical resonators prior to developing the theory of the

optomechanical interaction. Finally, we will describe the optomechanical crystal; a device created to harness the optomechanical interaction.

2.2 Mechanical Resonators

In this section we consider a simple harmonic oscillator in the form of a mass-spring system. Although motion in optomechanics can take many physical forms, it can generally be treated as a point-like effective mass m_{eff} which obeys Hooke's law:

$$F = -kx, \tag{2.1}$$

where F is the force exerted on the mass by a spring with spring constant k when the mass is displaced a distance x from its equilibrium position. The resonance frequency of the mechanical motion is determined by solving the second order differential equation attained using Newton's second law $F = m\ddot{x}$,

$$\frac{d^2}{dt^2}x = -\frac{k}{m_{\text{eff}}}x, \tag{2.2}$$

which has a solution $x = x_0 \cos(\omega_{\text{m}}t)$ with a resonant frequency $\omega_{\text{m}} = \sqrt{k/m_{\text{eff}}}$. The classical mechanics approach further allows for the calculation of the kinetic energy

$$T = \frac{p^2}{2m_{\text{eff}}}, \tag{2.3}$$

and the potential energy

$$U = \frac{1}{2}m_{\text{eff}}\omega_{\text{m}}^2 x^2. \tag{2.4}$$

The Hamiltonian represents the total energy in the system, and hence we combine the kinetic and potential energy to write the classical mechanical Hamiltonian

$$\mathcal{H}_{\text{mech}} = T + U = \frac{p^2}{2m_{\text{eff}}} + \frac{m_{\text{eff}}\omega_{\text{m}}^2 x^2}{2}. \tag{2.5}$$

We now move to a quantum mechanical description, where position and momentum are treated as operators $\hat{x}(t)$ and $\hat{p}(t)$. Second quantization allows for the motion to be characterized in terms of boson creation and annihilation

operators

$$\hat{b}^\dagger(t) = \frac{1}{2x_{\text{zpf}}} \left(\hat{x}(t) + \frac{i}{\omega_{\text{m}} m_{\text{eff}}} \hat{p}(t) \right) \tag{2.6}$$

$$\hat{b}(t) = \frac{1}{2x_{\text{zpf}}} \left(\hat{x}(t) - \frac{i}{\omega_{\text{m}} m_{\text{eff}}} \hat{p}(t) \right), \tag{2.7}$$

where $x_{\text{zpf}} = \sqrt{\hbar/(2m_{\text{eff}}\omega_{\text{m}})}$ is the mechanical zero-point fluctuation amplitude. The operators $\hat{b}(t)$ and $\hat{b}^\dagger(t)$ are used to rewrite the Hamiltonian, at which point we arrive at the Hamiltonian for the quantum harmonic oscillator,

$$\mathcal{H}_{\text{mech}} = \hbar\omega_{\text{m}} \left(\hat{b}^\dagger\hat{b} + \frac{1}{2} \right), \tag{2.8}$$

where the time dependence of the phonon operators necessarily cancels out such that the Hamiltonian is time independent. We can recover information about the time dependence of the phonon operators using Heisenberg's equation,

$$\dot{\hat{O}} = \frac{i}{\hbar} \left[\mathcal{H}, \hat{O} \right], \tag{2.9}$$

to develop an equation of motion for the quantum harmonic oscillator. The time evolution of the phonon annihilation operator is

$$\dot{\hat{b}}(t) = \frac{i}{\hbar} \left[\mathcal{H}_{\text{mech}}, \hat{b}(t) \right] \tag{2.10}$$

$$= -i\omega_{\text{m}}\hat{b}(t). \tag{2.11}$$

The solution to this differential equation is the exponential function, where $\hat{b}(t) = \hat{b}e^{-i\omega_{\text{m}}t}$.

The Hamiltonian describes the resonator as a completely closed system. Damping and noise terms can be attained by considering the mechanical mode as being coupled to an infinite bath of harmonic oscillators [32]. A more complete equation of motion for the mechanical mode is

$$\dot{\hat{b}}(t) = -i\omega_{\text{m}}\hat{b}(t) - \frac{\Gamma_{\text{m}}}{2}\hat{b}(t) + \sqrt{\Gamma_{\text{m}}}\hat{b}_{\text{in}}(t), \tag{2.12}$$

which describes the time-domain dynamics of phonons in a mechanical mode coupled to an external environment. The mechanical damping rate Γ_{m} describes the rate at which phonons are exchanged with the environment, whether it be the loss of phonons from the resonator to the environment $(\Gamma_{\text{m}}/2)\hat{b}(t)$, or the mechanical

mode being driven by thermal forces $\sqrt{\Gamma_{\rm m}}\hat{b}_{\rm in}(t)$, where the rate at which thermal phonons are incident on the mechanical mode is $\langle \hat{b}_{\rm in}^{\dagger}(t')\hat{b}_{\rm in}(t)\rangle = \bar{n}_{\rm th}\delta(t'-t)$. The coefficients in these terms represent our convention of describing the damping rate in terms of its full-width half-max linewidth in frequency space, hence $\Gamma_{\rm m}$ represents a phonon loss rate and $\Gamma_{\rm m}/2$ describes an amplitude damping rate [33]. Lastly, the mechanical damping rate and frequency can be combined into a mechanical quality factor $Q_{\rm m} = \omega_{\rm m}/\Gamma_{\rm m}$, which further describes the ratio of energy stored in the mechanical mode to energy lost to the environment. In this thesis, and in general for optomechanical devices, the mechanical modes exist in the "high-Q" regime with $Q_{\rm m} \gg 1$.

The mechanical Hamiltonian Eqn. (2.8) and equation of motion Eqn. (2.12) provide a basis for describing mechanical motion, which will later be expanded for a more complete description of optomechanics. Here we note again that the frequency $\omega_{\rm m}$ determines the number of thermal phonons for a given temperature as determined by Bose-Einstein statistics,

$$\bar{n}_{\rm th} = \frac{1}{e^{\frac{\hbar\omega_{\rm m}}{k_{\rm B}T}} - 1}, \tag{2.13}$$

which means that for any particular temperature, a high-frequency mechanical resonator has less thermal noise. This plays an important role for mechanically mediated wavelength transducers, as limiting thermal motion in the device directly limits the amount of noise added to the signal by the transducer.

2.3   Optical Resonators

The prototypical optical resonator is the Fabry Pérot cavity, which consists of two facing mirrors set some distance L apart. Light within the cavity is trapped between the mirrors to create a standing wave with the resonance condition [33]

$$\omega_k = k\frac{\pi c}{nL}, \tag{2.14}$$

where k is the mode order, ω_k is the mode frequency, n is the material index of refraction, and $c = \sqrt{1/\mu_0\epsilon_0}$ is the speed of light in vacuum, which is defined by the vacuum permitivity ϵ_0 and permeability μ_0. If the optical cavity is filled
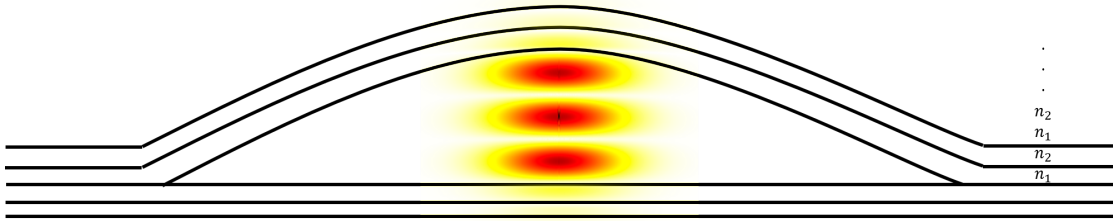
Figure 2.1: Buckled-dome Fabry Pérot cavity schematic including the simulated electric field. In this structure, the mirrors are distributed Bragg reflectors, which are composed of multiple layers of material with periodically varying index of refraction n_1 and n_2. At each material interface (black lines), the index difference results in an impedance mismatch which causes reflection. By tailoring the thickness of the material layers, the reflections can be tuned to constructively interfere, which results in high reflectivity mirrors. Between the mirrors, three red ovals represent high-intensity anti-nodes of the optical mode.

with material instead of air or vacuum, then n is the index of refraction of that material, and c/n is the speed of light in the cavity medium. Figure 2.1 depicts a buckled-dome Fabry Pérot cavity [34–36] as an example, where the $L \approx 2.5$ µm tall cavity hosts a $k = 3$ order optical mode for photons near $\lambda_3 = 2\pi c/\omega_3 = 1550$ nm.

The optical field inside the cavity can be understood from the starting point of the quantization of the electric and magnetic fields in terms of the creation and annihilation operators $\hat{a}^\dagger(t) = \hat{a}^\dagger e^{i\omega t}$, $\hat{a}(t) = \hat{a} e^{-i\omega t}$. The electric field confined in the cavity takes the form of a plane wave[1] [32]

$$\mathbf{E}(\mathbf{r}, t) = i \sum_k \hat{a}_k e^{-i\omega_k t} \mathcal{E}_k(\mathbf{r}) - \hat{a}_k^\dagger e^{i\omega_k t} \mathcal{E}_k^*(\mathbf{r}), \qquad (2.15)$$

where the electric field amplitude $\mathcal{E}_k(\mathbf{r}) = \sqrt{\frac{\hbar \omega_k}{2\epsilon_0}} \mathbf{u}_k(\mathbf{r})$ is defined using a set of orthonormal vectors $\mathbf{u}_k(\mathbf{r}) \propto e^{i\mathbf{k}\cdot\mathbf{r}}$ with wavevector $\mathbf{k}$ that satisfy the boundary conditions of the cavity. The magnetic field modes can be written in terms of the electric field modes,

$$\mathbf{B}_k(\mathbf{r}, t) = \frac{1}{\omega_k} \mathbf{k} \times \mathbf{E}_k(\mathbf{r}, t), \qquad (2.16)$$

---

[1]The dome-shape of the top mirror causes the optical modes of the cavity to be described by Hermite-Gaussian modes. By considering the solutions of a plane wave we neglect the spacial dimensions in the plane of the mirrors.

such that

$$\mathbf{B}(\mathbf{r}, t) = i \sum_k \hat{a}_k e^{-i\omega_k t} \mathcal{B}_k(\mathbf{r}) - \hat{a}_k^\dagger e^{i\omega_k t} \mathcal{B}_k^*(\mathbf{r}), \tag{2.17}$$

where the magnetic field amplitude is $\mathcal{B}_k(\mathbf{r}) = \sqrt{\frac{\hbar}{2\omega_k \epsilon_0}}(\mathbf{k} \times \mathbf{u}(\mathbf{r}))$. With both the electric and magnetic field written in quantized forms, the next step is to write the total electromagnetic field energy [32]

$$U = \int_V \left(\frac{\epsilon_0 \mathbf{E}^2}{2} + \frac{\mathbf{B}^2}{2\mu_0} \right) d\mathbf{r}^3. \tag{2.18}$$

Using the orthogonality of the position vectors $\int_V \mathbf{u}_k^*(\mathbf{r})\mathbf{u}_{k'}(\mathbf{r})d\mathbf{r}^3 = \delta_{k,k'}$ to carry out the volume integration, the Hamiltonian can be written as that of a quantum harmonic oscillator,

$$\mathcal{H}_{\mathrm{opt}} = \sum_k \hbar\omega_k \left(\hat{a}_k^\dagger \hat{a}_k + \frac{1}{2} \right). \tag{2.19}$$

From the Hamiltonian, we use Heisenberg's equation of motion, Eqn. (2.9), to reveal the dynamics of a chosen optical mode at frequency ω_{c}:

$$\dot{\hat{a}}(t) = \frac{i}{\hbar} [\mathcal{H}_{\mathrm{opt}}, \hat{a}(t)] \tag{2.20}$$

$$= -i\omega_{\mathrm{c}}\hat{a}(t). \tag{2.21}$$

Similar to the case of the mechanical equation of motion, the optical equation of motion now describes a closed system, with no coupling to the outside world. To include coupling to the external environment, which allows for photon loss, and to add an external driving laser, we turn to input-output theory [32, 33], which again provides a more complete equation of motion:

$$\dot{\hat{a}}(t) = -i\omega_{\mathrm{c}}\hat{a}(t) - \frac{\kappa}{2}\hat{a}(t) - \sqrt{\kappa_{\mathrm{e}}}\hat{a}_{\mathrm{in}}(t). \tag{2.22}$$

The optical equation of motion bears close similarity to the mechanical equation of motion Eqn. (2.12), which is to be expected as we describe both systems as quantum harmonic oscillators. The exception to the similarities is that the total optical cavity decay rate $\kappa = \kappa_0 + \kappa_{\mathrm{e}}$ has been partitioned into an external decay rate κ_{e}, which represents losses to an input/output channel such as an optical fiber, and an internal decay rate κ_0, which represents other sources of loss to the

environment, such as photon absorption in the mirrors or scattering due to mirror surface roughness. The need to distinguish between external and internal decay rates is a result of $\hat{a}_{\text{in}}(t)$ being used as a non-thermal driving term which populates the optical cavity with photons from a laser. This causes κ_{e} to act as a coupling term to the measurement system, and κ_0 to act as a true loss rate for the optical cavity. The distinction between channel and environmental losses will be further elucidated experimentally in Chapter 3.

The input field $\hat{a}_{\text{in}}(t)$ has a frequency ω_ℓ set by the external laser. The resulting field inside the optical cavity must also be at the same frequency, with a possible phase offset. This can be made explicit by separating the laser time dependence by setting $\hat{a}(t) \rightarrow \hat{a}(t)e^{-i\omega_\ell t}$, $\hat{a}_{\text{in}}(t) \rightarrow \hat{a}_{\text{in}}e^{-i\omega_\ell t}$. Applying the chain rule and rearranging, the equation of motion can be written in a frame of reference that rotates with the laser frequency,

$$\dot{\hat{a}}(t) = -i\Delta\hat{a}(t) - \frac{\kappa}{2}\hat{a}(t) - \sqrt{\kappa_{\text{e}}}\hat{a}_{\text{in}}, \tag{2.23}$$

where $\Delta = \omega_{\text{c}} - \omega_\ell$ is the laser detuning, and $\hat{a}_{\text{in}}$ is stationary for a continuous laser input. It is important to emphasize that the cavity photon operator $\hat{a}(t)$ is still time-dependent, unless the optical mode is in equilibrium—by transitioning to the rotating frame, we have simply removed the laser time dependence. To completely remove time dependence we set $\dot{\hat{a}}(t) = 0$, which allows us to determine the cavity optical field in the stationary state,

$$\hat{a} = -\frac{\sqrt{\kappa_{\text{e}}}\hat{a}_{\text{in}}}{i\Delta + \kappa/2}. \tag{2.24}$$

The expectation value of the intensity allows for the calculation of the average number of photons in the cavity

$$\bar{n}_{\text{cav}} = \langle\hat{a}^\dagger\hat{a}\rangle = \frac{\kappa_{\text{e}}|\hat{a}_{\text{in}}|^2}{\Delta^2 + \kappa^2/4}, \tag{2.25}$$

where $|\hat{a}_{\text{in}}|^2 = \frac{P_\ell}{\hbar\omega_\ell}$ is the photon flux of a laser with power power P_ℓ.

2.4 Optomechanical Interaction

Coupling between the optical and mechanical modes is achieved dispersively, where the mechanical motion shifts the optical resonance frequency [37]. Returning

to the optical resonance condition Eqn. 2.14, there are two ways the resonance frequency can change: the length of the cavity can change, which is known as moving boundary coupling [38]; or the optical cavity index of refraction n can change, which typically occurs due to motion-induced strain within a material that exhibits the photoelastic effect [39, 40].

Let us first use Fig. 2.1 to examine the consequences of a moving mirror. In this case, the cavity length is a function of the top mirror position x, such that the resonance condition Eqn. (2.14) becomes

$$\omega(x) = \frac{\pi c}{nL(x)}, \tag{2.26}$$

where we have chosen to focus on a single optical mode, which now has frequency dependence on the mirror position through $L(x)$. Then, taking the Taylor expansion near the equilibrium position $L(0)$, the cavity frequency is shifted from the equilibrium resonance frequency ω_c to,

$$\omega_c(x) \approx \omega_c + \frac{d\omega_c}{dx}x. \tag{2.27}$$

Where the Taylor expansion has been truncated to first order such that the resonance frequency is linearly displaced by the mirror position x. Here we take the opportunity to normalize the mirror position by the zero-point fluctuations, and subsequently normalize the frequency-shift-per-displacement scaling factor, such that

$$\omega_c(x) \approx \omega_c + g_0 \frac{x}{x_{\mathrm{zpf}}}, \tag{2.28}$$

where $g_0 = x_{\mathrm{zpf}} \frac{d\omega_c}{dx}$ is the single-photon single-phonon optomechanical coupling, which represents the rate at which energy is exchanged between photons in the optical mode and phonons in the mechanical mode.

We have developed the optomechanical coupling from the idea of a moving mirror changing the length of the cavity, but changing the index of refraction of the cavity medium produces the same effect, which occurs most commonly due to material photoelasticity. It is sometimes useful to distinguish between the moving boundary coupling g_{mb} and the photoelastic coupling g_{pe}. These effects add in series such that $g_0 = g_{\mathrm{mb}} + g_{\mathrm{pe}}$. Depending on the material and geometry of the cavity, the couplings can either compete or cooperate [40].

13

Transitioning to the Hamiltonian picture, the combined optical and mechanical systems can be written as the sum of each component,

$$\mathcal{H} = \mathcal{H}_{\text{opt}} + \mathcal{H}_{\text{mech}} \tag{2.29}$$

$$= \hbar\omega_{\text{c}}(x)\hat{a}^\dagger\hat{a} + \hbar\omega_{\text{m}}\hat{b}^\dagger\hat{b}, \tag{2.30}$$

where the zero-point contributions of $\frac{1}{2}$ have been dropped for simplicity. By expanding the cavity frequency using Eqn. (2.28), and using Eqns. (2.6, 2.7) to recognise $\hat{x} = x_{\text{zpf}}(\hat{b}^\dagger + \hat{b})$, the optomechanical Hamiltonian is

$$\mathcal{H} = \hbar\omega_{\text{c}}\hat{a}^\dagger\hat{a} + \hbar g_0\hat{a}^\dagger\hat{a}(\hat{b}^\dagger + \hat{b}) + \hbar\omega_{\text{m}}\hat{b}^\dagger\hat{b}. \tag{2.31}$$

The interaction component of the Hamiltonian represents a quadratic interaction between the optical and mechanical modes where the intensity of the light stored in the optical mode interacts with the position of the mirror.

The equations of motion can now be derived for both the optical and mechanical modes. As we have previously shown in Eqns. (2.12, 2.23), the equations of motion are presented in a frame where the optics rotate with the laser and with added terms representing bath coupling. We now further include an optomechanical coupling term:

$$\dot{\hat{a}}(t) = -i\Delta\hat{a}(t) - ig_0\hat{a}(t)\left(\hat{b}^\dagger(t) + \hat{b}(t)\right) - \frac{\kappa}{2}\hat{a}(t) - \sqrt{\kappa_{\text{e}}}\hat{a}_{\text{in}}, \tag{2.32}$$

$$\dot{\hat{b}}(t) = -i\omega_{\text{m}}\hat{b}(t) - ig_0\hat{a}^\dagger(t)\hat{a}(t) - \frac{\Gamma_{\text{m}}}{2}\hat{b}(t) - \sqrt{\Gamma_{\text{m}}}\hat{b}_{\text{in}}(t). \tag{2.33}$$

The equations of motion can be made more tractable by linearizing the optical field as an average amplitude $\bar{\alpha}$ with fluctuations $\delta\hat{a}(t)$, which is in general is a good approximation for optical cavities driven using a laser. This separation allows for Eqn. (2.32) to be represented as a steady state portion that can be used to recover Eqn. (2.24) as well as an equation of motion for fluctuations in the optical field. The linearized optical equation of motion is then

$$\delta\dot{\hat{a}}(t) = -i\Delta\delta\hat{a}(t) - ig_0\bar{\alpha}\left(\hat{b}^\dagger(t) + \hat{b}(t)\right) - \frac{\kappa}{2}\delta\hat{a}(t) - \sqrt{\kappa_{\text{e}}}\delta\hat{a}_{\text{in}}, \tag{2.34}$$

where we have neglected the second-order fluctuation term $-g_0\delta\hat{a}(t)\left(\hat{b}^\dagger(t) + \hat{b}(t)\right)$. Notably, the interaction term in Eqn. (2.34) presents evidence that the optomechanical interaction is linearly enhanced by the steady-state optical field amplitude $\bar{\alpha}$

due to the quadratic nature of the interaction. As a result, we consider the number of cavity photons to be the steady state populations $\bar{n}_{\text{cav}} = |\bar{\alpha}|^2$, which makes it clear that the exchange of energy between the optical and mechanical modes is proportional to $\sqrt{\bar{n}_{\text{cav}}}$. One way of characterizing this coupling is by defining a dimensionless parameter known as the optomechanical cooperativity

$$C = \frac{4g_0^2 \bar{n}_{\text{cav}}}{\kappa \Gamma_{\text{m}}}, \tag{2.35}$$

which compares the cavity enhanced rate of energy exchange $g_0 \sqrt{\bar{n}_{\text{cav}}}$ to the rate of energy loss in the optical (κ) and mechanical (Γ_{m}) modes. That is, a cooperativity greater than one implies energy will be preferentially exchanged between modes instead of lost to the respective mode baths. Obtaining $C > 1$ is important for wavelength transduction applications, as it implies that information, in the form of photons and phonons, is preferentially moved between the mechanical and optical modes instead of being lost to the environment. From this a straightforward prediction is that high-efficiency transduction requires high cooperativity.

The equations of motion for the optical fluctuations and the mechanical vibrations are most easily solved using their frequency-space representations found using the Fourier transform,

$$\delta\hat{a}(\omega) = -\frac{ig_0\bar{\alpha}\left(\hat{b}^\dagger(\omega) + \hat{b}(\omega)\right) + \sqrt{\kappa_e}\delta\hat{a}_{\text{in}}(\omega)}{\chi_{\text{a}}^{-1}(\omega)}, \tag{2.36}$$

$$\hat{b}(\omega) = -\frac{ig_0\bar{\alpha}\left(\delta\hat{a}^\dagger(\omega) + \delta\hat{a}(\omega)\right) + \sqrt{\Gamma_{\text{m}}}\hat{b}_{\text{in}}(\omega)}{\chi_{\text{b}}^{-1}(\omega)}, \tag{2.37}$$

where the optical and mechanical susceptibilities are respectively

$$\chi_{\text{a}}(\omega) = \frac{1}{i(\Delta - \omega) + \frac{\kappa}{2}}, \tag{2.38}$$

$$\chi_{\text{b}}(\omega) = \frac{1}{i(\omega_{\text{m}} - \omega) + \frac{\Gamma_{\text{m}}}{2}}. \tag{2.39}$$

Together, these coupled equations are used to describe many optomechanical interactions, including, as we will see later, wavelength transduction. For now, we investigate how the population of photons in the optical mode affects the mechanical mode.

2.4.1 Dynamical Backaction

In the opening pages of this thesis we quote Gene Wolfe's remark on how light carries momentum, which causes it to exert force when it collides with matter. This is especially true in optomechanics, where the accumulation of optical fields results in dynamical backaction, which affects the motion of the mechanics. To describe this optomechanical effect we turn to solving Eqns. (2.36, 2.37) for $\hat{b}^\dagger(\omega) + \hat{b}(\omega)$, which results in

$$\hat{b}^\dagger(\omega) + \hat{b}(\omega) = -\frac{ig_0\bar{\alpha}\sqrt{\kappa_{\mathrm{e}}}\left(\chi_{\mathrm{a}}^\dagger(-\omega)\delta\hat{a}_{\mathrm{in}}^\dagger - \chi_{\mathrm{a}}(\omega)\delta\hat{a}_{\mathrm{in}}\right) + \sqrt{\Gamma_{\mathrm{m}}}\frac{\chi_{\mathrm{b}}^\dagger(-\omega)^\dagger\hat{b}_{\mathrm{in}}^\dagger - \chi_{\mathrm{b}}(\omega)\hat{b}_{\mathrm{in}}}{\chi_{\mathrm{b}}^\dagger(-\omega)+\chi_{\mathrm{b}}(\omega)}}{\left(\chi_{\mathrm{b}}^\dagger(-\omega) + \chi_{\mathrm{b}}(\omega)\right)^{-1} + \Sigma(\omega)}.$$

(2.40)

Here we have defined the self energy, which arises from backaction, as

$$\Sigma(\omega) = -ig_0^2|\bar{\alpha}|^2\left(\chi_{\mathrm{a}}^\dagger(-\omega) - \chi_{\mathrm{a}}(\omega)\right),$$

(2.41)

and further note that the denominator of Eqn. (2.40) represents an effective mechanical susceptibility. By inspection of Eqn. (2.39), we can identify that $\mathrm{Im}\{\Sigma(\omega_{\mathrm{m}})\}$ shifts the mechanical damping rate [33],

$$\Gamma_{\mathrm{OM}} = -\frac{g_0^2|\bar{\alpha}|^2\kappa}{2}\left(\frac{1}{(\Delta + \omega_{\mathrm{m}})^2 + \kappa^2/4} - \frac{1}{(\Delta - \omega_{\mathrm{m}})^2 + \kappa^2/4}\right),$$

(2.42)

whereas $\mathrm{Re}\{\Sigma(\omega_{\mathrm{m}})\}$ shifts the mechanical frequency

$$\delta\omega_{\mathrm{m}} = -g_0^2|\bar{\alpha}|^2\left(\frac{\Delta + \omega_{\mathrm{m}}}{(\Delta + \omega_{\mathrm{m}})^2 + \kappa^2/4} + \frac{\Delta - \omega_{\mathrm{m}}}{(\Delta - \omega_{\mathrm{m}})^2 + \kappa^2/4}\right).$$

(2.43)

These shifts are recognised as the detuning-dependent optomechanical damping Γ_{OM} and optomechanical spring $\delta\omega_{\mathrm{m}}$ effects.

For microwave to telecom transduction, the optomechanical damping effect is of interest as it implies the existence of laser-induced damping. In the resolved sideband regime, where $\omega_{\mathrm{m}} \gg \kappa$, the total mechanical damping $\Gamma = \Gamma_{\mathrm{m}} + \Gamma_{\mathrm{OM}}$ increases to a maximum when the laser is red-detuned by the mechanical frequency $\Delta = \omega_{\mathrm{m}}$. At this point, an anti-Stokes scattering process is enhanced, where the phonon energy is absorbed by a laser drive photon to promote it into the optical resonance. This is effectively a cooling operation [41], which enhances the removal

of phonons from the mechanical resonator. In the case of transduction, it can be used to either pre-cool the mechanical mode, or to directly remove signal phonons as part of the transduction process [23–31].

Although the derivations of this chapter have thus far been made with a movable-mirror Fabry Pérot cavity in mind, the equations hold for a variety of optomechanical devices, including drum and trampoline resonators in optical cavities [23–25, 42, 43], optical microdisks of various designs [44–48], electromechanical LC resonators with mechanically dependent capacitance [21, 22, 49, 50], and optomechanical crystals [26–31, 40, 51–53], which are devices tailored to facilitating the optomechanical interaction and the device used for the experiments in this thesis. In the following section, we will develop the concept of the optomechanical crystal.

2.5 Optomechanical Crystals

Optomechanical crystals are complex devices built upon the principles of both photonic crystals [54] and phononic crystals [55]. Originally designed in the Painter lab [56], they rely on periodic (crystalline) structure to control optical and mechanical dispersion within the material. As a result, optomechanical crystals are well described by Bloch's theorem [57], which describes a plane wave such as the electric field described in Eqn. (2.15), modulated by a periodic potential $\psi(\mathbf{r})$.

In this section we will construct the theory of an optomechanical crystal from the starting point of a 1D waveguide, with the understanding that the principles can be naturally extended to a 2D slab [58]. Conceptually, a 3D bulk optomechanical crystal can also be envisioned since 3D structures are capable of acting both as photonic [59] and phononic [60] crystals, but fabrication limitations makes achieving both properties simultaneously difficult.

2.5.1 Waveguide confinement

Consider Fig. 2.2(a), in which a rectangular beam of material with index n_1 is suspended in air or vacuum with index n_2. At the interface between material and vacuum, both energy and transverse momentum must be conserved, such that
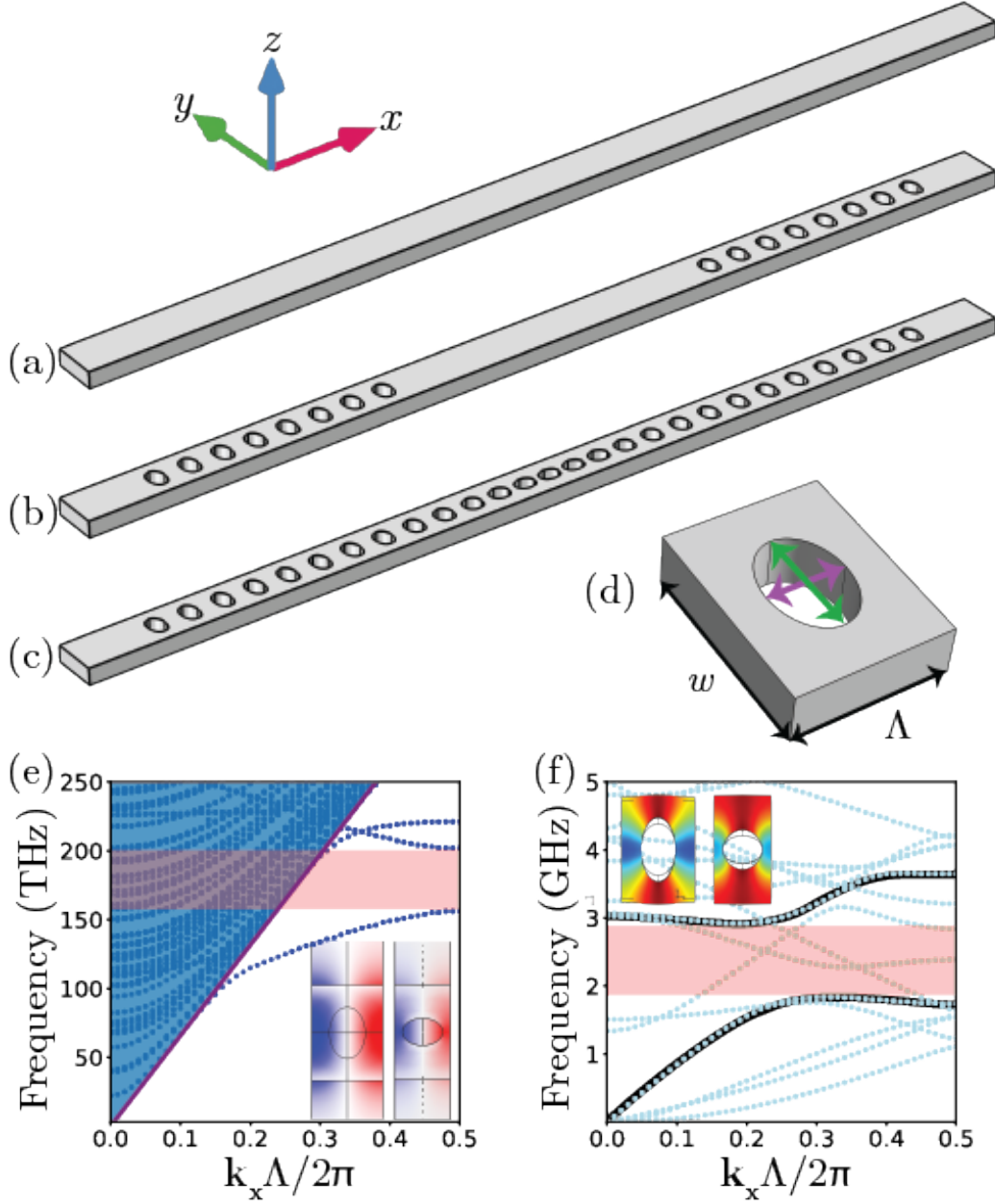
Figure 2.2: Illustration of optomechanical crystal design, beginning with (a) an optical waveguide. (b) Added photonic (and phononic) mirrors in a waveguide. (c) A mirror with a defect in the center. (d) Unit cell of the mirror, parametrized by the width of the nanobeam w, the unit cell length Λ, and the hole radii h_x and h_y indicated with purple and green arrows respectively. (e) The optical band diagram of the unit cell. Modes that exist in the blue-shaded region are above the lightline (purple) are are unguided. The bandgap, highlighted in red, is bounded from below by the inset mode simulation of the electric field x component. (f) Mechanical band diagram, with black lines highlighting in-plane modes capable of coupling to the mechanical breathing mode. A partial bandgap created between in-plane modes is highlighted in red, and bounded from below by the inset mode simulation of the mechanical mode displacement.

equalities between the frequencies $\omega_1 = \omega_2$ and parallel wave vectors $k_{1,\parallel} = k_{2,\parallel}$ must hold. Since the parallel component of the wave vector is $k_\parallel = \mathbf{k}\sin(\theta)$ and the wave vector itself is related to the frequency by $\omega = v|\mathbf{k}|$ for $v = c/n$ the speed of light in the material, these equalities manifest as Snell's Law

$$n_1\sin(\theta_1) = n_2\sin(\theta_2). \tag{2.44}$$

Below some critical angle $\theta_c = \arcsin(n_2/n_1)$, total internal reflection will confine the electric field within the beam, allowing it to propagate only along the length of the beam and effectively creating an optical waveguide. Total internal reflection can be better understood by considering the perpendicular component of the wave vector outside the beam [61],

$$k_{2,\perp}^2 = |\mathbf{k}_2|^2 - k_{1,\parallel}^2, \tag{2.45}$$

where we have used the conservation of parallel momentum. In the context of a plane wave $e^{i\mathbf{k}\cdot\mathbf{r}} = e^{ik_{2,\perp}r_\perp + ik_{2,\parallel}r_\parallel}$, if Eqn. (2.45) is less than zero this implies the exponential decay of the plane wave perpendicular to the waveguide—an evanescent field. Conversely, if Eqn. (2.45) is greater than zero then the perpendicular component is oscillatory and propagation outside the waveguide is permitted. This leads to a continuum of unguided modes. The boundary between guided and unguided modes,

$$k_{1,\parallel}^2 = |\mathbf{k}_2|^2 \tag{2.46}$$

$$= \frac{\omega^2 n_2^2}{c^2}, \tag{2.47}$$

is known as the light line in the band diagram [62].

2.5.2 Photonic Crystal

Creating an optical cavity from a waveguide requires light to be confined along the axis of the beam. Figure 2.2(b) introduces the photonic crystal, a 1D equivalent of a Bragg mirror where a set of holes in the material creates a periodic modulation in the index of refraction. Although the mirrors are finite in nature, they can be treated using periodic boundary conditions to understand their optical (and

mechanical) properties. To this degree we consider the unit cell shown in Fig. 2.2(d) and a Bloch wave (such as an electric field) propagating along the beam axis

$$\Psi(r_x) = e^{ik_x r_x}\psi(r_x), \tag{2.48}$$

where $e^{ik_x r_x}$ describes translation between unit cells and $\psi(r_x)$ describes a local potential within the unit cell. Each unit cell has a length Λ, and we consider a crystal of length $N\Lambda$, where N is the number of unit cells. To satisfy periodicity, Bloch's theorem states that [57]

$$\Psi(r_x + N\Lambda) = \Psi(r_x), \tag{2.49}$$

which allows us to identify the translating wave vector $k_x = 2\pi s/N\Lambda$ with integer $s \in [0, N-1]$. Equivalently, we consider the parameter $k_x\Lambda/2\pi \in [0, 1]$, and further reduce the space to $[0, 0.5]$ by exploiting phase symmetry about π. Scaling the wave vector adjusts the length of periodicity of the Bloch wave in the crystal structure. For example, the Bloch wave in each unit cell is identical for $k_x\Lambda/2\pi = 0$, whereas every other cell is identical when $k_x\Lambda/2\pi = 0.5$.

Photonic mirrors are effective reflectors for frequencies within a band gap, which is a region devoid of modes that support a Bloch wave. Hence, to understand where the the photonic mirror reflects, we must first investigate the allowed modes for all possible wave vectors k_x. This information is presented in the photonic band diagram Fig. 2.2(e), where each data point represents a simulated optical mode that the photonic crystal mirror supports. Above the light line, calculated using Eqn. (2.47) and shown in purple, there exists a continuum of unguided modes in the blue-shaded region, where $k_{2,\perp}$ is real-valued. These modes are not contained within the waveguide, and couple easily into free space. Below the light line, only three optical modes, which are modes guided by the material, exist in the photonic crystal for frequencies below 250 THz, two of which form the bounds of a band gap illustrated by the red shaded region.

By choosing a cavity length between the photonic mirrors that satisfies Eqn. (2.14) such that ω_c is within the band gap, Figure 2.2(b) represents the prototypical optical cavity manifested in a waveguide— essentially a 1D equivalent of the Fabry Pérot cavity from Fig. 2.1. However, the technique of modifying

20

the index of refraction by creating holes in the waveguide presents a more elegant solution to containing an optical mode: Fig. 2.2(c) illustrates a single mirror which gradually transitions to have holes of a different size and periodicity in the center, in effect creating a defect in the middle of the mirror. The gradual transition of the photonic mirror to a defect causes the lower-bounding optical band to be bent to a desired optical frequency in the mirror band gap. The inset in the band diagram shows simulations of the same electric field mode in the photonic crystal mirror cell at 150 THz and the optical defect at 190 THz. In this case, the defect caused the band to bend at the $\frac{k_x \Lambda}{2\pi} = 0.5$ point.

2.5.3 Phononic Crystal

In addition to hosting an optical mode, the photonic mirror simultaneously acts as a phononic mirror by preventing the propagation of acoustic phonons. It does this due to the unit cells acting as a mass-spring system, which has a specific set of resonance frequencies. In Fig. 2.2(f), the acoustic band diagram is presented for the mirror unit cell, with inset simulations of the 3 GHz acoustic mode in the mirror at the $\frac{k_x \Lambda}{2\pi} = 0$ point. As a result of the changing hole size and shape, the mechanical mode transitions to a frequency of 2.5 GHz in the acoustic defect. The band gap region for the acoustic defect is bound by two modes that restrict motion to the $x - y$ plane. Unlike the photonic crystal, the phononic crystal does not exhibit a complete bandgap. Instead, several modes are observed crossing through the region which is supposed to reflect acoustic phonons. These modes however involve motion in the z direction, and as a result they do not couple well to the in-plane defect mode. For this reason the mechanical mode is considered to be in a *quasi*-bandgap, which only weakly couples to other modes that exist in the region.

The combination of both photonic and phononic crystals in the same periodic structure is the essence of an optomechanical crystal, the device used for experiments in this thesis.

2.5.4 Mode Simulations

With unit cells, optomechanical crystal mirrors, and the optomechanical crystal defect now understood, the full optical and mechanical modes within the mirror

defect can be simulated. In Fig. 2.3(a), the x component of the electric field is shown to demonstrate the electric field alternation between unit cells, which occurs as a result of the mode being excited at the $k_x \Lambda / 2\pi = 0.5$ point. In Fig. 2.3(b) we plot the optical mode again, this time presenting the normalized electric field intensity. From Eqn. (2.34) we know that the optomechanical coupling depends on the optical intensity rather than the electric field itself, and hence this gives better perspective of the optical and mechanical mode overlap.

Figure 2.3(c) demonstrates the mechanical mode. Unlike the electric field profile, each unit cell of the mechanical mode presents the same motion profile, which is a result of the mode being tailored from the $k_x \Lambda / 2\pi = 0$ point in the band diagram. The mechanical motion is confined to the $x - y$ plane, and is often described as a 'breathing mode'.
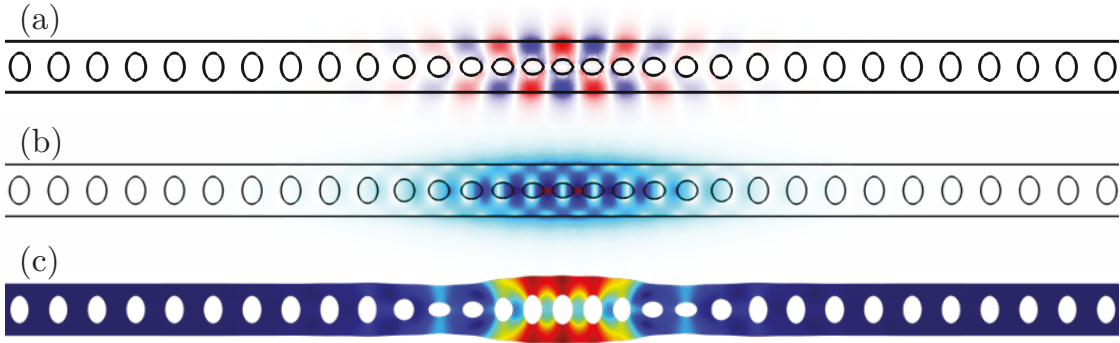
Figure 2.3: Simulations of an optomechanical crystal showing (a) the E_x electric field component, (b) the normalized electric field, and (c) the mechanical breathing mode.

These simulations can be used to estimate a number of important optomechanical parameters. The effective mass of the mechanical mode is generalized from the point mass considered in Section 2.2 to an effective motional mass which depends on the mechanical deformation of the resonator. The motional effective mass can be obtained by performing a volume integral over the density $\rho(\mathbf{r})$ and displacement $\mathbf{d}(\mathbf{r})$ of the optomechanical crystal, normalized by the point of maximum displacement [63]:

$$m_{\text{eff}} = \frac{\int \rho(\mathbf{r})\mathbf{d}(\mathbf{r})dV}{\max\left[\mathbf{d}(\mathbf{r})\right]}. \tag{2.50}$$

Similarly, an optical mode volume can be calculated from the electric field simulation,

$$V_{\text{opt}} = \frac{\int \epsilon(\mathbf{r})|\mathbf{E}(\mathbf{r})|^2 dV}{\max\left[\epsilon(\mathbf{r})|\mathbf{E}(\mathbf{r})|^2\right]}, \qquad (2.51)$$

where $\epsilon(\mathbf{r})$ is the dielectric constant of the material at position $\mathbf{r}$.

The optomechanical coupling can now be estimated using an integral that calculates the overlap of the mechanical displacement that is perpendicular to the surface $\mathbf{d}(\mathbf{r}) \cdot \mathbf{n}(\mathbf{r})$ and the electic field. In this case, the coupling calculated would be the moving boundary optomechanical coupling

$$g_{\text{mb}} = \frac{\omega_c x_{\text{zpf}}}{2V_{\text{opt}}} \int \mathbf{u}(\mathbf{r}) \cdot \mathbf{n}(\mathbf{r}) \left[(\epsilon_2 - \epsilon_1)|\mathbf{E}_\parallel(\mathbf{r})|^2 - \frac{\epsilon^2(\mathbf{r})\mathbf{E}_\perp(\mathbf{r})|^2}{\epsilon_2 - \epsilon_1}\right] dA, \qquad (2.52)$$

which becomes large when the overlap integral is large, the optical mode volume is small, and the zero-point fluctuations are large (requiring small effective mass). Similar methods exist for calculating the photoelastic optomechanical coupling [39, 40], which will be used for the design of future optomechanical devices.

2.5.5 Material Choice

Optomechanical crystals have been fabricated from a wide variety of materials including, but not limited to, silicon [56], silicon nitride [64], diamond [65, 66], aluminum nitride [26, 28, 67], gallium phosphide [68, 69], lithium niobate [30, 31], and gallium arsenide [29, 40].

Material choice is predicated on the balance of a number of factors, and depends on the intended application. For piezomechanical based microwave-to-telecom transduction, piezoelectricity is the crucial aspect, which ostensibly rules out non-piezoelectric materials such as silicon and diamond with the caveat of hybrid material devices [70]. Optomechanical coupling is also critical in achieving high efficiency transduction, which makes materials exhibiting strong photoelasticity excellent candidates. High optical indexes and electronic bandgaps are also important for confining the optical field within the material to minimize V_{opt} and reducing optical absorption effects that result in optical heating.

In Table 2.5.5 we present a brief overview of important material properties of piezoelectric materials for comparison, with the caveat that many of these

properties are incommensurable as they depend on the exact orientation of the optomechanical crystal within the material. For example, AlN is an ideal candidate for maximizing optomechanial coupling due the high photoelastic coefficient, but reported measurements of optomechanical coupling reveal values [28] an order of magnitude smaller than those of GaAs [40]. As a result, a proper comparison of materials for piezoelectric optomechanical crystals requires significant simulation and optimization, and may strongly depend on the precise optomechanical crystal geometry. There is no clear 'winner' among materials for optomechanical crystals.

Material	AlN	GaP	LN	GaAs
Optical index [71]	2.03	3.05	2.21	3.37
Electronic bandgap (eV)	4.1 [72]	2.3 [69]	3.0 [72]	1.4[73]
Photoelastic coeff. (max)	0.23 [74]	.11 [69]	0.3[30]	0.16[39]
Piezoelectric coeff. (pC/N)	4.0 [74]	-2.4 [72]	21 [72, 75]	2.6 [72]

Table 2.1: Properties of common piezoelectric optomechanical crystal materials

The choice of material for optomechanical crystals used in this thesis was dictated by availability. To date, the Davis lab has no experience with fabricating piezoelectric materials, and only recently have we begun the design and fabrication process for optomechanical crystals. To minimize the learning curve required to enter the field of microwave to telecom transduction using piezo-optomechanical crystals, we opted to collaborate with the Kartik Srinivasan's group at the National Institute of Standards and Technology in Gaithersburg, Maryland. Krishna Balram, a post-doc in the Srinivasan group, sent us ready-to-measure gallium arsenide optomechanical crystals, which allowed us to quickly begin conducting state-of-the-art experiments on transduction ready devices.

2.6 Device

The optomechanical crystal used throughout this thesis is a 13 μm long, 600 nm wide optomechanical crystal fabricated from 220 nm thick gallium arsenide. The optomechanical crystal design, shown in Fig. 2.4(a), is surrounded by a phononic shield meant to reduce the mechanical damping. The optomechanical crystal is one of 25 devices, which are laid out in a 5x5 grid, Fig. 2.4(b). Each row of the

grid represents a set of identical (up to fabrication imperfections) optomechanical crystals, where each column represents an increasing beam width between 580 nm and 620 nm in steps of 10 nm. A scanning electron microscope image, Fig. 2.4(c), shows the fabrication details of a gallium arsenide optomechanical crystal.
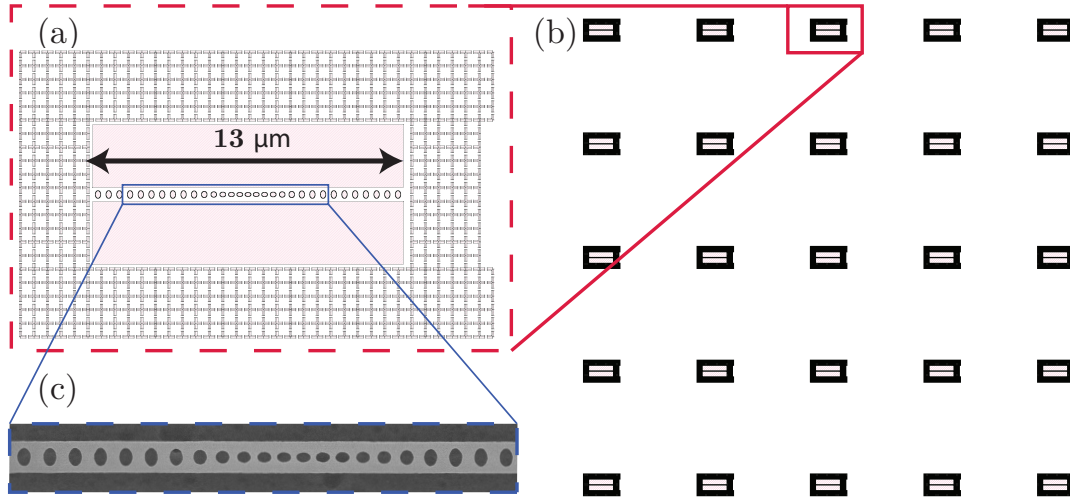
Figure 2.4: (a) Design of the optomechanical crystal. (b) Complete chip layout. (c) Scanning electron microscope image of a 600 nm wide optomechanical crystal.

In the following Chapter, the optical and mechanical modes of the device shown in Fig. 2.4(a,c) will be thoroughly calibrated. In addition to the data presented in this thesis, it is worth mentioning that several other devices were calibrated to varying degrees. In doing so, we found that the optical and mechanical properties changed slightly with beam width. Despite this, no direct comparisons are made between beams of varying width due to the variations in optical coupling causing similar shifts in the optomechanical crystal properties.

Chapter 3

Calibration & Experimental Design

The experimental apparatuses used to measure optomechanical crystals are an extension of the framework that had been built by previous graduate students in the Davis Lab. The concepts and infrastructure created by Doolin, Hauer, Kim, and MacDonald [45, 76, 77] for measuring the optical modes of microdisk resonators remains largely unchanged. Sections 3.1 and 3.2 briefly describe the apparatus used to make optical measurements and detail the characterization of the optical mode of the optomechanical crystal.

In contrast to the optical mode, measurements of the gigahertz mechanical breathing modes of optomechanical crystals require a significantly different approach than the megahertz modes of the cantilevers that are typically coupled to the optical microdisks. This paradigm change occurs primarily due to the limited speed of analog-to-digital converters, which are limited to collecting time-domain data for signals below 1 GHz. To capture the signal of high-frequency mechanical modes on an analog-to-digital converter, the signal must first be downmixed to a measurable frequency. There are several ways to approach this problem, which are detailed in this chapter and used for experiments throughout this thesis.

In addition to the intrinsic challenge of capturing high-frequency mechanical signals, there is a second, more insidious challenge—noise. During the course of the experiments that will follow, a common refrain was "At gigahertz frequencies everything is an antenna!" A quick calculation shows why this is true: for our mechanical mode, which we will measure to be near 2.4 GHz, the equation for the

length of a quarter wavelength antenna is

$$\lambda_{\frac{1}{4}} = \frac{2\pi c}{4\omega} = 3.12 \text{ cm,}$$

which means that the majority of the electronics used in measuring the optomechanical crystals can easily pick up stray electromagnetic radiation noise if not properly shielded. The noise then appears in the measurements and can obfuscate the mechanical mode. This becomes a particular issue just above 2.4 GHz, which is a common wi-fi broadcasting band.

3.1 Dimple Tapered Fiber Coupling

In the previous chapter, we showed that the optical mode of an optomechanical crystal exists within a bandgap below the light line. Above the light line, however, a plethora of unguided modes exist which can in theory couple to the optical mode. Despite this, mode-matching restrictions make it difficult to directly couple between unguided and guided modes (which is to the benefit of the optical decay rate κ). Instead, to optically couple to the optomechanical crystal we use a dimpled tapered fiber, presented in a microscope image in Fig. 3.1(a). To create the dimpled tapered fiber, we follow the process detailed in Ref. [45], which begins with a single-mode optical fiber that has been stripped of its cladding layer to expose the bare silica core. A small length of the core is then exposed to an open flame, and tension is applied across the length of the fiber such that the heated section of the core stretches out. As the core stretches, the core diameter subsequently shrinks to create a tapered region. The tapered region is then fitted around the core of another optical fiber and moulded to create the characteristic dimple shape shown in Fig. 3.2(a). The apex of the dimple has a radius of $25 \sim 50$ μm. Despite the tight radius of the fiber dimple, the fiber efficiency remains as high as 98% of the initial optical transmission.

When using the dimpled tapered fiber to couple to a device, the fiber is positioned such that the evanescent field at the dimple overlaps the evanescent field of the optomechanical crystal. The narrow radius of the dimple allows the contact point between the optomechanical crystal and the fiber to be selected with ~ 5 nm
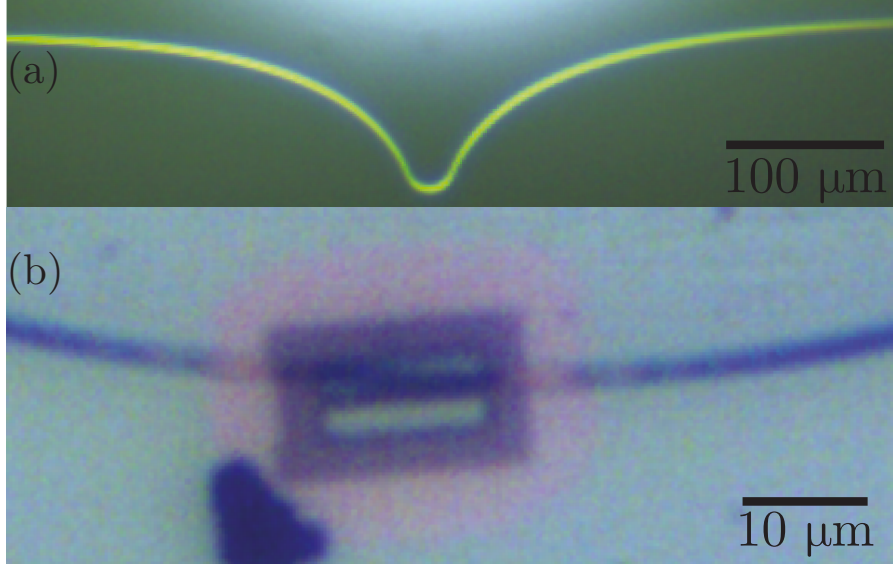
Figure 3.1: (a) Microscope image of the dimpled tapered fiber from the side and (b) coupling to an optomechanical crystal.

accuracy along the fiber axis. In the next section, we will show that this accuracy is crucial to controlling optical coupling between the dimpled tapered fiber and the optomechanical crystal. Figure 3.1(b) presents a microscope image of the dimpled tapered fiber coupling to an optomechanical crystal. In this picture, the fiber and the optomechanical crystal are purposely aligned off-axis to allow for increased precision when coupling.

3.2 Optical Properties

In Fig. 3.2, a simple schematic of the setup used to measure the optical transmission profile of an optomechanical crystal is shown. The transmission profile is measured using a tunable laser[1], which sweeps the laser frequency (equivalently, wavelength) across the optical resonance. The optical field emitted from the laser $\hat{a}_{\text{in}}$, with intensity

$$|\hat{a}_{\text{in}}|^2 = \frac{P_\ell}{\hbar\omega_\ell} \tag{3.1}$$

set by the laser power P_ℓ, is carried through the dimpled tapered fiber to the optomechanical crystal defect, where it couples into the optical mode at a rate κ_{e}.

---

[1]Santec TSL-510

Due to the fact that the optical mode reacts quickly to a changing input, for the purposes of measuring the transition profile, we consider the optical mode to have a steady-state optical field $\hat{a}$. From the optical mode, light is lost to the environment at a rate κ_0, and couples back into the fiber at a rate κ_{e} for a total optical decay rate $\kappa = \kappa_{\mathrm{e}} + \kappa_0$. The optical field that re-enters the fiber is split into two equal parts, a reflected field which is typically discarded, and a transmitted field $\hat{a}_{\mathrm{out}}$, which is detected at a photodiode. The emitted optical field, in the absence of mechanics, is [78]

$$\hat{a}_{\mathrm{out}} = \hat{a}_{\mathrm{in}} + \frac{\sqrt{\kappa_{\mathrm{e}}}}{2}\hat{a}, \tag{3.2}$$

where we recall the steady state optical cavity field $\hat{a}$ from Chapter 2,

$$\hat{a} = -\frac{\sqrt{\kappa_{\mathrm{e}}}\hat{a}_{\mathrm{in}}}{i\Delta + \kappa/2}. \tag{3.3}$$

Using this, we find the detected intensity on the photodiode,

$$|\hat{a}_{\mathrm{out}}|^2 = |\hat{a}_{\mathrm{in}}|^2 - \frac{\kappa_0 + \kappa_{\mathrm{e}}/2}{2}|\hat{a}|^2. \tag{3.4}$$

By dividing both sides of Eqn. (3.4) by $|\hat{a}_{\mathrm{in}}|^2$, we obtain an equation for the normalized transmission through the optical cavity for any given detuning. This can ostensibly be used to fit optical resonances, such as those presented in Fig. 3.3(a), though often an additional term is included in the fit to account for thermorefractive non-linearities resulting from a high cavity photon occupancy [79]. The resonances presented in this thesis are deemed 'near-linear', with small thermorefractive contributions. As such, we will consider Eqn. (3.4) to be the default equation used to fit optical resonances with the understanding that there may be small non-linearities in play.

The optical intensity measured on the photodiode[2] is converted into a voltage signal, which is then measured on a data acquisition card[3] as a DC signal. Figure 3.3(a) presents two optical transmission profiles of an optomechanical crystal to illustrate the effect of the fiber on the optical mode. The top profile

---

[2]Typically a 1 GHz Newport 1611 photo receiver. Despite the 3 dB rolloff at 1 GHz, it is capable of detecting 2.4 GHz signals. If high frequency measurement is not required then a 40 MHz Resolved Instruments DPD80 may be used.

[3]National Instruments USB-6259 multifunction IO, set to sample at 50 kHz
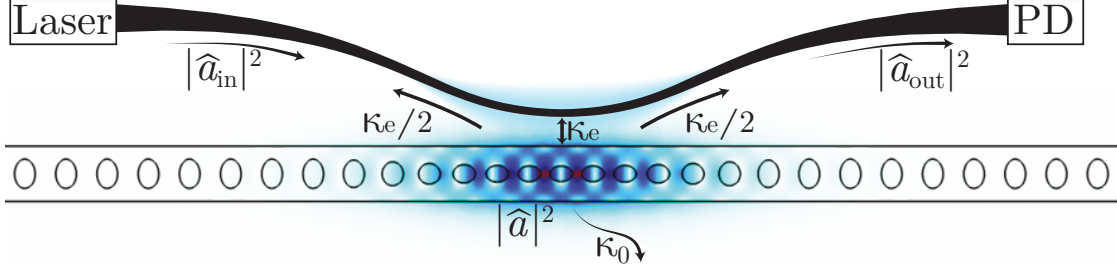
Figure 3.2: Diagram of dimpled tapered fiber coupling to the optical mode of the optomechanical crystal. The dimple is shown with its own evanescent field overlapping the optical mode. The transmitted optical intensity is measured on a photodiode (PD).

shows a mostly undisturbed transmission profile, whereas in the bottom profile the optical fiber is in direct contact with the optomechanical crystal defect, such that the index of the dimpled tapered fiber causes the optical mode to be distorted. The effect of the fiber is assessed by taking repeated transmission profiles while moving the fiber closer[4] to the optomechanical crystal defect and recording the internal κ_0 and external κ_e decay rates, Fig. 3.3(b), and the change in resonance wavelength, Fig. 3.3(c). At a certain point, where the total decay rate is near $\kappa/2\pi \approx 6$ GHz, the internal decay rate begins to increase which indicates that the proximity of the optical fiber causes photons to scatter from the optical mode. To limit this scattering effect, the fiber is first deliberately misaligned from the long axis of the optomechanical crystal to limit the overlap of the fiber with the optical mode. Then the fiber is typically positioned such that the total decay rate is between $5 \sim 7$ GHz, which balances the distortion of the optical mode with the need for enough optical coupling to measure a mechanical signal.

In addition to the scattering caused by the dimpled tapered fiber, the optical cavity has a baseline internal decay rate $\kappa_0 \approx 4$ GHz, which is caused by a mixture of optical absorption and scattering. It is hypothesized that a large source of the scattering is from the underside surface of the optomechanical crystal, which is

---

[4]This experiment is made possible using Attocube 3-axis piezo-stages with the ANC-300 controller, which allows for small, equal amplitude steps to be made with minimal vibrations. The fiber and device must moreover be vibration damped by air. Other stages used for manoeuvring the fiber and/or devices such as the Agilus piezo-stages or Newport micrometer stages can cause vibrations which cause the fiber to latch onto the device unexpectedly. Accurate coupling with these stages is still possible, but coupling distance sweeps are not.
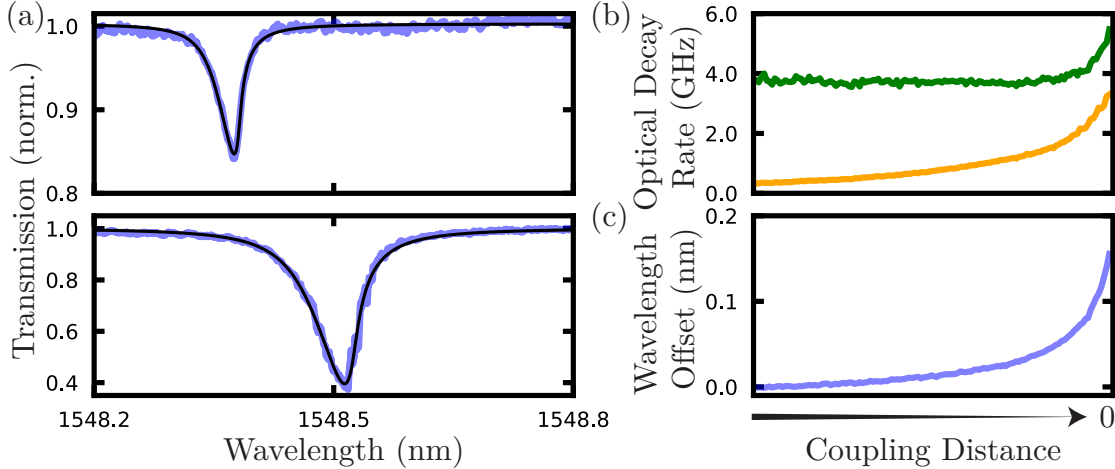
Figure 3.3: (a) Transmission profile (blue) with fits (Eqn. (3.4), black) of the optical resonance when the fiber is (top) far away from the optomechanical crystal defect and (bottom) in contact with the crystal defect. The transmission profiles have been normalized by dividing by the laser input power. (b) Internal (dark green) and external (light orange) optical decay rates, and (c) change in wavelength as a function of distance from fiber to optomechanical crystal defect.

rough due to fabrication imperfections [40]. This surface rougness plays a limiting role in reducing the total cavity decay rate, and therefore sets the maximum optical cavity quality factor to $Q \approx 50,000$.

3.3 Mechanical Measurement Techniques

In Eqn. (2.28), we determined that mechanical motion causes shifts in the optical resonance frequency, scaled by the optomechanical coupling. This implies that the mechanical motion can be measured by monitoring the optical resonance transmission (direct detection) or phase (homodyne or heterodyne detection). In both cases, the mechanical signal is imparted onto the measured optical intensity as a modulation. A photodetector[5] is then used to convert the optical intensity into a AC voltage signal, which can in turn be digitized for analysis using a high speed (1 GHz) analog-to-digital converter[6] or a real-time spectrum analyser.[7]

During the course of the experiments in this thesis, the methods used to measure

---

[5]Direct detection: Newport 1611 photoreciever, homodyne: 800 MHz Newport 1811 balanced photoreciever, heterodyne: 40 MHz Resolved Instruments DPD80 Balanced

[6]Ultraview AD12-2000

[7]Tektronix RSA 306b

mechanical signal were constantly developed and adapted as experiments progressed. Initial experiments used direct detection, which is the most common method for detecting low-frequency mechanical motion in the Davis Lab, coupled with a real-time spectrum analyser to allow for the measurement of high frequency signals. Although this spectrum analyser is useful for finding mechanics, the software that accompanied the instrument made it of limited use for integration in the data collection and analysis process flow. As such, our discussion on measuring mechanical motion will include only a brief description of direct detection, which will then be followed by an in-depth description of the phase measurement techniques that were used to collect the majority of the experimental data.

3.3.1 Mechanical Modulation of the Optical Mode

Instead of sweeping the laser frequency, as we previously did to measure the optical mode in Fig. 3.3, we consider a measuring laser set to a constant frequency to measure mechanical motion. As before, the optical field inside the cavity is populated by the laser to create the static optical cavity field Eqn. (3.3), but we now further consider the dynamic response imposed by the mechanical motion. A complete derivation of the dynamic response due to mechanical motion can be found in Appendix A, where it is shown that for a mechanical signal $x(t) = x_0 \cos(\omega_\mathrm{m} t)$, the optical cavity field is phase modulated sinusoidally by the mechanics and can be approximated as the static optical cavity field with two sidebands,

$$\hat{a}(t) = \hat{a} e^{-i\beta_\mathrm{m} \sin(\omega_\mathrm{m} t)}, \tag{3.5}$$

$$\approx \hat{a} \left[1 - \frac{\beta_\mathrm{m}}{2} \left(e^{i\omega_\mathrm{m} t} - e^{-i\omega_\mathrm{m} t} \right) \right], \tag{3.6}$$

where the mechanical modulation sidebands are detuned from the carrier frequency by $\pm\omega_\mathrm{m}$ and have amplitude determined by the mechanical modulation index

$$\beta_\mathrm{m} = \frac{g_0 x_0}{\omega_\mathrm{m} x_\mathrm{zpf}}. \tag{3.7}$$

The complete equation for the optical field after the cavity can then be found by replacing the static response $\hat{a}$ in Eqn. (3.4) with the dynamic response $\hat{a}(t)$ from Eqn. (3.6),

$$\hat{a}_\mathrm{out}(t) = \hat{a}_\mathrm{in} + \frac{\sqrt{\kappa_\mathrm{e}}}{2} \hat{a} \left[1 - \frac{\beta_\mathrm{m}}{2} \left(e^{i\omega_\mathrm{m} t} - e^{-i\omega_\mathrm{m} t} \right) \right]. \tag{3.8}$$

3.3.2 Direct Detection

Direct detection involves setting the laser to the maximum slope of the optical resonance (direct detection is also known as "tuned-to-slope" detection), found by maximizing the derivative of Eqn. (3.4) with respect to detuning such that

$$\frac{d|\hat{a}_{\text{out}}(t)|^2}{d\Delta^2} = 0. \tag{3.9}$$

At this detuning, shifts in the optical frequency result in maximal changes in transmission. By considering the optical field intensity incident on the photodetector at this detuning, $|\hat{a}_{\text{out}}(t)|^2$, we can predict the AC voltage signal response produced by the photodetector [80],

$$V_{\text{dir}}(t) = \eta_d(\omega)|\hat{a}_{\text{in}}|^2 \beta_{\text{m}} \kappa_{\text{e}} \mathcal{K}_{\text{dir}}(\Delta, \omega_{\text{m}}) \sin(\omega_{\text{m}}t), \tag{3.10}$$

where the detector efficiency $\eta_d(\omega)$ contains both the photodetector gain and responsivity,[8] which is frequency dependent. The function $\mathcal{K}_{\text{dir}}(\Delta, \omega_{\text{m}})$ is a detuning and frequency dependent measurement function, which is zero at $\Delta = 0$ and maximized near the maximum slope (see Fig. 3.4) of the static optical resonance at

$$\Delta = \pm \frac{\sqrt{(2\omega_{\text{m}})^2 + \kappa^2}}{2\sqrt{3}}. \tag{3.11}$$

The exact forms of the direct detection measurement function used in Eqn. (3.10) and a similar phase detection measurement function are explored thoroughly in Refs. [77, 80, 81]. For the experiments in this thesis they are treated as blackbox gain factors that arise from the optical resonance.

3.3.3 Phase Detection

In addition to the intensity response used for direct detection, the optical cavity also exhibits a phase response, pictured in Fig. 3.4, that can be used to detect mechanical motion. The static phase response of the optical mode is derived from the optical susceptibility by taking the argument of Eqn. (3.3) to find

$$\phi_{\text{cav}} = \arctan\left(-\frac{\Delta}{\kappa}\right), \tag{3.12}$$

---

[8]For the high-frequency mechanical breathing modes measured in this thesis, the detectors mechanical frequency was beyond the specifications provided by the manufacturer. As a result, the detector frequency response is unknown.
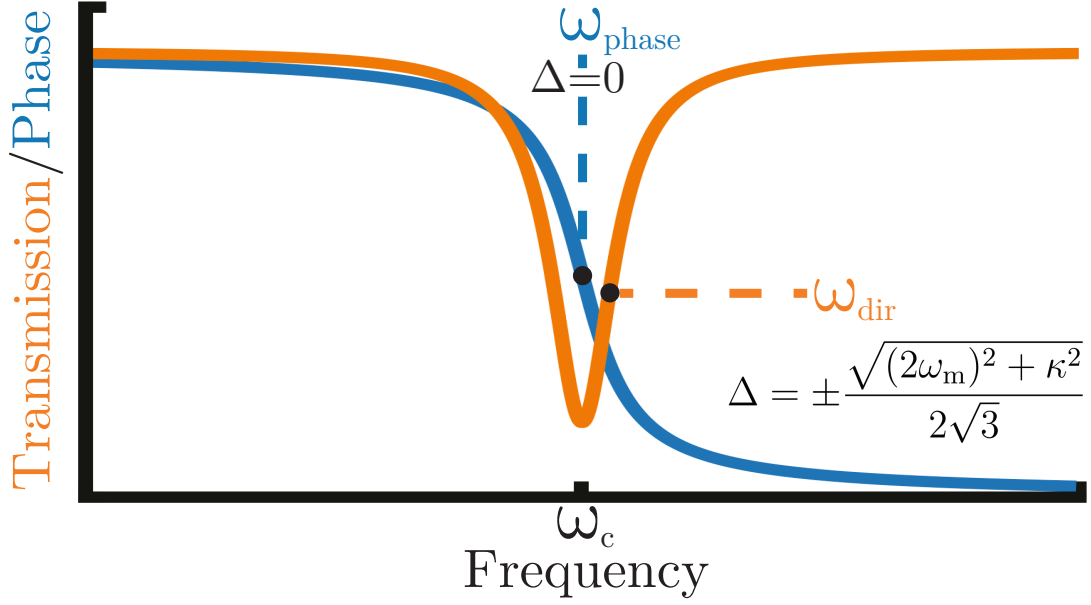
Figure 3.4: Schematic of optical cavity transmission amplitude (orange) and phase (blue) responses. Laser tunings for both direct (blue detuned $\Delta < 0$) and phase detection are labelled, showing that for both detection schemes the laser is tuned to the maximum transmission or phase slope respectively.

which is approximately linear in the region $\Delta \approx 0$. The phase of the cavity shifts with mechanical motion as the resonance frequency changes, which implies that by setting a measuring laser to the optical resonance frequency $\omega_\ell = \omega_c$, the mechanical motion can be measured using an optical phase detection scheme.

The phase of an optical cavity cannot be directly detected, as photodetectors measure optical intensities, which carry no phase information, instead of optical fields. Phase measurements must instead be performed using interferometry, where the laser light emitted from the optical cavity is mixed with a reference laser to create a phase-dependent interference pattern. Phase detection provides two significant advantages: first, the local oscillator adds optical gain to the system, allowing for very small optical fields in the signal arm to be measured; second, because measurements occur at zero detuning, there is no optical backaction on mechanical measurements. In the next sections, we will explore the methods we use to make phase measurements.

3.3.4 Optical Homodyne Detection

Homodyne detection is the basis upon which we build our phase measurement systems, and is a common method of measuring the mechanical motion of optomechanical devices [80, 82, 83]. Figure 3.5(a) shows a prototypical model of an optical homodyne system, in which a laser is split along two paths by a beamsplitter,[9] the signal arm and the local oscillator arm. The signal arm interacts with the optomechanical crystal which causes the transmitted optical field to pick up phase modulations imparted by the mechanics, while the local oscillator acts as the phase reference. The resulting spectra of the mechanically modulated light and the local oscillator are shown pictorially in Fig. 3.5(b).
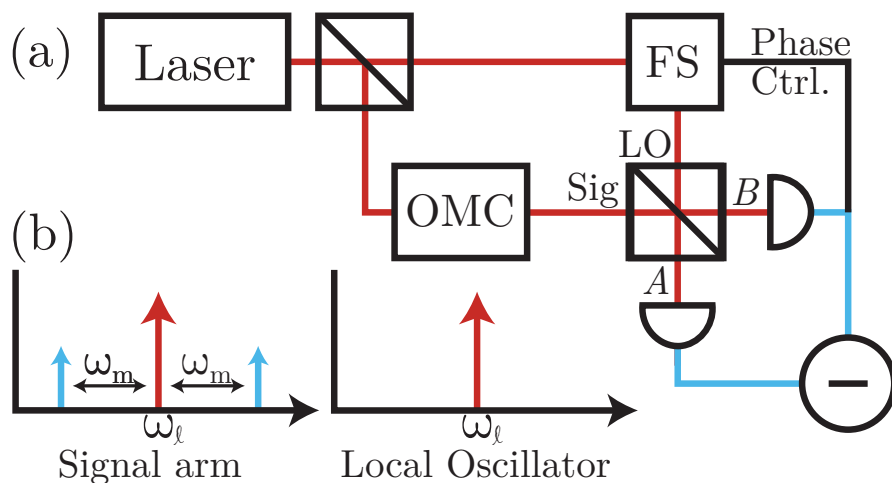
Figure 3.5: (a) Homodyne detection system for performing phase measurements on an optomechanical crystal (OMC). The laser path is split at a beamsplitter into a signal and local oscillator arm, which recombine at a second beamsplitter to be detected on a balanced photodetector. To ensure phase matching of the measurement arms, a fiber stretcher (FS) is used to balance path lengths. (b) Cartoon spectrum of the signal arm and local oscillator, showing the sidebands generated by mechanical motion.

The signal and local oscillator arms recombine at a 50:50 beamsplitter[10] to create two signals A and B, which are subsequently detected on a balanced photodetector.[11]

---

[9]Evanescent Optics Inc. variable coupler
[10]Thorlabs 2x2 50:50 wideband coupler
[11]Newfocus 1811 balanced photoreciever

The difference between the detected signal intensities is

$$|A|^2 - |B|^2 = 2i(\hat{a}_{\mathrm{LO}}(t)\hat{a}_{\mathrm{out}}^\dagger(t) - \hat{a}_{\mathrm{LO}}^\dagger(t)\hat{a}_{\mathrm{out}}(t)) \tag{3.13}$$

$$= 2|\hat{a}_{\mathrm{LO}}|(|\hat{a}_{\mathrm{in}}| + |\hat{a}|)\sin(\phi_{\mathrm{LO}}) + |\hat{a}_{\mathrm{LO}}||\hat{a}|\sqrt{\kappa_{\mathrm{e}}}\beta_{\mathrm{m}}\cos(\phi_{\mathrm{LO}})\sin(\omega_{\mathrm{m}}t), \tag{3.14}$$

where $\hat{a}_{\mathrm{LO}}(t) = \hat{a}_{\mathrm{LO}}[e^{-i\omega_\ell t - i\phi_{\mathrm{LO}}}]$ is the optical field of the local oscillator arm, which has a phase offset ϕ_{LO}. The phase offset between the measurement arms can be set using a fiber stretcher.[12] Notice, importantly, that the AC and DC components of the homodyne signal are quadrature separated by the local oscillator phase. By setting the path length such that the local oscillator phase offset is an integer multiple of 2π (ideally zero), the DC component can be eliminated ($\sin(\phi_{\mathrm{LO}}) = 0$) and the AC signal can be maximized ($\cos(\phi_{\mathrm{LO}}) = 1$). The homodyne output voltage then oscillates at the mechanical frequency,

$$V_{\mathrm{hom}}(t) = \eta(\omega)|\hat{a}_{\mathrm{LO}}||\hat{a}_{\mathrm{in}}|\kappa_{\mathrm{e}}\beta_{\mathrm{m}}\mathcal{K}_{\mathrm{hom}}(\Delta, \omega_{\mathrm{m}})\sin(\omega_{\mathrm{m}}t), \tag{3.15}$$

where $\mathcal{K}_{\mathrm{hom}}(\Delta, \omega_{\mathrm{m}})$ is our black-box detuning dependent measurement function for homodyne measurement [80], which is maximized for zero detuning.

In this scenario, the voltage output by the photodetector depends on the optical field amplitude of both the signal arm and the local oscillator. This allows for very small signal-arm optical fields to be measured using a strong local oscillator that acts as an amplifier, which permits low-power optical measurements of mechanical motion.

3.3.5   Balancing Homodyne Paths

The homodyne detection scheme poses significant advantages over direct detection, but also requires a more complicated experimental setup. The primary challenge of implementing an optical homodyne detection scheme arises from the short wavelength of telecom light. To set the local oscillator phase offset to an integer multiple m of 2π, the path length difference ΔL between the signal and

---

[12]Optiphase PZ1 high-speed fiber stretcher

local oscillator arms must be similarly constrained,

$$\phi_{\text{LO}} = \frac{2\pi \Delta L}{(\lambda_\ell/n)} = 2\pi m \tag{3.16}$$

$$\Rightarrow \Delta L = m\frac{\lambda_\ell}{n}, \tag{3.17}$$

where λ_ℓ is the vacuum wavelength of light and $n \approx 1.47$ is the fiber index of refraction. If m is large, then small fluctuations in the laser wavelength will result in large phase fluctuations between the measurement arms. Thus, to minimize noise it becomes critical to match the homodyne arm lengths as closely as possible.

Prior to beginning the balancing process, we must determine which arm of the homodyne system is initially longer. If the signal arm is longer, then extra fiber must be added to the local oscillator arm, if the local oscillator is longer, then the opposite is true. For room temperature experiments the local oscillator arm will sometimes be longer due to the 12.5 m of fiber contained within the fiber stretcher. For low temperature experiments, the amount of fiber contained within the dilution refrigerator means that the signal arm is typically longer. Determining which arm is longer is most easily done by adding known lengths of fiber to either arm, and proceeding with the first stage of balancing.

Matching homodyne arm length is achieved in two stages. In the first stage, a short duration optical pulse is injected into the homodyne system using an acousto-optic modulator[13] as a fast on-off switch. The beamsplitter splits the pulse into two separate pulses which travel through the system and arrive at the photodetector different times. The output of the AC output of the photodetector is then viewed on an oscilloscope[14], which is used to calculate the time difference between pulses. The path length difference can then be calculated as

$$\Delta L = \frac{c}{n}\Delta t, \tag{3.18}$$

such that c/n is the speed of light in the fiber, and Δt is the pulse arrival time difference. By adding various lengths of fiber to one of the arms, the relative arrival time of the pulses will change, which allows us to determine which arm is initially longer. A long spool of fiber is then added to shorter arm. By cutting down the

---

[13]Gooch & Housego 200 MHz
[14]LaCroy dda-125
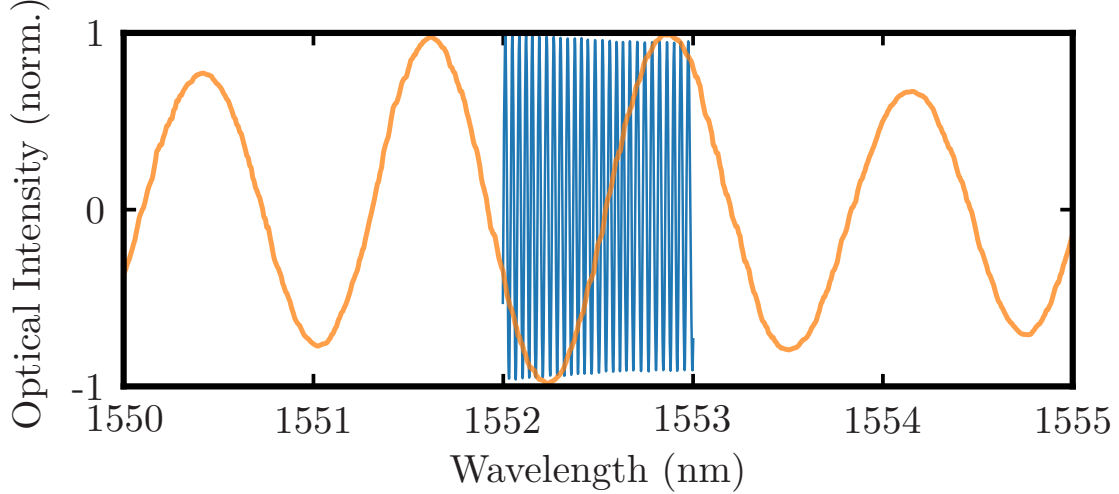
Figure 3.6: Stage two of balancing a homodyne detection system: a wavelength sweep demonstrating signal and local oscillator arms with mismatched path lengths. A 1 nm laser scan in blue shows phase oscillations from a 46 mm path length difference, which requires further balancing. In contrast, the 5 nm laser scan in orange shows phase oscillations from a ≈ 1 mm path length difference, indicating that the arms are adequately balanced.

length of the fiber spool, the path lengths of the arms can be equalized. Using the optical pulse technique, the length of the fiber spool is reduced until the path length difference is approximately one meter, at which the ≈ 5 ns time difference becomes difficult to measure on the oscilloscope.

To further reduce the path length difference below one meter, the homodyne system is measured while the laser wavelength is swept over a narrow region. Since the DC output of the homodyne detector depends on the homodyne phase difference and the phase difference in turn is wavelength dependent, the DC optical intensity oscillates sinusoidally as a function of laser wavelength, as shown in Fig. 3.6. By counting the number of periods over a wavelength range, the path length difference can be calculated as

$$\Delta L = \frac{2\pi c \Delta m}{n \Delta \lambda_\ell^{-1}}, \tag{3.19}$$

which is derived using Eqn. (3.17) at two wavelengths. Δm is the number of periods over the wavelength range, and represents the change in the integer multiple relating path length and laser wavelength.

Using the wavelength sweep method in tandem with a fiber cleaver[15] to remove 2 cm lengths from the fiber spool, path length differences on the order of 1 mm can be routinely achieved. Once the path lengths are equalized, a fusion splicer[16] is used to permanently connect the fiber spool to the system. Figure 3.6 demonstrates a path length difference of ≈ 1 mm, which results in approximately one phase oscillation per nanometer wavelength. Using Eqn. (3.17), this corresponds to the homodyne arms having lengths that differ by $m \approx 1000$ wavelengths. While this may seem like a large imbalance in the homodyne system, it results in experimentally acceptable sensitivity to laser wavelength changes. Using Eqn. (3.19), a shift of 5 pm in laser wavelength (which is the laser specification for accuracy) results in a shift of $\Delta m = 0.003$ periods ($\Delta\phi_{LO} = 0.018$ rad).

For this discussion we have assumed that the primary complication in homodyne detection is changes in laser wavelength, simply because changing the wavelength is the primary manner in which we characterize the path length difference. However, the truth is that homodyne balancing complications stem from time-varying path length differences in the arms, which are hypothesized to arise from stress and temperature dependence of the fiber index of refraction. Because of the equivalence between wavelength and path length difference stated in Eqn. (3.17), the discussion of laser noise applies directly to path-length-induced noise. As such, we can write an equation for the change in phase due to a change in the effective path length difference $\Delta(n\Delta L)$,

$$\Delta\phi_{LO} = \frac{2\pi\Delta(n\Delta L)}{\lambda_\ell}. \tag{3.20}$$

The path length changes induced by stress and temperature effects tend to be slow in nature, and as a result can be automatically corrected for using a control loop that tunes the local oscillator arm length using the fiber stretcher. In Fig. 3.5, the input to the control loop is one of the three power monitors on the balanced photodetector,[17] which have a phase-difference dependent DC signal that is sent

---

[15]Ericsson EFC11 fiber cleaver

[16]Ericsson FSU 995 FA

[17]The Newfocus 1811 balanced photoreciever has voltage pick-offs from either photoreceiver on the homodyne detector and the DC homodyne difference signal.

to a feedback controller,[18] amplified,[19] and used to drive the fiber stretcher. The fiber stretcher has a 12.5 m spool of fiber wound around a piezoelectric core, which expands proportionally to the applied voltage causing the fiber spool to stretch. This increase to the path length of the local oscillator results in a compensating phase shift. By choosing a voltage setpoint that sets $\phi_{\mathrm{LO}} = 0$ (and therefore maximizes the AC signal), the homodyne system can be continuously tuned such that detection of the mechanical signal is always maximized.

3.3.6 Optical Heterodyne Downmixing

Both direct and homodyne detection produce voltage signals that oscillate at the mechanical frequency, which, as previously noted, is too fast to be detected using analog-to-digital converters.[20] Optical heterodyne detection provides a phase-measurement based solution to this problem by optically downmixing the mechanical signal before it is detected on the photodetectors. Though optical heterodyne has been used in optomechanical measurement systems previously [84], the application of optically downmixing high-frequency mechanical signals for detection on low-frequency is new.

In homodyne detection, the phase is measured by comparing the optical sidebands produced by mechanical motion to the local oscillator at the laser frequency. The detector then measures the beat-note present in the intensity. Heterodyne takes advantage of the same principle, except that the local oscillator frequency is now detuned by an amount near, but not equal to, the mechanical frequency. This causes the resulting beat note to appear at the difference between the frequency shift and the mechanical frequency, effectively downmixing the mechanical signal.

One method of achieving a shifted local oscillator would be to use a separate laser. However, small fluctuations in the laser wavelength due to thermal or electronic noise could cause large changes in the frequency offset, which would be disastrous for mechanical measurements—a 5 pm wavelength fluctuation corresponds to a

---

[18]Newport LB1005 Servo Controller

[19]RHK Technology HVA 900 high voltage amplifier

[20]The 1 GHz Ultraview analog-to-digital converters used here are among the fastest cards that can be purchased.

600 MHz frequency shift at 1550 nm. Instead, we choose to split the laser frequency into two arms as we did for homodyne detection, but now shift the laser frequency using an optical modulator. Ideally, an acousto-optic modulator (AOM) would be used to produce a single tone at a shifted frequency, however AOMs are typically limited to ~ 400 MHz, which, without linking several AOMs in series, is insufficient for our purposes.
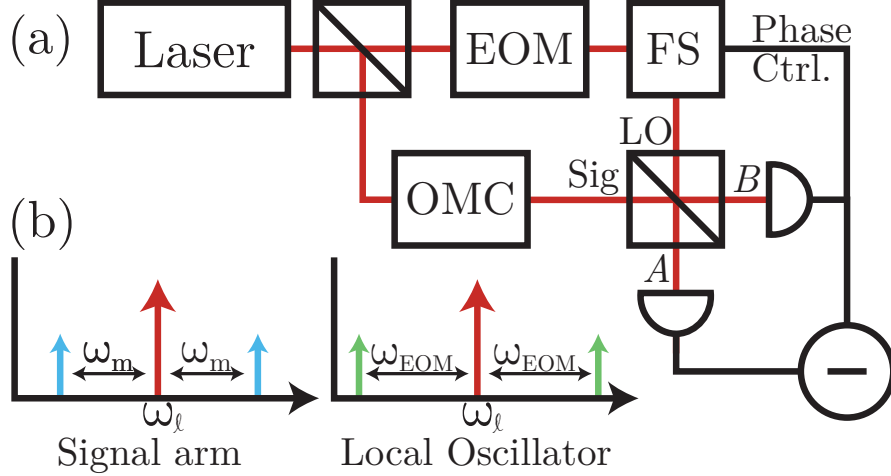
Figure 3.7: (a) Heterodyne detection system for performing optically downmixed measurements of the device mechanics. The setup is identical to homodyne, with the exception of an included electro-optic phase modulator (EOM). (b) Cartoon spectrum of the signal arm and the local oscillator, showing optical sidebands generated by both the mechanical motion and the EOM.

In Fig. 3.7(a), we illustrate a heterodyne detection system which uses an electro-optic phase modulator[21] (EOM). The principle of operation behind the EOM is identical to the mechanics in that it produces two optical sidebands created by phase modulation $\phi(t) = \sin(\omega_{\mathrm{EOM}}t)$ in addition to passing through some of principle laser tone (for details, see Appendix A). Thus, the light in the local oscillator can be described in the rotating frame of the laser as

$$\hat{a}_{\mathrm{LO}}(t) = \hat{a}_{\mathrm{LO}}e^{-i\beta_{\mathrm{EOM}}\phi(t)} \tag{3.21}$$

$$= \hat{a}_{\mathrm{LO}}\left[1 - \frac{\beta_{\mathrm{EOM}}}{2}(e^{i\omega_{\mathrm{EOM}}t} - e^{-i\omega_{\mathrm{EOM}}t})\right], \tag{3.22}$$

where ω_{EOM} is a gigahertz input tone produced by an external signal generator, which modulates the local oscillator field with strength determined by the

---
[21] EOSpace LiNbO$_3$ 10 GHz phase modulator

modulation index $\beta_{\mathrm{EOM}} = \pi V_{\mathrm{EOM}}/V_\pi$, where V_{EOM} is the voltage amplitude of the signal applied to the EOM, and V_π is the half-wave voltage that would result in a π phase shift.[22] Figure 3.7(b) depicts the spectral components of the heterodyne signal after the local oscillator and signal arms are mixed at the beam splitter. Due to the number of laser tones, the intensity detected has a number of spectral components: $\pm\omega_{\mathrm{m}}$, $\pm\omega_{\mathrm{EOM}}$, and $(\pm\omega_{\mathrm{EOM}} \pm \omega_{\mathrm{m}})$. By choosing to drive the EOM at a frequency $\omega_{\mathrm{EOM}} \approx \omega_{\mathrm{m}} \pm 10$ MHz, the photodetector will measure the downmixed signal at $\pm|\omega_{\mathrm{EOM}} - \omega_{\mathrm{m}}|$, while the high frequency combinations can be electronically filtered, or simply time-averaged by the analog-to-digital converter.

The complexity of the optical signal after being mixed at the beamsplitter makes it clear why an AOM was earlier suggested as the ideal optical mixer for optical heterodyne downmixing. Using a single tone in the local oscillator considerably reduces the complexity of the downmixed signal, reducing the number of tones from eight to just three. This scenario can be replicated by inserting a filter in the local oscillator arm to pick off a single EOM sideband. In this case, the produced tones are ω_{EOM}, $\omega_{\mathrm{EOM}} - \omega_{\mathrm{m}}$, and $\omega_{\mathrm{EOM}} + \omega_{\mathrm{m}}$. In practice, however, filtering the local oscillator becomes difficult as the frequency difference between the laser tone and EOM sideband places a stringent requirement on optical filter bandwidth, and drifts in the filter can cause the local oscillator intensity to fluctuate. In our system, we chose to avoid the complications associated with filtering the signal, but the next generation of optical heterodyne detection systems may choose to implement an optical filter to improve signal clarity.

3.3.7 Electrical Homodyne Downmixing

A second method of measuring high-frequency signals is by electronically downmixing the voltage signal produced by the photodiode to a frequency that can be measured on the analog to digital converter and then digitally upconverted to the true frequency [84]. This method is advantageous in that it can be applied to both direct and phase detection measurements. There are several ways of electrically downmixing the mechanical signal, including the straightforward approach of using

---

[22]The EOspace EOM used for heterodyne has $V_\pi = 4.5$ V, calculated using the procedure in Appendix A

a frequency mixer to produce an intermediate frequency. Here we approximate the output of the photodetector as a sinusoidal signal with specific amplitude A, frequency ω_{sig}, and phase ϕ: $A\cos(\omega_{\text{sig}}t + \phi_{\text{sig}})$, and use an electronic local oscillator (ELO) tone $\cos(\omega_{\text{ELO}}t)$. We note now that while mechanical motion is incoherent in nature and thus does not have a singular phase to be measured, the microwave-to-telecom transduced tones we will later investigate do carry a specific phase based on the phase of the microwave input. Thus for the purpose of being general, we consider a generic input signal with a well-defined phase. With this understanding, the output of the mixer is

$$A\cos(\omega_{\text{sig}}t + \phi_{\text{sig}})\cos(\omega_{\text{ELO}}t) = \frac{A}{2}\Big[\cos((\omega_{\text{sig}} + \omega_{\text{ELO}})t + \phi_{\text{sig}})$$
$$+ \cos((\omega_{\text{sig}} - \omega_{\text{ELO}})t + \phi_{\text{sig}})\Big]. \tag{3.23}$$

Thus by choosing an intermittent frequency $\omega_{\text{IF}} = \omega_{\text{s}} - \omega_{\text{ELO}}$ in the megahertz regime, the lower sideband generated by the mixer can be measured on the analog-to-digital converter and subsequently digitally mixed back to ω_{sig} for further analysis, while the higher frequency signal is again filtered out or simply time-averaged.
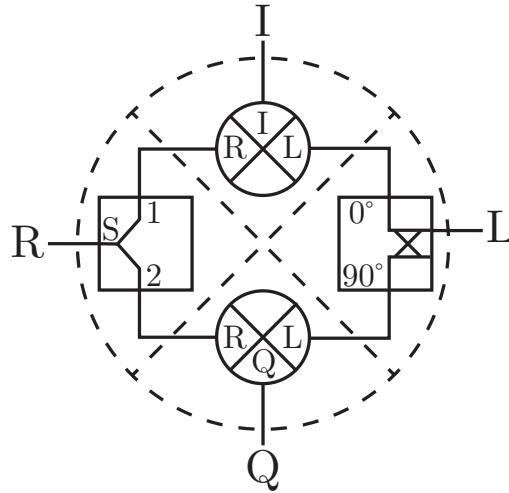
Figure 3.8: Block diagram of an IQ mixer illustrating a microwave signal R divided into two parts by a splitter and the local oscillator L divided into two 90° phase separated parts by a quadrature hybrid. The portions of the signal and local oscillator are then mixed together to produce in-phase I and quadrature Q components of the mixed signal. The dashed lines indicate the common symbol for an IQ mixer: ⊗, where the ports, listed clockwise, are RILQ.

Another approach is to perform electronic downmixing using an IQ-mixer,[23] which is shown in the block diagram Fig. 3.8. IQ mixers internally shift the phase of part of the local oscillator signal, such that when it is mixed with the input microwave signal the product is in-phase and quadrature signals,

$$\text{I} = \frac{A}{2} \left[\cos((\omega_{\text{sig}} + \omega_{\text{ELO}})t + \phi) + \cos((\omega_{\text{sig}} - \omega_{\text{ELO}})t + \phi_{\text{sig}}) \right], \quad (3.24)$$

$$\text{Q} = \frac{A}{2} \left[\sin((\omega_{\text{sig}} + \omega_{\text{ELO}})t + \phi) - \sin((\omega_{\text{sig}} - \omega_{\text{ELO}})t + \phi_{\text{sig}}) \right]. \quad (3.25)$$

Both quadratures of the signal can be low-pass filtered for the difference frequency and detected individually on an analog-to-digital converter. The signals can then be individually processed, or added in-quadrature and processed as a whole, to digitally mix the signal back up to the original frequency and extract information about the signal.

3.3.8 Low-IF Receiver

IQ mixing provides a secondary advantage over both regular electronic downmixing and optical heterodyne downmixing: comparing the quadrature signals provides phase information about coherent modulation signals (e.g., $\phi(t) = \beta \sin(\omega_{\text{sig}} + \phi_{\text{sig}})$). In particular, if a coherent signal is mixed to DC, then the signal phase is measured by comparing quadrature amplitudes,

$$\phi_{\text{sig}} = -\arctan\left(\frac{\text{Q}}{\text{I}}\right). \quad (3.26)$$

Mixing to DC can be achieved directly by setting $\omega_{\text{ELO}} = \omega_{\text{sig}}$, however this introduces significant $1/f$ noise to the detection system [85]. Instead, it is preferable to develop a measurement system known as a low-IF receiver [86], which first mixes the signal to an intermittent frequency (IF) that is subsequently converted into the digital domain, and then digitally mixed to DC to circumvent low frequency noise. To correctly measure the signal phase during this process, the entire system, including the computer used to digitally downmix, must be phase locked. To achieve this, all instruments that produce or measure a frequency are phase locked to a rubidium clock.[24]

---

[23]Marki Microwave IQ1545LMP
[24]Stanford Research Systems FS725 Rubidium Frequency Standard

The low-IF receiver architecture, however, does introduce a new set of complications [87], neither the splitter nor the quadrature hybrid in the IQ mixer are perfect and thus the electronic downmixing process introduces both phase and amplitude imbalances to the in-phase and quadrature signals. To correct these imbalances, we implemented a digital I/Q imbalance procedure [88], which is detailed in Appendix B.

3.3.9   Experimental Implementation

Optical homodyne with downmixing, optical heterodyne, and direct detection all play crucial roles in detecting mechanical motion. Choosing which system to use is largely circumstantial, and therefore in order to remain flexible during the course of an experiment, the optomechanical experimental apparatus is designed for ease of switching between detection methods. The general implementation is shown in Fig. 3.9. Typically, initial measurements are made using direct detection with the real-time spectrum analyzer to avoid the additional complications of matching the local oscillator phase. When the mechanical resonance is identified in direct detection, phase measurements are used for better signal-to-noise and reduced optical heating.

For experiments in this thesis, the choice between optical homodyne with downmixing and optical heterodyne was largely inconsequential—both types of phase measurement are adequate for measuring the mechanical mode. Optical heterodyne does, however, provide two tangible advantages. First, the balanced photodetector[25] has a 3 dB roll off at 800 MHz, which implies that detection is more efficient at the optically-downmixed megahertz signal frequencies. Second, the largest sources of electronic noise occur in the electronics after detection, which are susceptible to acting as antennas for gigahertz signals. By optically downmixing prior to detection, the gigahertz frequency range is entirely avoided by electronics.

Despite the benefits of optical downmixing, there are also perceived advantages provided by optical homodyne with downmixing, which make the trade-offs of lower efficiency, and higher noise, worth making. First, the control loop for keeping the local oscillator and signal arms phase locked tends to be more stable in homodyne

---

[25]Newfocus 1811 balanced photoreciever
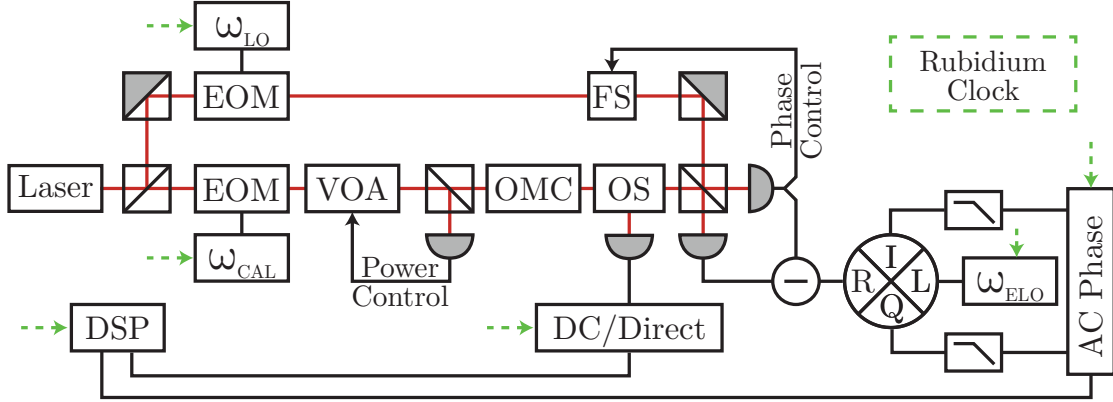
Figure 3.9: Experimental apparatus for optical and mechanical measurements of an optomechanical crystal (OMC). An optical switch (OS) allows the system to transition between direct detection to phase detection. The presence of a drive tone ω_{EOM} on the electro-optic modulator (EOM) in the local oscillator arm determines if the phase measurement is homodyne (absent) or heterodyne (present). An additional beamsplitter directly before the OMC allows for power control by feeding back to a variable optical attenuator (VOA). All signal generators and data collection devices, including the digital signal processing (DSP) computer, are clocked using a rubidium clock.

detection, which allows for longer-term measurements. Second, the measurement detection efficiency of heterodyne occasionally appears to fluctuate—possibly due to the extra tones created by the unfiltered local oscillator. This was a common problem during room temperature experiments, but not during low temperature measurements. As such the optical downmixing of heterodyne was taken advantage of at low temperatures, and the stability of homodyne was used for room temperature experiments. The low-IF receiver was implemented with homodyne downmixing for the purpose of detecting the coherent phase of a transduced microwave tone, which will be further detailed in Chapter 5.

It is also possible to compensate for high-frequency electronics noise through the judicious use of electronic filtering. After the homodyne photodetector, an electrical bandpass filter[26] is used to remove signals outside of the $2250 - 2470$ MHz frequency region and the remaining signal is amplified.[27] After mixing with the local oscillator in the IQ-mixer, the IQ signals are low pass filtered[28] to remove

---

[26]Mini-Circuits VBF2360+ bandpass filter
[27]Two Pasternack PE15A3258 low-noise, broadband 33 dB amplifiers
[28]Mini-Circuits SLP-200+

noise above 190 MHz. Immediately prior to being measured on the analog-to-digital converter, DC-blocks[29] are used to remove signals below 100 kHz. The DC-blocks are also used in heterodyne detection to remove any DC offset that comes from imbalances in the homodyne arms, which could overload the analog-to-digital converter.

3.3.10   Mechanics Signal Processing

The outcome of heterodyne, and homodyne or direct detection with downmixing, is a voltage signal that carries DC information about the optical resonance and megahertz AC information about the mechanical motion. The AC component is converted into a digital time domain signal using an analog-to-digital converter.

The autocorrelation of the AC signal is then Fourier transformed to obtain the power spectral density [89],

$$S_{\mathrm{VV}}(\omega) = \frac{1}{2\pi} \int \langle V(t)(V(t+\tau) \rangle \, e^{-i\omega\tau} d\tau \tag{3.27}$$

which describes how the power of a signal is distributed over frequency. For mechanical motion, the measured power spectral density is of the form [63]

$$S_{VV}(\omega) = S_{VV}^{w} + \alpha x_{\mathrm{zpf}}^2 S_{\hat{b}^\dagger \hat{b}}(\omega), \tag{3.28}$$

where S_{VV}^{w} describes a white-noise background generated by the measurement apparatus, and $x_{\mathrm{zpf}}^2 S_{\hat{b}^\dagger \hat{b}}(\omega)$ is the noise imparted by mechanical motion, which is scaled by a detection factor α. In the case of thermally driven motion, the mechanical power spectral density can be derived using the mechanical equation of motion, Eqn. (2.37), in the absence of optical backaction on the mechanical mode. The thermal power spectral density is given by [1]

$$S_{\hat{b}^\dagger \hat{b}}^{\mathrm{th}}(\omega) = \frac{1}{2\pi} \int \langle \hat{b}^\dagger(\omega)\hat{b}(\omega') \rangle \, d\omega' \tag{3.29}$$

$$= \frac{\Gamma_{\mathrm{m}} \bar{n}_{\mathrm{th}}(\omega_{\mathrm{m}})}{(\omega_{\mathrm{m}} + \omega)^2 + \Gamma_{\mathrm{m}}^2/4}, \tag{3.30}$$

where the thermal input autocorrelation is [33]

$$\langle \hat{b}_{\mathrm{in}}^\dagger(\omega)\hat{b}_{\mathrm{in}}(\omega') \rangle = 2\pi \bar{n}_{\mathrm{th}}(\omega_{\mathrm{m}})\delta(\omega + \omega'), \tag{3.31}$$

---

[29]Mini-Circuits BLK-18-S+

and we recall the number of thermal phonons is $\bar{n}_{\mathrm{th}}(\omega_{\mathrm{m}}) = \left[e^{\hbar\omega_{\mathrm{m}}/k_{\mathrm{B}}T} - 1\right]^{-1}$ for a mechanical mode at temperature T.

The detection factor, which has units $\mathrm{V}^2/\mathrm{m}^2$, represents how well the mechanical motion is converted into a voltage signal and combines factors of both the optomechanical coupling and system detection efficiency. The total amplitude of the measured mechanical peak is therefore

$$\alpha\bar{n}_{\mathrm{th}}x_{\mathrm{zpf}}^2 = |\hat{a}_{\mathrm{in}}|^4\beta_{\mathrm{m}}^2\eta^2(\omega)\mathcal{K}^2(\Delta, \omega_{\mathrm{m}})\kappa_{\mathrm{e}}^2. \tag{3.32}$$

3.3.11 Mechanical Properties
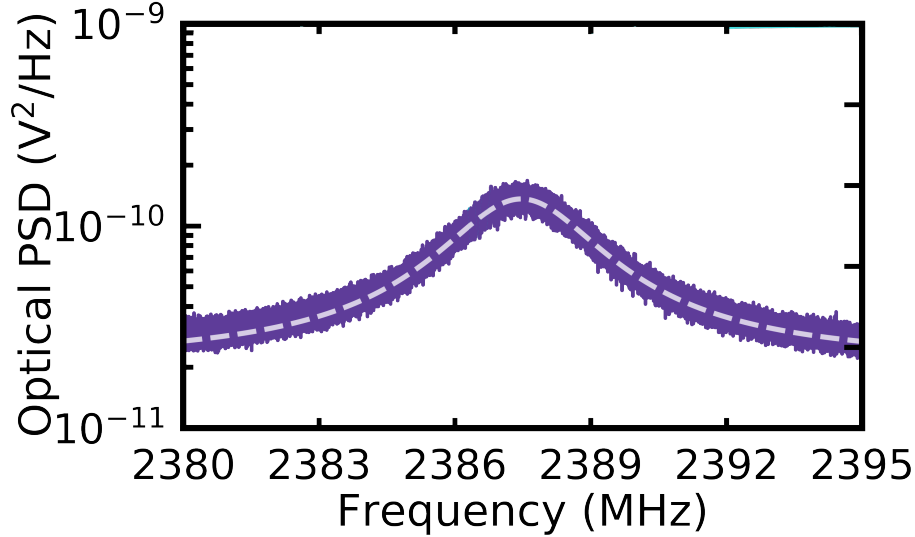
Figure 3.10: Homodyne measurement of the mechanical mode at room temperature and atmospheric pressure, with fit in dashed white using Eqn. (3.28).

In Fig. 3.10, we provide a typical measurement of the mechanical mode measured using homodyne detection with downmixing, in ambient conditions at room temperature and atmospheric pressure for initial calibrations. Using Eqn. (3.28), the resonance is fit to extract the frequency $\omega_{\mathrm{m}}/2\pi \approx 2.388$ GHz and damping rate $\Gamma_{\mathrm{m}}/2\pi \approx 2.9$ MHz. The devices were also explored at low-temperature, which will be discussed in Chapter 6, and in vacuum at a pressure near 10^{-7} Torr. The damping rate was found to be identical in air and vacuum, which implies that the mechanical breathing mode is not limited by viscous air damping. This is atypical of mechanical resonators measured in the Davis lab, and is thought to be a result

of the mechanical motion being faster than the response time of the surrounding air, and the relatively small amplitude of the breathing mode motion.

An ideal measurement of the mechanical mode is made using a fiber that is hovering above the optomechanical crystal, such that it does not provide a path for phonons to escape the mechanical mode. Unfortunately, hover-coupling is difficult to routinely achieve, and often only lasts for a short period before vibrations cause the fiber to latch onto the optomechanical crystal. Once the fiber latches on to the optomechanical crystal, it acts as a source of damping and can also cause slight shifts in the mechanical mode frequency. These effects were noted during experiment, but no systematic study was undertaken to determine ideal coupling conditions for measuring low mechanical damping. Instead, as previously mentioned, fiber position is wholly dictated by the optical coupling, which dictates whether or not enough light from the optical mode couples back into the optical fiber to render the mechanical mode visible.

3.4 Optomechanical Coupling

Several options exist for measuring the optomechanical coupling rate. Historically, the Davis lab has implemented the thermomechanical calibration technique [63], which combines a fit of the mechanical resonance lineshape to calculate $\sqrt{\alpha} = \frac{dV}{dx}$, a simulation of the mechanical mode to calculate the effective mass, and the optical resonance to determine the conversion between wavelength and voltage $\frac{d\omega}{dV}$. Using the chain rule, the thermomechanically calibrated optomechanical coupling is

$$g_0 = \frac{d\omega}{dx} = \frac{d\omega}{dV_{\mathrm{DC}}} \cdot \frac{dV_{\mathrm{AC}}}{dx} x_{\mathrm{zpf}}. \tag{3.33}$$

The thermomechanical calibration technique requires precise knowledge of how the AC and DC signals are manipulated between the photodetector and data processing. Any relative gains, through signal amplification, or losses, through frequency-dependent detection efficiency or attenuation, will result in a scaling factor that must be accounted for in the calculation of the optomechanical coupling. This can often be easily accounted for in the tens-of-megahertz frequency regime,

where electronic gain and attenuation profiles are typically spectrally flat. In the gigahertz frequency regime of optomechanical breathing modes, however, the gain spectra of the detection instruments (in particular, the photodiodes) are less clear, and thermomechanical calibration is therefore less reliable.

Instead, the optomechanical crystal mode coupling is measured via phase calibration, wherein the mechanical modulation of the measurement laser is compared to a known phase modulation source, in this case a second electro-optic phase modulator in the signal arm[30] (see Fig. 3.9), which is driven by a signal generator with known voltage V_{CAL} and frequency ω_{CAL}. As a result, we now describe the optical cavity input field with phase modulation, as we did for the local oscillator in Eqn. (3.21),

$$\hat{a}_{\mathrm{in}}(t) = \hat{a}_{\mathrm{in}} \left[1 - \frac{\beta_{\mathrm{CAL}}}{2} \left(e^{-i\omega_{\mathrm{CAL}}t} - e^{i\omega_{\mathrm{CAL}}t} \right) \right]. \tag{3.34}$$

The phase modulated optical input causes the cavity field, and therefore the cavity transmission, to fluctuate at both the calibration tone frequency and the mechanical frequency (see Appendix A). The EOM calibration frequency is set to be near the mechanical resonance to ensure that the fluctuations imparted on the optical signal are measured with the same system detection efficiency as the mechanical fluctuations. For a direct detection measurement, the corresponding voltage output by the photodetector is

$$V_{\mathrm{AC}}(t) = \eta(\omega) \frac{|\hat{a}_{\mathrm{in}}|^2 \kappa_{\mathrm{e}}}{2} \mathcal{K}_{\mathrm{dir}}(\Delta) \left(\beta_{\mathrm{m}} \frac{x(t)}{x_0} - \beta_{\mathrm{CAL}} \phi(t) \right), \tag{3.35}$$

where we have applied a bandpass filter around the mechanical resonance $\frac{x(t)}{x_0} = \cos(\omega_{\mathrm{m}}t)$ and calibration tone $\phi(t) = \sin(\omega_{\mathrm{CAL}}t)$. We note that the mechanical resonance has been normalized, as the amplitude due to thermal motion has been included in the modulation index.

We now further restrict the calibration frequency to be near, but not equal to the mechanical frequency so that there is little overlap between the two. This allows us to separate the calculated power spectral density into two parts,

$$S_{VV}(\omega) - S_{VV}^w = \alpha x_{\mathrm{zpf}}^2 S_{\hat{b}^\dagger \hat{b}}^{\mathrm{th}}(\omega) + \alpha_{\mathrm{CAL}} \delta(\omega - \omega_{\mathrm{CAL}}), \tag{3.36}$$

---

[30]Thorlabs LN65S 10 GHz phase modulator, $V_\pi = 4.1$ V

where the power spectral density of the phase calibration tone is represented by a delta function, with amplitude $\alpha_{\mathrm{CAL}} = |\hat{a}_{\mathrm{in}}|^4 \beta_{\mathrm{CAL}}^2 \eta^2(\omega) \mathcal{K}^2(\Delta) \kappa_{\mathrm{e}}^2$.
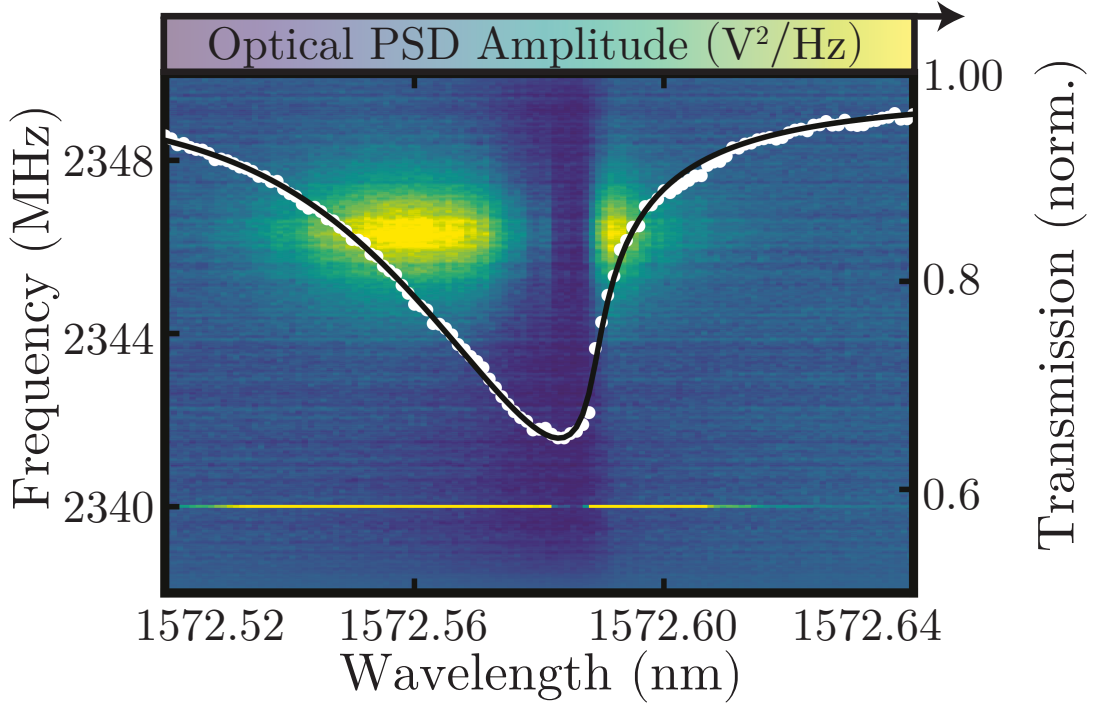
Figure 3.11: Direct detection measurement of a 620 nm optomechanical crystal. DC transmission (white) of the optical resonance (fit in black) and measured AC frequency spectrum at each 1 pm laser wavelength step (plot background with colour-scale spectrum amplitude). The mechanical mode appears near 2347 MHz, and an electro-optic phase modulator calibration tone is visible at 2340 MHz.

In Fig. 3.11, a direct detection measurement of a optomechanical crystal with beam width of 620 nm is made simultaneously by stepping the laser frequency across the optical resonance and measuring DC optical transmission and AC sideband modulation at each wavelength increment. The mechanics and the electro-optic phase modulator appear at 2347 MHz and 2340 MHz respectively, in two lobes which correspond to the regions of high slope of the optical resonance. The electro-optic phase modulator, calibrated in Appendix A, shifts the phase of the laser by π when the half-wave voltage $V_\pi = 4.1$ V is applied to the RF input. For the purpose of phase calibration, we apply a much weaker modulation signal $V_{\mathrm{CAL}} = 10$ mV at $\omega_{\mathrm{CAL}}/2\pi = 2340$ MHz to induce a maximum phase shift $\beta_{\mathrm{CAL}} = \frac{\pi V_{\mathrm{CAL}}}{V_\pi} \approx 0.01$ rad.

The mechanical modulation index, Eqn. (3.7) can be made an experimentally

tractable using equipartition theorem, which relates the average potential energy $\langle U \rangle$ and the thermal energy of the mechanical mode [40, 63]

$$\langle U \rangle = \frac{1}{2} m_{\text{eff}} \omega_{\text{m}}^2 x_0^2 = \frac{1}{2} k_{\text{B}} T. \tag{3.37}$$

By rearranging Eqn. (3.7) in terms of x_0, substituting the result into Eqn. (3.37), and solving for β_{m}, the mechanical modulation index is

$$\beta_{\text{m}} = \sqrt{\frac{2 k_{\text{B}} T}{\hbar \omega_{\text{m}}^3}} g_0. \tag{3.38}$$

Hence, the mechanical modulation strength is linearly related to optomechanical coupling as well as the square root of temperature. By comparing the known modulation strength of the EOM to the modulation strength of the mechanics in an environment with known temperature, the optomechanical coupling can be calculated.

The frequency separation allows us to consider the mechanical and modulation peak areas individually. The mechanical peak can either be directly integrated or the area can be extracted from the fit,

$$\mathcal{P}(\omega_{\text{m}}) = \int_{\omega_{\text{m}}} (S_{VV}(\omega) - S_{VV}^w) \, d\omega = \frac{S_{VV}(\omega_{\text{m}}) \Gamma_{\text{m}}}{2} = \alpha \beta_{\text{m}}^2. \tag{3.39}$$

The modulation peak in contrast typically has linewidth less than the frequency resolution of the power spectral density, the power in the modulation peak can therefore be calculated as

$$\mathcal{P}(\omega_{\text{CAL}}) = \int_{\omega_{\text{cal}}} (S_{VV}(\omega) - S_{VV}^w) \, d\omega = \frac{S(\omega_{\text{CAL}}) \cdot \text{ENBW}}{2} = \alpha \beta_{\text{CAL}}^2, \tag{3.40}$$

where ENBW is the effective-noise-bandwidth of the Fourier transform, which is set by the frequency spacing of points,

$$\text{ENBW} = \frac{\text{RATE}}{\text{NFT}}. \tag{3.41}$$

Where RATE is the rate at which voltage data is collected, and NFT is the number of points included in the Fourier transform. Comparing the integrated power spectral densities, and substituting Eqn. (3.38) for β_{m}, we arrive at an

experimentally measurable equation for the optomechanical coupling,

$$g_0 = \sqrt{\frac{\hbar\omega_{\mathrm{m}}^3}{2k_{\mathrm{B}}T}\beta_{\mathrm{CAL}}^2\frac{\mathcal{P}(\omega_{\mathrm{m}})}{\mathcal{P}(\omega_{\mathrm{CAL}})}} \tag{3.42}$$

$$= \sqrt{\frac{\hbar\omega_{\mathrm{m}}^3}{2k_{\mathrm{B}}T}\left(\frac{\pi V_{\mathrm{CAL}}}{V_\pi}\right)^2\frac{S_{VV}(\omega_{\mathrm{m}})\Gamma_{\mathrm{m}}}{S_{VV}(\omega_{\mathrm{CAL}})\cdot\mathrm{ENBW}}}. \tag{3.43}$$

In contrast to thermomechanical calibration, the optomechanical coupling calculated using Eqn. (3.42) is independent of the optical resonance and only depends on frequency in the narrow region between the calibration frequency and the mechanical frequency. As a result, phase calibration is robust against frequency dependent gains and provides an accurate measure of the optomechanical coupling for high frequency mechanical modes.
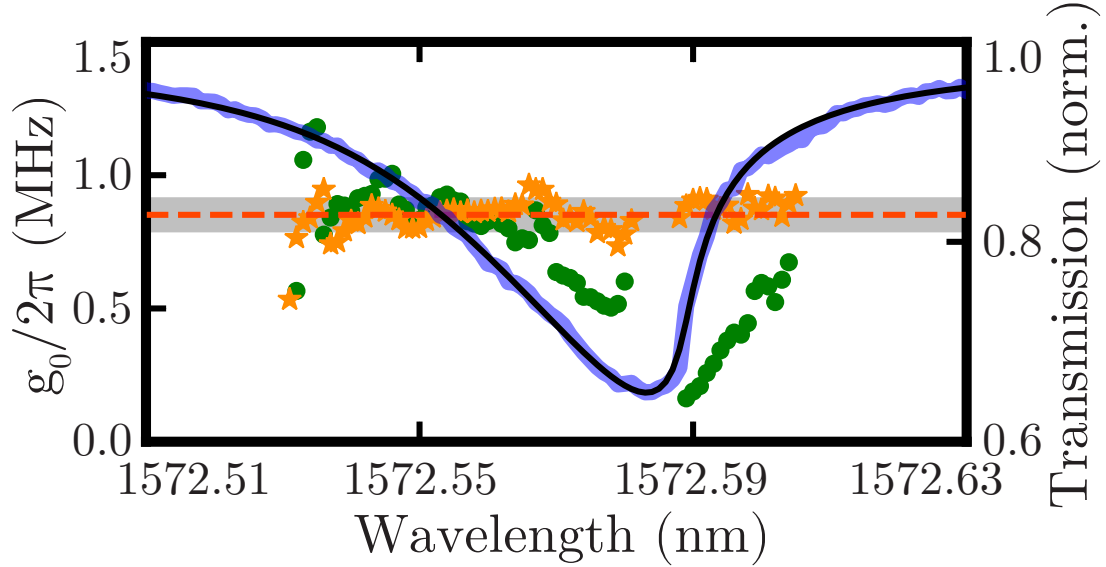
Figure 3.12: Calculation of the optomechanical coupling using phase calibration (orange stars) and thermomechanical calibration (green circles), with the optical resonance (blue) as reference for the detuning at which each calculation is made. The red dashed line depicts the mean phase calibrated g_0 measurement surrounded by a 1σ standard deviation. Measurements were made on a 620 nm wide optomechanical crystal.

In Fig. 3.12, the power spectral density measurement from Fig. 3.11 is condensed into a phase calibration calculation of g_0 using Eqn. (3.42), and a thermomechanical calibration calculation using Eqn. (3.33), at every wavelength step. Near the slope maxima of the optical resonance, where the signal strength of direct detection is

maximized, the phase-calibrated optomechanical coupling is consistently measured to be $g_0/2\pi = (0.90 \pm 0.05)$ MHz. The calculated values for thermomechanical calibration and phase calibration on the blue detuned ($\omega_\ell < \omega_c$) side of the optical resonance are similar, which suggests that the AC and DC signal gains have been scaled appropriately. The red detuned calculations, particularly at 1572.59 nm, differ greatly. The optomechanical coupling is independent of detuning, so we may assume that the thermomechanical calibration value is incorrect, and speculate that the non-linearity of the optical resonance caused by the thermorefractive effect invalidates the straightforward application of the chain rule in Eqn. (3.33).

In this Section, we have phase calibrated a 620 nm wide optomechanical crystal at room temperature, whereas the rest of the experiments in this thesis make use of a 600 nm wide optomechanical crystal. The difference in nanobeam width causes the experiments in this section to have slightly shifted wavelength and mechanical resonance frequencies. Using the same phase calibration procedure illustrated here, in Chapter 6 we measure the optomechanical coupling of the 600 nm optomechanical crystal to be $g_0/2\pi = (1.3 \pm 0.3)$ MHz at low temperature.

3.4.1 Dynamical Backaction

In addition to calculating the optomechanical coupling, the detuning measurements presented in Fig. 3.11 can be used to investigate the dynamical backaction effects in the 620 nm wide optomechanical crystal. In Fig. 3.13, the parameters found by fitting the optical and mechanical modes for a range of detunings, are used to calculate the optomechanical spring and damping effects. The directly measured mechanical mode frequency shift is demonstrated to roughly agree with the calculated optomechanical spring effect, but the change in measured optomechanical damping shows no similarity to the optomechanical damping effect. Since the damping effect is predicted to be on the order of 100 kHz, we conclude that extraneous effects, such as the unaccounted for nonlinearity in the optical resonance, wash out our ability to detect optomechanical damping.
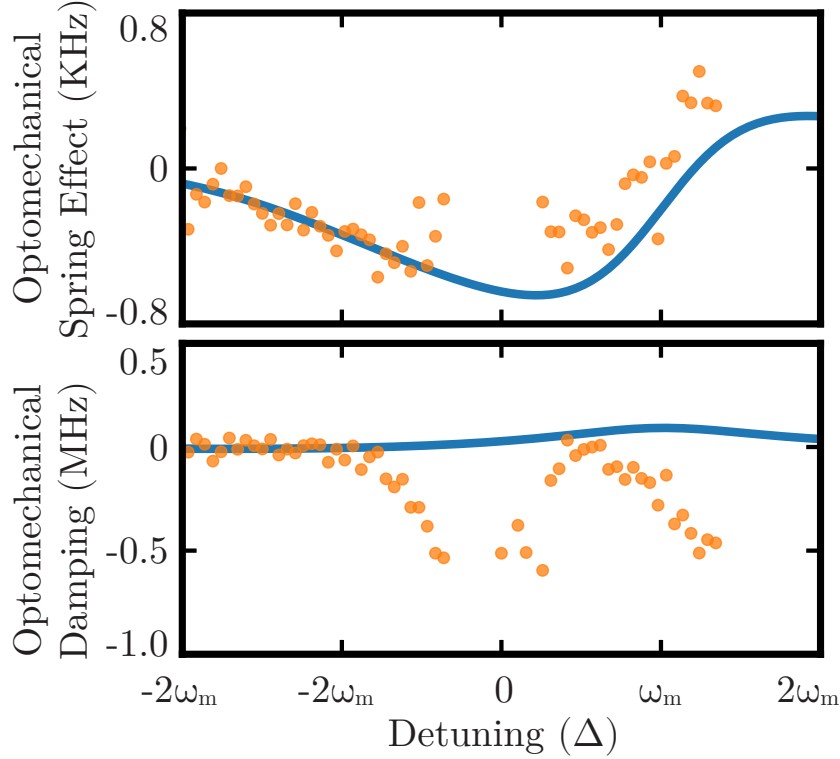
Figure 3.13: (Top, orange dots) Change in measured mechanical frequency and (bottom, orange dots) mechanical damping as a function of detuning. The blue lines represent the expected (top) optomechanical spring effect and (bottom) optomechanical damping calculated using Eqns. (2.42, 2.43), using parameters extracted from fits of the measured mechanical resonances.

3.5 Methods Summary

In this Chapter, we have highlighted the three primary methods of optomechanical measurement used in this thesis:

1. direct detection for DC measurement of the optical resonance, and AC measurement of the mechanical resonance when combined with a real-time spectrum analyzer or downmixing;

2. homodyne detection with downmixing for high-sensitivity, low-power measurements of the mechanical mode, which can be combined with a low-IF receiver for phase measurements of the modulation signal;

3. heterodyne detection for optical downmixing of the mechanical mode frequency, which similarly allows for high-sensitivity, low-power measurements

and further circumvents high-frequency noise picked up by measurement electronics.

Using these methods, we present typical measurements of the optical mode, the mechanical mode, and the optomechanical interaction in Table 3.1 for room temperature operation of the standard 600 nm optomechanical crystal. These measurements are in-line with measurements from other groups of similar gallium arsenide optomechanical crystals [27, 29, 40].

	Optical Mode	Mechanical Mode
Wavelength	$\lambda_c \approx 1550$ nm	—
Frequency	$\omega_c/2\pi \approx 194$ THz	$\omega_m/2\pi \approx 2.38$ GHz
Total decay rate	$\kappa/2\pi \approx 6$ GHz	$\Gamma_m/2\pi \approx 2.9$ MHz
External decay rate	$\kappa_e/2\pi \approx 2$ GHz	—
Optomechanical coupling	$g_0/2\pi = (1.3 \pm 0.3)$ MHz	
Cooperativity	$C = \bar{n}_{cav} \times 10^{-4}$	

Table 3.1: Summary of room temperature optomechanical properties of the gallium arsenide optomechanical crystal.

Ideally, the optical and mechanical decay rates, and the optomechanical coupling can be combined into the cooperativity,

$$C = \frac{4g_0^2 \bar{n}_{cav}}{\kappa \Gamma_m} \approx \bar{n}_{cav} \times 10^{-4}, \tag{3.44}$$

which scales with the number of cavity photons $\bar{n}_{cav} = \langle \hat{a}^\dagger \hat{a} \rangle$ due to the parametric nature of the optomechanical interaction. Here we have used typical values discussed throughout this chapter for the optical and mechanical decay rates. The cooperativity represents the ratio of energy transferred between the optical and mechanical mode to the rate of energy loss in each mode. By increasing the number of cavity photons to $\bar{n}_{cav} \approx 10000$ such that $C > 1$, energy transduction between the modes will occur preferentially to energy loss, which is a requirement for high-efficiency microwave-to-telecom transduction. However, high cavity photon occupancy will cause large amounts of optical heating at low temperatures, which will result in additional thermal noise in a transduced signal. We will explore this further during our low-temperature calibration of the optomechanical crystal in Chapter 6.

Chapter 4

Piezomechanics

In Chapter 1, several possible methods of wavelength transduction were introduced. Of those using mechanical modes, there are two approaches to coupling microwave photons to mechanical phonons. The first is through electromechanical coupling, where one terminal of a capacitor in a LC circuit acts as a mechanical element. As the mechanical element moves the capacitance changes, which in turn changes the resonance frequency of the LC circuit. This architecture is most easily implemented for membranes which vibrate at frequencies below 10 MHz, and as such wavelength transducers that use the electromechanical interactions are thus far limited by thermal noise [23–25]. The second mechanism is piezomechanical coupling, where piezoelectric materials are used to couple mechanical motion to microwave fields through electric dipoles in the material itself. As a result, piezomechanical coupling is a more flexible method of creating interaction between microwaves and mechanics, and allows microwaves to be coupled to optomechanical crystal breathing modes [26–31].

4.1   Piezoelectricity

Taking advantage of piezoelectric coupling requires that the device used is made from a material exhibiting the piezoelectric effect. In general, piezoelectric materials are crystalline structures which become electrically polarized as they are mechanically strained, in turn creating an electric displacement [90]. The opposite is also true: as a piezoelectric material is polarized by an electric field, it will induce strain in the material lattice which causes deformation—the converse piezoelectric

57

effect.

The piezoelectric effect is derived using the electrical displacement $\mathbf{D}$ of a material due to an electric field $\mathbf{E}$,

$$\mathbf{D} = \boldsymbol{\epsilon}\mathbf{E} \tag{4.1}$$

and Hooke's law relating strain $\mathbf{S}$ to stress $\mathbf{T}$,

$$\mathbf{S} = \mathbf{s}\mathbf{T}, \tag{4.2}$$

where $\boldsymbol{\epsilon}$ is the material permittivity, and $\mathbf{s}$ is the material compliance. These equations are then coupled together using a coupling matrix $\mathbf{d}$, which is transposed for the converse piezoelectric effect [91, 92]

$$\mathbf{S}_{ij} = \mathbf{s}_{ijkl}\mathbf{T}_{kl} + (\mathbf{d}_{ijk})^{\mathrm{T}}\mathbf{E}_k \tag{4.3}$$

$$\mathbf{D}i = \mathbf{d}_{ijk}\mathbf{T}_{jk} + \boldsymbol{\epsilon}_{ij}\mathbf{E}j. \tag{4.4}$$

Here we have used subscript indices to denote dimensionality of each component of the piezoelectric equations. However the equations are commonly represented using Voigt notation [91], which exploits symmetry to reduce the rank of the matrices by 1. For the piezoelectric matrix in particular, $\mathbf{d} = d_{ijk}$, the indices $j, k \in \{1, 2, 3\}$ are subject to the transformation $j, k \to j'$: $1, 1 \to 1$; $2, 2 \to 2$; $3, 3 \to 3$; $2, 3 \to 4$; $1, 3 \to 5$; $1, 2 \to 6$. The result of the Voigt notation is that $j' \in \{1, 2, 3\}$ represent extensional couplings, whereas $j' \in \{4, 5, 6\}$ represent shear rotations around the 1, 2, and 3 axes respectively. This is most easily visualized in Fig. 4.1, where the 1, 2, and 3 axes are identified as the x, y, and z directions.

Applying Voigt notation to the converse piezoelectric effect, Eqn. 4.3, and neglecting the stress-strain relationship for the moment, the relationship between strain caused by the application of an electric field is explicitly written in strain-charge form as:

$$\begin{bmatrix} S_1 \\ S_2 \\ S_3 \\ S_4 \\ S_5 \\ S_6 \end{bmatrix} = \begin{bmatrix} d_{11} & d_{12} & d_{13} & d_{14} & d_{15} & d_{16} \\ d_{21} & d_{22} & d_{23} & d_{24} & d_{25} & d_{26} \\ d_{31} & d_{32} & d_{33} & d_{34} & d_{35} & d_{36} \end{bmatrix}^{\mathrm{T}} \begin{bmatrix} E_1 \\ E_2 \\ E_3 \end{bmatrix}. \tag{4.5}$$
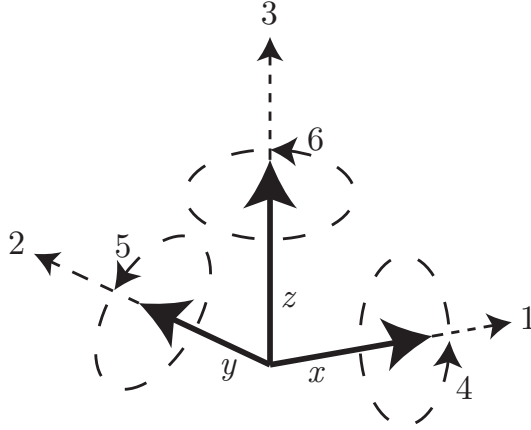
Figure 4.1: The transformations represented by Voigt notation. The indices 1, 2, and 3 are linear transforms along x, y, and z respectively, and the indices 4, 5, and 6 are similarly shear rotation transforms.

Hence, Voigt notation allows us to write $S_{j'} = [d_{ij'}]^{\mathrm{T}} E_i$, such that the element $d_{ij'}$ in piezoelectric matrix represents the strain caused in the j' direction by an electric field applied in the i direction. In Fig. 4.2, this is demonstrated for a cube of piezoelectric material that has only one non-zero piezoelectric coupling element per simulation. In this simulation, we fix the electric field to be oriented along the z-axis, with the understanding that aligning the field to x and y yield identical results.

In a physical material system, the piezoelectric coupling matrix is determined by crystal structure. Gallium arsenide, the material used for the experiments in this thesis, has a cubic crystal structure and is part of the $\bar{4}3m$ point group, which defines the crystal symmetry and results in the structure of the piezoelectric coupling matrix [93],

$$\mathbf{d} = \begin{bmatrix} 0 & 0 & 0 & d_{14} & 0 & 0 \\ 0 & 0 & 0 & 0 & d_{25} & 0 \\ 0 & 0 & 0 & 0 & 0 & d_{36} \end{bmatrix}, \tag{4.6}$$

where $d_{14} = d_{25} = d_{36} = 2.6 \times 10^{-12}$ C/N [94]. The units of the coupling matrix are typically written in terms of C/N, which is exactly the inverse of the electric field units, V/m. The strain that results is unitless as it describes a deformation, which is the change in length per total length.
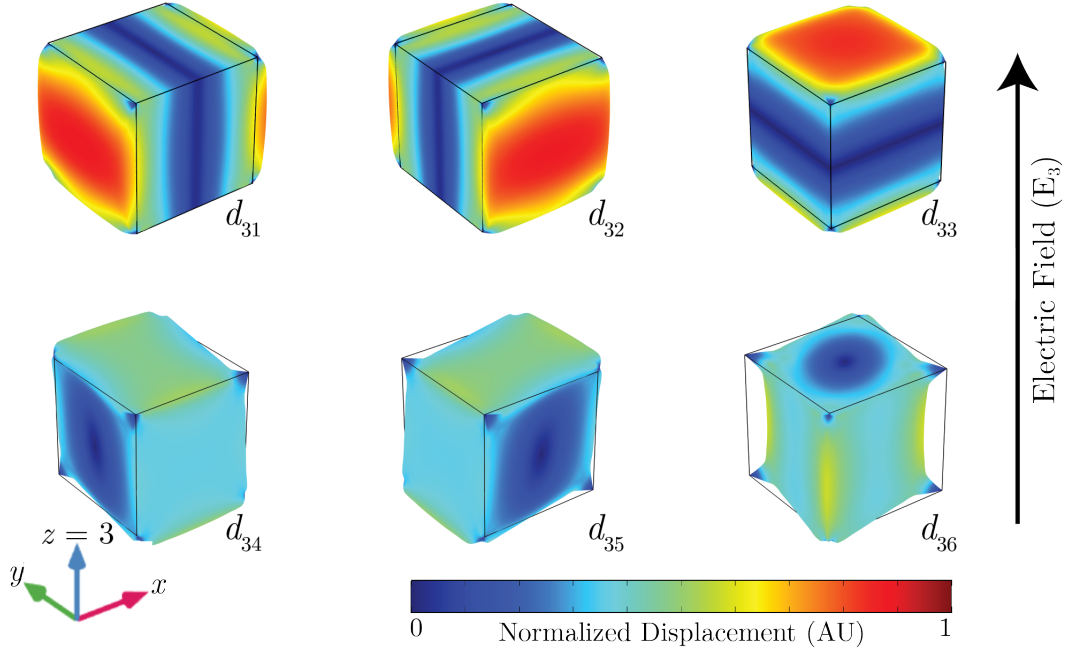
Figure 4.2: The effect of the piezoelectric coupling matrix is demonstrated using six boxes of "single element" piezoelectric material in a z-oriented ($i = 3$) electric field. Each box shows the displacement induced by the indicated piezoelectric coupling matrix element, while all other elements are set to zero. Simulations for x- and y-oriented ($i = 1, 2$) electric fields will yield identical results. The simulation software has handled the additional step of converting the stress into a static displacement.

4.2 Simulation of piezoelectricity in gallium arsenide optomechanical crystals

The next step is to use Eqn. 4.3 to simulate the effect of an electric field on a gallium arsenide optomechanical crystal. To do this accurately, careful consideration of reference frames must be taken into account. Demonstrated in Fig. 4.3, the material axes x, y, and z lie along the gallium arsenide crystal axes. A second set of coordinate axes, the device frame, is shown to be rotated around the z axis such that the device axes u and v are offset by an angle Φ from the material frame. The optomechanical crystal is oriented such that the long axis lies in the u direction.

In Ref. [40], it was demonstrated that optomechanical coupling was maximized at the device angle $\Phi = 45°$. As a result, the devices used for the experiments in this thesis are fixed to this angle such that the long axis of the optomechanical crystal
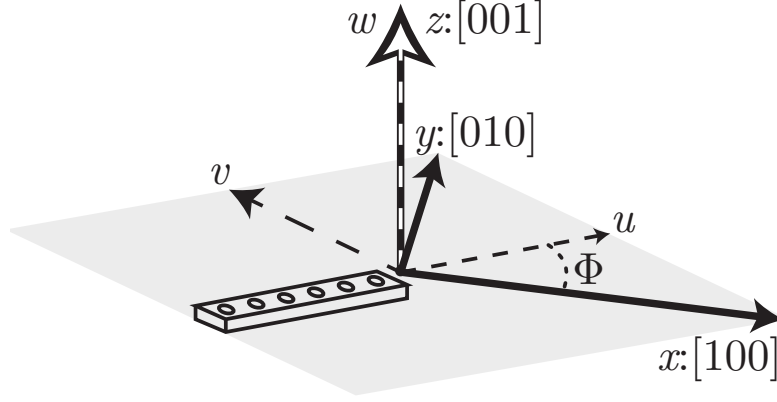
Figure 4.3: Device orientation u relative to the material orientation x, y, z.

is aligned to the crystallographic [110] axis. With the crystal orientation of the optomechanical crystals fixed, the remaining tunable parameter for piezomechanical coupling is the electric field orientation. The static response of the optomechanical crystal in various DC electric fields, shown in Fig. 4.4, allows us to perform initial qualitative assessments of the displacement caused by electric fields, whereas simulation of a resonant AC electric field is required to fully assess the effect of the electric field on the breathing mode.
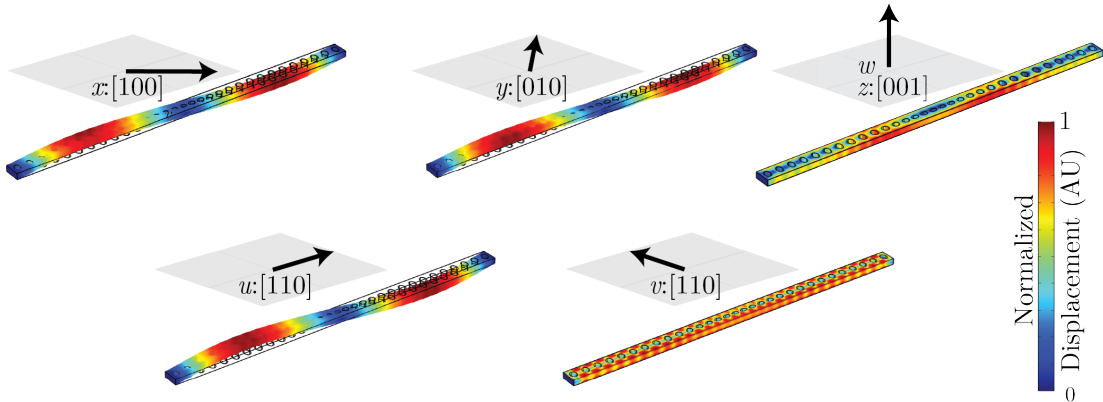
Figure 4.4: The GaAs optomechanical crystal, clamped at either end of the long axis and statically displaced by DC electric fields (black arrows with labelled directions) aligned to the material frame (top row) and the device frame (bottom row).

In Fig. 4.4, the static piezoelectric response of the gallium arsenide optomechanical crystals is simulated for five directions of DC electric field. The x, y, u, v

directions cause out-of-plane displacement, but close inspection of these simulations reveals that the piezoelectric coupling matrix does not have the anticipated effect—for example, the u-oriented electric field causes displacement that suggests a non-zero $d_{1,5}$ element, while the v-oriented electric field suggests a non-zero $d_{2,4}$ element. This is the result of a 45° rotation transformation on the piezoelectric coupling matrix, which is the result of the [110] alignment of the optomechanical crystal. In a scenario where the device is not rotated, the coupling between the electric field and the displacement appears as expected. In contrast, the z-oriented DC electric field generates the expected in-plane static displacement, which is likely to couple to the mechanical breathing mode of the optomechanical crystal.
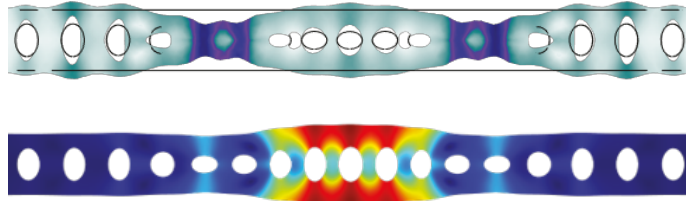
Figure 4.5: Top: Dynamic GaAs nanobeam response to a z-oriented AC electric field, which oscillates at mechanical resonance frequency. Bottom: The mechanical breathing mode for comparison.

To further demonstrate the qualitative overlap between the piezoelectrically-induced motion and the mechanical breathing mode, in Fig. 4.5 the optomechanical crystal is then simulated in a z-oriented AC electric field which oscillates at the breathing mode resonance frequency. The similarity between the modes qualitatively suggests that a microwave cavity with a z-oriented field should drive the mechanical breathing mode.

4.3 Piezomechanical formalization

The piezomechanical coupling between microwave and mechanical modes, with resonance frequencies ω_μ and ω_m respectively, can be quantified by developing the Hamiltonian for the piezomechanical system. To begin, the total energy of the

piezomechanical system is [74, 91, 92]

$$U_{\mathrm{pm}} = \frac{1}{2} \int_V \mathbf{T} \cdot \mathbf{S} + \mathbf{E} \cdot \mathbf{D} \, dV \tag{4.7}$$

$$\tag{4.8}$$

which, using Eqns. (4.1, 4.2) to make subsitutions for strain $\mathbf{S}$ and electrical displacement $\mathbf{D}$, can be separated into three parts according to where the energy is stored. The elastic and electrical energy are respectively

$$U_{\mathrm{e}} = \frac{1}{2} \int_V \mathbf{T} \cdot \mathbf{s} \cdot \mathbf{T} \, dV, \tag{4.9}$$

$$U_{\mathrm{d}} = \frac{1}{2} \int_V \mathbf{E} \cdot \boldsymbol{\epsilon} \cdot \mathbf{E} \, dV, \tag{4.10}$$

and the mutual energy representing the interaction is

$$U_{\mathrm{m}} = \frac{1}{4} \int_V \mathbf{T} \cdot \mathbf{d}^{\mathrm{T}} \cdot \mathbf{E} + \mathbf{E} \cdot \mathbf{d} \cdot \mathbf{T} \, dV. \tag{4.11}$$

Thus the total energy of the system is

$$U_{\mathrm{pm}} = U_{\mathrm{e}} + 2U_{\mathrm{m}} + U_{\mathrm{d}}. \tag{4.12}$$

The mechanical stress and the electric field displacement can then be quantized as harmonic oscillators with normalized amplitudes [74]:

$$\mathbf{T} = \sum_{\mathrm{m}} \mathbf{T}_{\mathrm{m}} \left(\hat{b}_{\mathrm{m}} + \hat{b}_{\mathrm{m}}^{\dagger} \right), \tag{4.13}$$

$$\mathbf{E} = \sum_{\mu} \mathbf{E}_{\mu} \left(\hat{c}_{\mu} + \hat{c}_{\mu}^{\dagger} \right). \tag{4.14}$$

To consider a single mechanical and microwave mode, we now drop the subscripts for $\hat{b}^{\dagger}, \hat{b}$ and $\hat{c}^{\dagger}, \hat{c}$, which are the creation and annihilation operators for phonons and microwave photons respectively. For the microwave and mechanical mode of choice, the corresponding piezomechanical Hamiltonian is [95]

$$\mathcal{H}_{\mathrm{pm}} = \hbar \omega_{\mathrm{m}} \hat{b}^{\dagger} \hat{b} + \hbar \omega_{\mu} \hat{c}^{\dagger} \hat{c} + \hbar g_{\mu} (\hat{b}^{\dagger} + \hat{b})(\hat{c}^{\dagger} + \hat{c}), \tag{4.15}$$

where ω_{m} and ω_{μ} are the mechanical and microwave frequencies, and

$$g_{\mu} = \frac{1}{2} \int_V \mathbf{T}_{\mathrm{m}} \cdot \mathbf{d}^{\mathrm{T}} \cdot \mathbf{E}_{\mu} + \mathbf{E}_{\mu} \cdot \mathbf{d} \cdot \mathbf{T}_{\mathrm{m}} \, dV \tag{4.16}$$

is the piezomechanical coupling strength. The piezomechanical Hamiltonian differs from the optomechanical Hamiltonian, Eqn. (2.31), in that the interaction term between the microwave and mechanical modes is immediately linear in nature, without the need for any linearization process where the field would be normalized about an average amplitude. As a consequence, the piezomechanical coupling differs from the optomechanical coupling in that it cannot be cavity enhanced by a microwave pump. Instead, the piezomechanical coupling relies solely on the overlap of the mechanical stress and electric field, as demonstrated by Eqn. (4.16).

Using the piezomechanical Hamiltonian, the coupled mechanical and microwave equations of motion are derived using Heisenberg's equation, Eqn. (2.9). In frequency space the equations of motion are

$$i\omega\hat{b}(\omega) = i\omega_\mathrm{m}\hat{b}(\omega) + ig_\mu\left(\hat{c}^\dagger(\omega) + \hat{c}(\omega)\right) + i\frac{\Gamma_\mathrm{m}}{2}\hat{b}(\omega) + \sqrt{\Gamma_\mathrm{m}}\hat{b}_\mathrm{in}(\omega), \qquad (4.17)$$

$$i\omega\hat{c}(\omega) = i\omega_\mu\hat{c}(\omega) + ig_\mu\left(\hat{b}^\dagger(\omega) + \hat{b}(\omega)\right) + i\frac{\kappa_\mu}{2}\hat{c}(\omega) + \sqrt{\kappa_{\mu,\mathrm{e}}}\hat{c}_\mathrm{in}(\omega). \qquad (4.18)$$

In addition to the resonance frequency and coupling terms that arise from the closed-system Hamiltonian, the mechanical mode is further characterized by coupling to the external environment through the damping rate Γ_m and to the thermal bath input $\hat{b}_\mathrm{in}$. The microwave mode is similarly coupled to the external environment through a total decay rate κ_μ, as well as the external decay rate $\kappa_{\mu,\mathrm{e}}$, which couples to an input port $\hat{c}_\mathrm{in}$ that can be used to drive the microwave cavity.

The piezomechanical equations of motion can now be used to describe the number of microwave-actuated phonons, which are the phonons in the mechanical mode that arise from a drive tone in the microwave mode. In Appendix C, we provide a detailed derivation of the following equations where assumptions are limited, so that they can be more generally applied to piezo-optomechanical systems. Here, we make the simplifying assumptions that the counter-rotating terms are small and can be omitted, and assume that the microwave cavity is being driven by a powerful input signal that dominates thermal noise in the cavity, as well as any signal that is transduced in reverse (from the mechanics to the microwave cavity).

Hence, the equations of motion are solved for their respective operators,

$$\hat{b}(\omega) = -\frac{ig_\mu \hat{c}(\omega) + \sqrt{\Gamma_\mathrm{m}}\hat{b}_\mathrm{in}(\omega)}{i\left(\omega_\mathrm{m} - \omega\right) + \Gamma_\mathrm{m}/2} \tag{4.19}$$

$$\hat{c}(\omega) = -\frac{\sqrt{\kappa_{\mu,\mathrm{e}}}\hat{c}_\mathrm{in}(\omega)}{i\left(\omega_\mu - \omega\right) + \kappa_\mu/2}. \tag{4.20}$$

Substituting Eqn. (4.20) into Eqn. (4.19) and separating the result into two parts, the mechanical mode is shown to have distinct thermal and microwave driven components,

$$\hat{b}(\omega) = \frac{ig_\mu\sqrt{\kappa_{\mu,\mathrm{e}}}\hat{c}_\mathrm{in}(\omega)}{\left[i\left(\omega_\mathrm{m} - \omega\right) + \Gamma_\mathrm{m}/2\right]\left[i\left(\omega_\mu - \omega\right) + \kappa_\mu/2\right]} + \frac{\sqrt{\Gamma_\mathrm{m}}\hat{b}_\mathrm{in}(\omega)}{i\left(\omega_\mathrm{m} - \omega\right) + \Gamma_\mathrm{m}/2}. \tag{4.21}$$

We now consider a situation in which the microwave mode has been populated with a signal tone of microwave photons at frequency ω_s. Through the piezomechanical coupling between the modes, the mechanical mode becomes populated with phonons at the same frequency. The number of microwave-actuated phonons in the mechanical mode can be found integrating the power spectral density of the first term in Eqn. (4.21) such that,

$$\bar{n}_\mathrm{s}(\omega_\mathrm{s}) = \frac{1}{2\pi}\int S^s_{\hat{b}^\dagger\hat{b}}(\omega)d\omega \tag{4.22}$$

$$= \frac{1}{(2\pi)^2}\int\int \langle\hat{b}^\dagger(\omega)\hat{b}(\omega')\rangle\, d\omega' d\omega \tag{4.23}$$

$$= \frac{P_\mathrm{s}}{\hbar\omega_\mathrm{s}}\frac{g_\mu^2\kappa_{\mu,\mathrm{e}}}{\left[(\omega_\mathrm{m} - \omega_\mathrm{s})^2 + \Gamma_\mathrm{m}^2/4\right]\left[(\omega_\mu - \omega_\mathrm{s})^2 + \kappa_\mu^2/4\right]}. \tag{4.24}$$

The frequency space distribution of the microwave-actuated phonons depends on the spectral linewidth of the microwave source. In this case, the microwave signal generator is modelled to be nearly a delta function, with linewidth less than the resolution of the detection setup. If the mechanical and microwave resonance frequencies are identical and the signal frequency is also set to be on-resonance, then the number of microwave-actuated phonons in the mechanical mode simplifies to

$$\bar{n}_\mathrm{s} = \left(\frac{16g_\mu^2\kappa_{\mu,\mathrm{e}}}{\Gamma_\mathrm{m}^2\kappa_\mu^2\hbar\omega_\mathrm{s}}\right)P_\mathrm{s}, \tag{4.25}$$

which is a linear equation relating the power of the microwave input directly to the number of phonons. Since $\kappa_{\mu,\mathrm{e}}, \Gamma_\mathrm{m}$, and κ_μ are all independently measurable, this allows for the experimental calculation of the piezomechanical coupling if $\bar{n}_\mathrm{s}$ can be measured.

4.4 Future Outlook of Piezomechanics

In this Chapter, we have developed the Hamiltonian Eqn. (4.15) and equations of motion Eqns. (4.19, 4.20) from the first principles of piezoelectricity, Hooke's Law and the definition of electrical displacement. Using these equations of motion, we derived equations to characterize the piezomechanical interaction, which in the next chapter will allow us to calculate the bandwidth of transduction and calibrate piezomechanical coupling.

Beyond that, there are a number of interesting, as-of-yet unexplored facets of piezoemechanics that are left to future projects. Most importantly, the form of the piezomechanical coupling given in Eqn. (4.16) can be used to simulate the piezomechanical coupling [74] for an arbitrary device, similar to the use of Eqn. (2.52) to simulate the moving boundary optomechanical coupling [96]. Simulation of piezomechanics provides a route towards optimization, which creates a path for continuous improvement of piezomechanical devices. Other groups further suggest that there may be photoelastic coupling between microwaves and mechanics [95], which could allow for interesting interplay between linear and non-linear coupling in piezomechanical systems. Our approach to piezomechanical interactions has been surgical rather than exploratory in nature, and it is likely that exploratory research into piezomechanical coupling through theory, simulation, and experiment produces new physics that can be harnessed for transduction and other quantum technologies.

Chapter 5

Microwave to Telecom Wavelength Transduction

This chapter, following a preface describing transduction theory, is based on the experiment presented in the publication [1] "Wavelength transduction from a 3D microwave cavity to telecom using piezoelectric optomechanical crystals," *Appl. Phys. Lett.* **116**, 174005 (2020).

5.1 Piezo-optomechanical Theory

In the previous Chapter, we developed the equations of motion for piezomechanics, which allows an electric field to be coupled to a mechanical resonator by the piezoelectric effect. In Chapter 2, we similarly derived the equations for optomechanical coupling. Here, we combine these formalisms into a complete piezo-optomechanical theory. To begin, the piezo-optomechanical Hamiltonian is

$$\frac{\mathcal{H}}{\hbar} = \omega_c \hat{a}^\dagger \hat{a} + \omega_m \hat{b}^\dagger \hat{b} + \omega_\mu \hat{c}^\dagger \hat{c} + g_0 \hat{a}^\dagger \hat{a}(\hat{b}^\dagger + \hat{b}) + g_\mu(\hat{c}^\dagger + \hat{c})(\hat{b}^\dagger + \hat{b}), \qquad (5.1)$$

which is the summation of the optomechanical Hamiltonian Eqn. (2.31) and the piezomechanical Hamiltonian Eqn. (4.15), where we do not double-count the mechanical mode term. From the Hamiltonian we derive the respective frequency-space equations of motion for the (linearized) optical, mechanical, and microwave

modes:

$$\delta\hat{a}(\omega) = -\frac{ig_0\bar{\alpha}(\hat{b}^\dagger(\omega) + \hat{b}(\omega)) + \sqrt{\kappa_e}\delta\hat{a}_{in}(\omega)}{\chi_a^{-1}(\omega)}, \tag{5.2}$$

$$\hat{b}(\omega) = -\frac{ig_0\bar{\alpha}(\delta\hat{a}^\dagger(\omega) + \delta\hat{a}(\omega)) + ig_\mu(\hat{c}^\dagger(\omega) + c(\omega)) + \sqrt{\Gamma_m}\hat{b}_{in}(\omega)}{\chi_b^{-1}(\omega)}, \tag{5.3}$$

$$\hat{c}(\omega) = -\frac{ig_\mu(\hat{b}^\dagger(\omega) + \hat{b}(\omega)) + \sqrt{\kappa_{\mu,e}}\hat{c}_{in}(\omega)}{\chi_c^{-1}(\omega)}, \tag{5.4}$$

where we recall the respective inverse susceptibilities:

$$\chi_a^{-1}(\omega) = i(\Delta - \omega) + \frac{\kappa}{2}, \tag{5.5}$$

$$\chi_b^{-1}(\omega) = i(\omega_m - \omega) + \frac{\Gamma_m}{2}, \tag{5.6}$$

$$\chi_c^{-1}(\omega) = i(\omega_\mu - \omega) + \frac{\kappa_\mu}{2}. \tag{5.7}$$

These equations can be condensed into a matrix form that improves approachability when solving the equations of motion[1] [30],

$$
\begin{bmatrix} \delta\hat{a} \\ \hat{b} \\ \hat{c} \end{bmatrix} = \frac{1}{1 + \frac{g_0^2|\bar{\alpha}|^2}{\chi_a^{-1}\chi_b^{-1}} + \frac{g_\mu^2}{\chi_b^{-1}\chi_c^{-1}}}
\begin{bmatrix} 1 + \frac{g_\mu^2}{\chi_b^{-1}\chi_c^{-1}} & \frac{-ig_0\bar{\alpha}}{\chi_a^{-1}} & \frac{-g_0\bar{\alpha}g_\mu}{\chi_a^{-1}\chi_c^{-1}} \\ \frac{-ig_0\bar{\alpha}}{\chi_b^{-1}} & 1 & \frac{-ig_\mu}{\chi_b^{-1}} \\ \frac{-g_0\bar{\alpha}g_\mu}{\chi_a^{-1}\chi_b^{-1}} & \frac{-ig_\mu}{\chi_c^{-1}} & 1 + \frac{g_0^2|\bar{\alpha}|^2}{\chi_a^{-1}\chi_b^{-1}} \end{bmatrix}
\begin{bmatrix} \sqrt{\kappa_e}\chi_a\hat{a}_{in} \\ \sqrt{\Gamma_m}\chi_b\hat{b}_{in} \\ \sqrt{\kappa_{\mu,e}}\chi_c\hat{c}_{in} \end{bmatrix}. \tag{5.8}
$$

The equation of motion matrix, where we have neglected counter rotating terms, forms the basis of the experiment that will be carried out in this Chapter. Most importantly, we use the matrix to calculate the transduction efficiency for a signal at frequency ω_s from microwave to telecom, which is the ratio of transduced light output to light input [30]

$$\eta(\omega_s) = \kappa_e \frac{|\delta\hat{a}(\omega_s)|^2}{|\hat{c}_{in}(\omega_s)|^2} \tag{5.9}$$

$$= \kappa_e\kappa_{\mu,e} \left| \frac{|\bar{\alpha}|g_0g_\mu}{\chi_a^{-1}(\omega_s)\chi_b^{-1}(\omega_s)\chi_c^{-1}(\omega_s) + g_0^2|\bar{\alpha}|^2\chi_c^{-1}(\omega_s) + g_\mu^2\chi_a^{-1}(\omega_s)} \right|^2. \tag{5.10}$$

In the wavelength transduction literature, this equation is frequently simplified significantly by choosing $\omega_s = \omega_m = \omega_\mu = \Delta$ and rewriting in terms of cooperativities [23, 30, 97]

$$\eta(\omega_s)_{\Delta=\omega_m} = \frac{\kappa_e\kappa_{\mu,e}}{\kappa\kappa_\mu} \frac{4CC_\mu}{(1 + C + C_\mu)^2}. \tag{5.11}$$

---

[1]We have dropped the explicit frequency dependence for this equation due to space constraints.

By making this simplification the transduction efficiency is maximized, as the complex term in each of the inverse susceptibilities Eqns. (5.5-5.7) is set to zero. However, in Eqn. (5.11), the choice of telecom laser detuning $\Delta = \omega_{\mathrm{m}}$ is at odds with the homodyne measurement technique described in Chapter 3, where the detuning is set to $\Delta = 0$ for maximum detection efficiency. Instead, $\Delta = \omega_{\mathrm{m}}$ optimizes the rate at which phonons are removed from the mechanical mode by means of optomechanical damping, which we recall from our discussion on optomechanics theory Eqn. (2.42), and from our attempt to measure the effect in Fig. 3.13. For future transduction experiments at low temperature, investigating detuning (including blue detuning for amplification [31]) will be of critical importance. For the purposes of the room-temperature proof-of-principle experiment, however, we perform transduction experiments at zero detuning. The transduction efficiency in this case is

$$\eta(\omega_{\mathrm{s}})_{\Delta=0} = \frac{\kappa_{\mathrm{e}}\kappa_{\mu,\mathrm{e}}}{\kappa\kappa_{\mu}} \frac{4C_{\mu}C}{(1 + C_{\mu} + C)^2 + (2(1 + C_{\mu})\omega_{\mathrm{m}}/\kappa)^2}. \qquad (5.12)$$

The extra term present in the denominator is a direct result of the non-zero imaginary component in the optical susceptibility Eqn. (5.5). The term is non-negative, and therefore must result in a reduced efficiency in comparison to Eqn. (5.11). It is important to note differences between the signal frequency ω_{s} and the mechanical mode ω_{m} or microwave ω_{μ} frequencies result in similar terms that reduce the transduction efficiency. Thus for piezo-optomechanical transduction it is important to have $\omega_{\mathrm{s}} \approx \omega_{\mathrm{m}} \approx \omega_{\mu}$. For situations where $\omega_{\mathrm{s}} \neq \omega_{\mathrm{m}}$, in Section 5.10 we discuss how a tunable microwave cavity could be used to optimize transduction efficiency.

5.2 Comparison to Electro-optomechanics

The efficiency of microwave-to-telecom transduction, regardless of the optomechanical mode detuning, is primarily predicated on the cooperativities between the mechanical mode and the electromagnetic modes. In our discussion of piezomechanical theory, we noted that as a result of the linear nature of the piezoemchanical interaction, the piezomechanical cooperativity could not be cavity enhanced. In contrast, the quadratic interaction of optomechanics provides cavity enhancement,

which allows for many optomechanical devices to reach the high cooperativity regime $C > 1$ by driving the interaction with pump photons. Our linearized treatment of the optical mode reveals that the only consequences of the quadratic nature of the optomechanical interaction are cavity enhancement and the presence of a detuning term in the susceptibility. The equations of motion for the telecom Eqn. (5.2), and microwave Eqn. (5.4) modes are otherwise treated identically.

The immediate conclusion that can be drawn from this discussion is that electromechanical coupling (which we recall from Chapter 2 to be the quadratic coupling between microwave and mechanical modes) similarly benefits from microwave-photon-number enhanced coupling, and should therefore allow for easier access to high-cooperativity regimes. Moreover, by replacing the microwave frequency ω_μ with a microwave detuning term Δ_μ in Eqn. (5.7), the restriction $\omega_m \approx \omega_\mu$ required to maximize transduction efficiency would become $\omega_m \approx \Delta_\mu$, which is an easier requirement to meet, since it requires changing a microwave drive tone rather than physically shifting a resonance frequency.

The ability to achieve high-efficiency transduction using electromechanical coupling was demonstrated in Ref. [23], where an efficiency $\eta \approx 10\%$ was reported using a Fabry-Perot type optomechanical cavity with an aluminum-coated membrane, which acts simultaneously as a moving mirror and capacitor (the prototypical example of both optomechanical and electromechanical systems). The electromechanical coupling rate in this case was bolstered by a microwave photon population of $10^7 \sim 10^9$. Despite the success of high-efficiency microwave-to-telecom transduction, the device was hampered by high phonon populations in the mechanical mode, which added noise to the transduced signal.

Despite the advantages posed by using electromechanical coupling instead of piezomechanical coupling, the majority of microwave-to-telecom transduction experiments forgo the benefits of microwave cavity enhancement and detuning-based microwave coupling. This is because a low thermal phonon population is difficult to achieve without high-frequency mechanical modes, and the same high-frequency modes are difficult to electromechanically couple to using microwave cavities. In part, this coupling difficulty is caused by the high spring constant $k = \omega_m^2 m_{eff}$ that directly results from the high frequency, which makes it difficult for the relatively

weak radiation pressure forces to drive mechanical motion [98]. This difficulty could be overcome with a strong enough microwave pump, but the development of superconducting circuits capable of coupling to the mechanical mode while also handling the required microwave power would likely be a feat of engineering. To couple to, for example, the optomechanical crystal breathing mode, metallic capacitors would likely need to be attached directly to the optomechanical crystal near the crystal defect. The proximity of a metal layer to the optical mode would result in increased optical and microwave mode damping from optical absorption in the metal.

The ability to control coupling strength through the number of microwave pump photons makes the development of an electromechanically coupled device an interesting avenue of future exploration. In particular, it may be worth considering both the linear piezomechanical and the quadratic electromechanical interactions through a microwave photoelastic effect simultaneously [95]. This may not result in greatly improved transduction efficiencies, but the interaction between various modes of coupling could result in greater tunability and other interesting quantum effects.

We now return to piezo-optomechanical systems, which despite lacking cavity enhancement, have become very robust in their own right. Numerous systems have used the piezoelectric effect in optomechanical systems to demonstrate microwave-to-telecom transduction, where the microwave to mechanical interaction is mediated through surface acoustic waves [27–31], which are used to directly drive the mechanical mode. In the remainder of this Chapter, we describe the experiment performed in Ref. [1], where we coupled the mechanical breathing mode of our gallium arsenide optomechanical crystal directly to the electric field of a microwave mode within a 3D microwave cavity to demonstrate microwave-to-telecom transduction.

5.3   Telecom Optics, Mechanics, and Microwaves

The optomechanical crystal, characterized in Chapter 3, supports a telecom optical mode at 1543 nm ($\omega_c/2\pi \approx 194.3$ THz), with a total decay rate
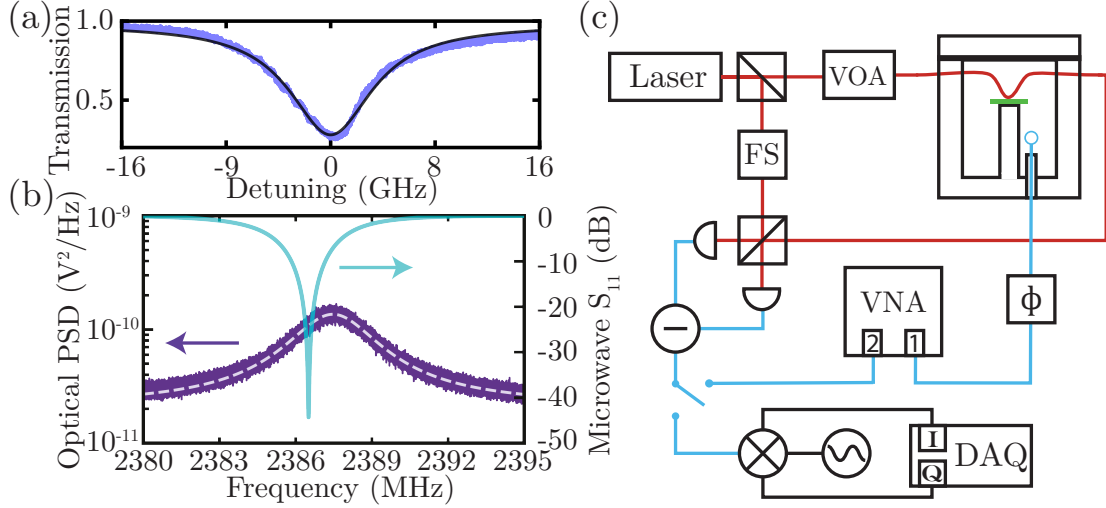
Figure 5.1: (a) Transmission of the telecom resonance (blue), centered at 1543 nm, with fit in black using Eqn. (3.4). (b) Purple trace (left axis): power spectral density (PSD) of the thermomechanical motion, measured by homodyne detection of the telecom mode and fit in dashed white using Eqn. (3.28). Light blue trace (right axis): microwave reflection measurement of the 3D cavity. (c) Measurement setup: the microwave system in blue shows port 1 of a vector network analyser (VNA) driving the microwave cavity using a loop coupler [99], which couples to the magnetic field that circulates the microwave cavity pedestal. The VNA signal phase is controlled externally using a phase modulator (ϕ). The balanced laser homodyne system in red follows two paths: the measurement arm, with telecom optical power set by a variable optical attenuator (VOA) before coupling to the optomechanical crystal (green) in the microwave cavity, and the local oscillator, with a fiber stretcher (FS) for path-length matching and optical phase control. The paths recombine at a beam splitter and are then detected on a balanced photodiode. The photodiode output can either be measured on VNA port 2 or downmixed into low frequency in-phase and quadrature components measured on a separate data acquisition (DAQ) system.

$\kappa/2\pi \approx 6.6$ GHz and external decay rate $\kappa_e/2\pi \approx 2.3$ GHz, which are extracted from the fit of the laser sweep depicted in Fig. 5.1(a). The telecom mode spatially overlaps the high-frequency mechanical breathing mode, which has a frequency $\omega_m/2\pi \approx 2387.5$ MHz and damping rate $\Gamma_m/2\pi \approx 2.90$ MHz, Fig. 5.1(b). Figure 5.1(c) shows a simplified diagram of the homodyne setup used to measure the system, which now includes a vector network analyser[2] VNA used to probe the microwave cavity.

---

[2]Keysight E5063A ENA series network analyser
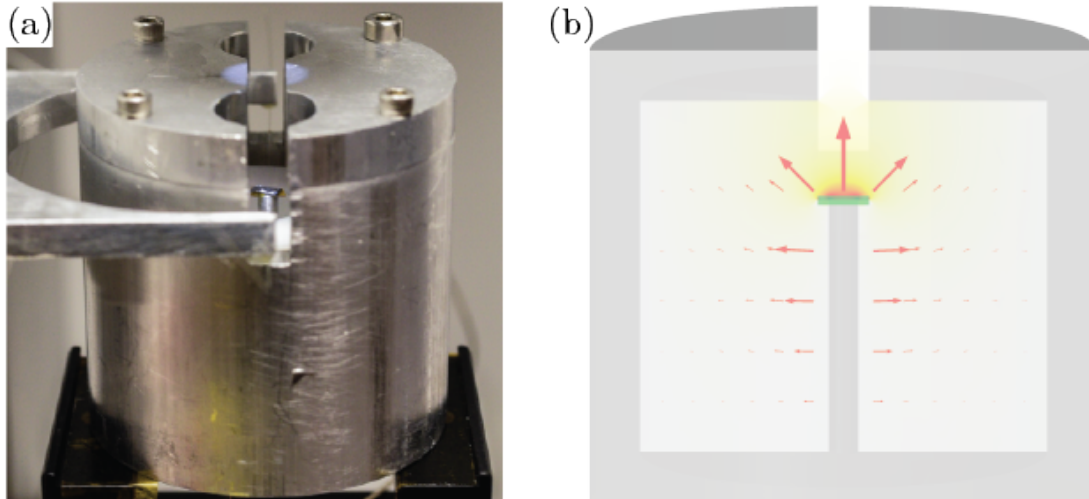
Figure 5.2: (a) Photograph of a split-lid re-entrant 3D microwave cavity, with the gallium arsenide optomechanical crystals placed on the re-entrant pedestal. The dimpled-tapered fiber has been lowered into the microwave cavity to optically couple to an optomechanical crystal. (b) Simulation of the electric field in the 3D microwave cavity mode with arrows showing electric field directivity and relative amplitude.

As shown in Chapter 4, coupling between the mechanical breathing mode and an electric field is best achieved using a primarily z-oriented electric field. This is challenging to achieve for devices using a dimpled-tapered fiber coupling mechanism, which requires z-axis line-of-sight to couple the fiber to the device, thereby preventing the placement of a capacitor directly above the device. To circumvent this issue, we developed an aluminum split-lid re-entrant 3D microwave cavity, pictured in Fig. 5.2(a), which has an inner diameter of 41 mm and an interior height of 35 mm. The re-entrant pedestal measures 2.8 mm in diameter and stands 25 mm tall, which leaves a 10 mm gap between the cavity lid and the top of the re-entrant pedestal where the optomechanical crystal is placed. The cavity lid is split a by 5 mm gap which allows a dimpled tapered fiber [45] to access the gallium arsenide chip for optical coupling. This process takes place in two stages due to limited stage range; first, the optical fiber is lowered using a micrometer stage[3] until it is within ≈ 1 cm of the device chip, then the entire microwave cavity is raised

[3]Newport 9063-XYZ 25.4 mm travel gothic arch linear stage

using a second stage[4] to meet the optical fiber. This greatly increases coupling accuracy, as moving the fiber stage causes vibrations in the fiber.[5]

The microwave mode electric field, shown using arrow vectors in the electric field simulation Fig. 5.2(b), is predominantly directed along the cylinder axis, which corresponds to the [001] crystal axis of the gallium arsenide chip. This design results in a microwave resonant frequency near the mechanical mode frequency. A low-loss Teflon cylinder [95] surrounding the re-entrant pedestal allows for control over the microwave cavity decay rates by shaping the magnetic field, and further allows us to change the microwave mode frequency by approximately 10 MHz. Rotating the loop coupler allows further control over the external decay rate by changing the magnetic flux that passes through the loop. If the area of the loop is perpendicular to the cavity radius, coupling is maximized. Conversely, if the loop is parallel to the radius, the coupling demonstrably goes to zero. Using this control over the microwave resonance, we are able to coarsely tune the microwave mode close to our desired frequency $\omega_\mu = \omega_m$, such that $\omega_\mu/2\pi \approx 2386.5$ MHz. Similarly, we tune the microwave decay rates such that the total cavity decay rate $\kappa_\mu/2\pi \approx 4.07$ MHz is almost exactly double the external decay rate $\kappa_{\mu,e}/2\pi \approx 2.05$ MHz. This condition, known as critical coupling, ensures that on-resonance there is near-zero (-45 dB) reflection of microwave power from the cavity [33].

5.3.1 Piezomechanical coupling

As discussed in Chapter 4, coupling between the microwave electric field and the mechanical motion of the optomechanical crystal is mediated by the d_{36} coefficient of the piezoelectric tensor, which converts a transverse electric field oriented along the [100] crystal axis into shear motion in the plane of the optomechanical crystal [100]. In Fig. 4.5, the displacement of the optomechanical crystal due to a resonant transverse electric field was simulated to demonstrate the similarity between the mechanical breathing mode and microwave driven motion. The spatial overlap

---

[4]Thorlabs NanoMax302 3-axis stage with open-loop piezos

[5]Application note: The thorlabs stage piezo motors drift over time unless they are locked using the Thorlabs BPC303 piezo controller. Leaving the stage circuits open will cause drift. 50-Ohm terminating the stage circuits will cause drift. Connecting the stage circuits to the controller but not actively feeding back will cause drift.

between the mechanical mode and driven motion indicates that the piezoelectric interaction between the microwave transverse electric field and the mechanical breathing mode should result in well-coupled modes. Although the microwave cavity electric field is predominantly transverse, small in-plane electric field components caused by imperfect electric field directivity are capable of driving high-order flexural and torsional modes in the optomechanical crystal, however these modes have poor overlap with the optical mode and are therefore not measured.

Despite our best efforts to tune the microwave cavity frequency using the teflon core, we find that the microwave mode is slightly detuned from the mechanical resonance such that $(\omega_\mu - \omega_m)/2\pi \approx 1$ MHz. Despite this small offset, Fig. 5.1(b) shows that the microwave mode frequency lies within the linewidth of the mechanical mode and vice versa, implying that a signal can be resonantly coupled to both the microwave and mechanical modes.

5.4 Transduced Signal

In Fig. 5.3(a), the mechanical motion of the optomechanical crystal is measured while the microwave cavity is driven by a -20 dBm electrical signal at frequency ω_s, which is set to the microwave resonance frequency. The electrical signal populates the microwave mode with photons, which are converted into actuated phonons in the mechanical mode through the piezoelectric effect. The telecom laser, at frequency ω_ℓ, causes the actuated phonons to be up-converted into telecom photons at frequency $\omega_\ell + \omega_s$. The up-converted photons beat together with a local oscillator to produce a sharp peak in the homodyne measurement—the transduced microwave tone.

5.5 Phase Coherence

Coherent transduction is then demonstrated by using an external phase modulator[6] to sweep the phase of the injected microwave signal, plotted in Fig. 5.3(b), from $0°$ to $144°$. The output of the balanced photodiode is returned to the second port of the VNA for an S_{21} measurement, where the returned signal

---

[6]Pasternack PE8255 adjustable phase shifter
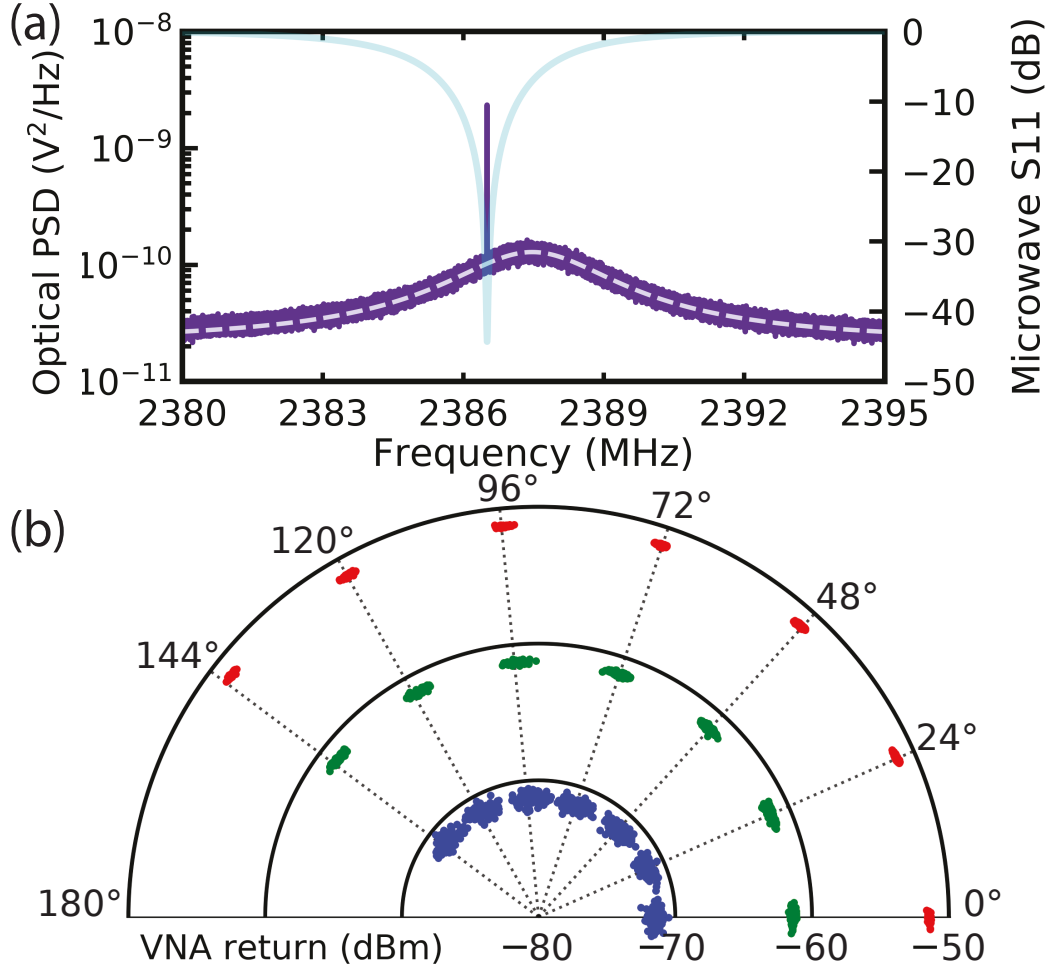
Figure 5.3: (a) Microwave-to-telecom transduction. A 10 µW electrical signal at the microwave resonance frequency creates a sharp peak in the optical PSD. (b) Phase coherence measurements of the transduced signal. The input signal phase (dotted lines) is swept in 24° steps using the external phase modulator, for three sets of microwave input power: 200 µW (red), 20 µW (green), and 2 µW (blue). Slight systematic offset at high phase angles may be due to miscalibration of the microwave phase shifter.

mixes with the VNA output signal to determine relative phase. By manipulating both the phase and amplitude, we show that we have complete coherent control of the transduced signal [27]. Classically, coherent control implies that the system can be used for information transduction techniques such as phase shift keying [48].

Although the data shown in Fig. 5.3(b) was taken with the VNA, the original intent was to use the low-IF receiver detailed in Chapter 3 to measure the signal phase. This allow for the signal phase to be both set and detected in a fully

automated measurement system, capable of encoding detailed information in the microwave signal and upconverting it into an optical signal. At the time of the experiment, the low-IF receiver was limited by the clock rate, which created significant ($\approx 5°$) phase errors at the step where the measured signal was digitally downmixed. The lab now has a 4-channel high-speed DAQ card[7] which will allow the clock to be captured at the same rate as the signal. This should eliminate phase errors and allow for extremely high-precision automatic phase and amplitude measurements.

5.6 Piezomechanical Coupling Calibration

The number of actuated phonons $\bar{n}_\mathrm{s}$ in the mechanical breathing mode can be calculated using thermomechanical noise as a calibration metric [27]. The ratio of the powers in the transduced peak $\mathcal{P}(\omega_\mathrm{s})$ and the thermal noise $\mathcal{P}(\omega_\mathrm{m})$, where power is the integrated spectral density, is scaled by the number of thermal phonons such that

$$\bar{n}_\mathrm{s} = \frac{\hbar\omega_\mathrm{m}}{k_B T}\frac{\mathcal{P}(\omega_\mathrm{s})}{\mathcal{P}(\omega_\mathrm{m})}, \tag{5.13}$$

where $T = 295$ K is room temperature. To ensure the device is properly thermalized and optical heating is appropriately limited, the thermal noise is in turn calibrated to a temperature-independent electro-optic modulator tone in the signal arm [79]. This calibration process is exactly the phase calibration used to calculate the optomechanical coupling in Chapter 3, but instead the ratios are used to calculate the temperature T. In Fig. 5.4, the number of actuated phonons are calculated for a range of microwave powers. At low powers, the transduced signal sinks below the thermal noise floor at an average population of $(9.0 \pm 0.4) \times 10^{-2}$ actuated phonons. Sufficiently far from this thermal limit, the number of actuated phonons increases linearly with microwave input power. This slope is fit to Eqn. (4.25) to calculate the single-photon piezomechanical coupling rate $g_\mathrm{\mu}/2\pi = (4.3 \pm 0.8)$ Hz. Using the piezomechanical coupling rate we can additionally calculate the piezomechanical

---

[7]Ultraview AD16-250X4 high-speed analog-to-digital converter
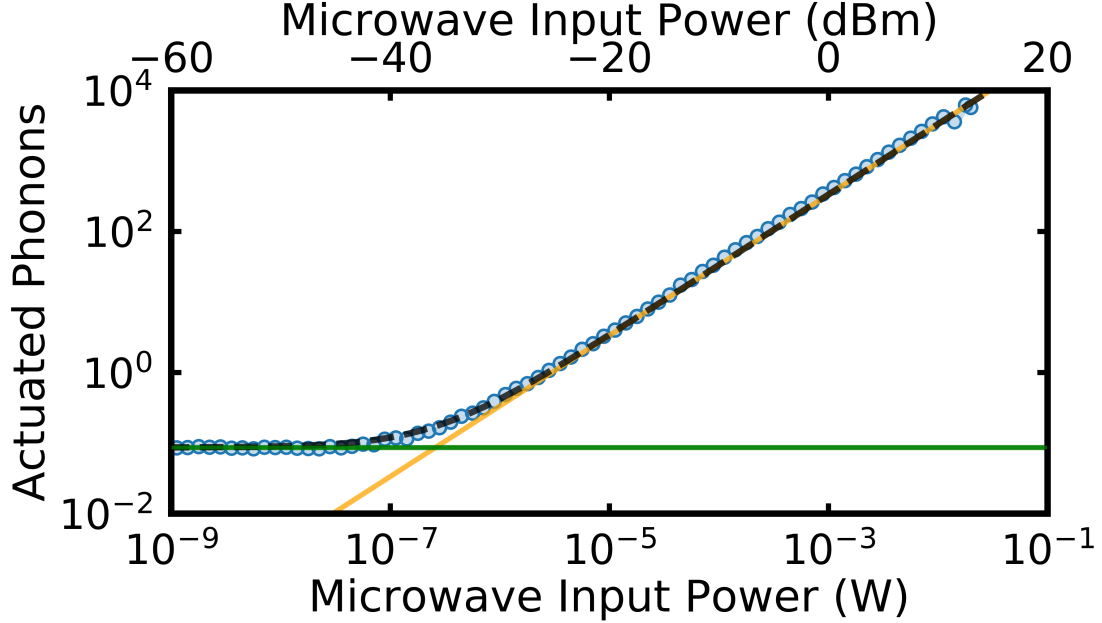
Figure 5.4: The integrated area of the transduced peak, scaled using Eqn. (5.13) to measure the actuated phonon number, measured as microwave power is stepped. The resulting trace is fit in two segments: input power above 10^{-5} W is fit to a line (orange) to determine the piezomechanical coupling, and input power below 10^{-8} W is fit to a constant to determine the measurement noise floor, below which the transduced signal becomes unmeasurable due to thermal noise. The sum of these fits is presented as the black dashed curve. Error in the actuated phonon number is smaller than the marker size. The uncertainties of derived quantities are calculated from 1σ fit error.

cooperativity,

$$C_\mu = \frac{4g_\mu^2}{\kappa_\mu \Gamma_m} \tag{5.14}$$

$$= (6.2 \pm 0.2) \times 10^{-12}. \tag{5.15}$$

5.7 Transduction Efficiency

We have now fully characterized the fundamental parameters of the piezo-optomechanical system, which are summarized in Table 5.1.

Using the calculated optomechanical and piezomechanical cooperativities, we first consider the single-photon efficiency, in which the optomechanical interaction is not parametrically enhanced by a steady-state photon population. In this

	Optics (GHz)	Mechanics (MHz)	Microwaves (MHz)
Wavelength	$\lambda_\text{c} \approx 1543$ nm	—	—
Frequency	$\omega_\text{c}/2\pi \approx 194300$	$\omega_\text{m}/2\pi \approx 2387.5$	$\omega_\mu/2\pi \approx 2386.5$
Tot. decay rate	$\kappa/2\pi \approx 6.6$	$\Gamma_\text{m}/2\pi \approx 2.9$	$\kappa_\mu/2\pi \approx 4.07$
Ext. decay rate	$\kappa_\text{e}/2\pi \approx 2.3$	—	$\kappa_{\mu,\text{e}}/2\pi \approx 2.05$
Mode coupling	$g_0/2\pi = (1.3 \pm 0.3)$ MHz		$g_\mu/2\pi = (4.3 \pm 0.8)$ Hz
Cooperativity	$C = \bar{n}_\text{cav}(3.5 \pm 0.1) \times 10^{-4}$		$C_\mu = (6.2 \pm 0.2) \times 10^{-12}$

Table 5.1: Summary of room temperature piezo-optomechanical properties of the gallium arsenide optomechanical crystal used for microwave to telecom transduction.

case, with $\bar{n}_\text{cav} = 1$, the efficiency is calculated using Eqn. (5.12) to find $\eta_{\Delta=0} = \bar{n}_\text{cav}(1.0 \pm 0.1) \times 10^{-15}$.

For high-efficiency transduction, the condition $C \approx C_\mu \gg 1$ must be achieved. In the present experiment, the telecom photon population of the optomechanical crystal was limited to $\bar{n}_\text{c} \approx 400$ to circumvent optical heating, leading to a cooperativity $C = 0.14$. The cavity-enhanced transduction efficiency can be recalculated to find $\eta_{\Delta=0} = (3.4 \pm 0.2) \times 10^{-13}$. The transduction efficiency recorded in this experiment is far from being efficient, but does provide a starting point for future systems to improve on.

5.8 Future Transduction Prospects

Even with the enhancements to optomechanical cooperativity, the efficiency of our system is primarily limited by piezomechanical cooperativity, which is in turn limited by the piezomechanical coupling rate. Our ability to transduce microwave tones to optical frequencies is fuelled by high populations of photons in the microwave cavity, which allows us to overcome the poor coupling and efficiency. As a result, without improvements to the piezomechanical coupling rate the experiment will be unable to progress to the next set of microwave-to-telecom transduction milestones, which include bidirectional transduction and the transduction of quantum signals.

As a part of our experiment, we attempted to reverse the microwave-to-telecom transduction process and measure a telecom signal using the microwave mode.

This was approached in two ways, first, we considered an optical pump-probe scenario, where the optical cavity is driven strongly on the red sideband and a small transduction signal is injected at the optical resonance frequency. In a classical sense this can be understood as creating an optical field in the cavity that beats at the mechanical frequency and therefore drives the mechanical mode through radiation pressure forces. We further attempted to drive the mechanical mode using the blue-detuned sideband, where stokes scattering causes the laser photons to be preferentially converted into a photon-phonon pair that is resonant with the optical and mechanical modes respectively. In both cases, poor piezomechanical coupling prevented the detection of telecom-to-microwave transduction. In future experiments where coupling is improved, these trials should be repeated to demonstrate bidirectional conversion.

Fortunately, the path to increased piezomechanical coupling, and moreover increased piezomechanical cooperativity, is relatively straightforward because the piezomechanical coupling is predicated on the overlap of the optomechanical crystal and the microwave electric field [74]. In our system, this overlap is small due to the large spatial requirement of the dimpled tapered fiber optical coupling mechanism. Future iterations with permanent fiber coupling [101] will allow the gap between the cavity pedestal and lid to be dramatically decreased, thus increasing field overlap and allowing piezomechanical coupling to reach rates on the order of 1 kHz. Additionally, the piezomechanical cooperativity can be further increased by reducing the microwave cavity decay rate and mechanical damping rate. Specifically, 3D superconducting microwave cavities are capable of decay rates below $\kappa_\mu/2\pi = 100$ Hz [102], and low temperature measurements in Chapter 6 will demonstrate an improved mechanical damping rate of $\Gamma_m/2\pi = 83$ kHz. With these improvements taken into account the piezomechanical cooperativity could reach values exceeding 1, which would lead to nearly lossless microwave-to-telecom transduction, bidirectional transduction of signals, and quantum state transduction.
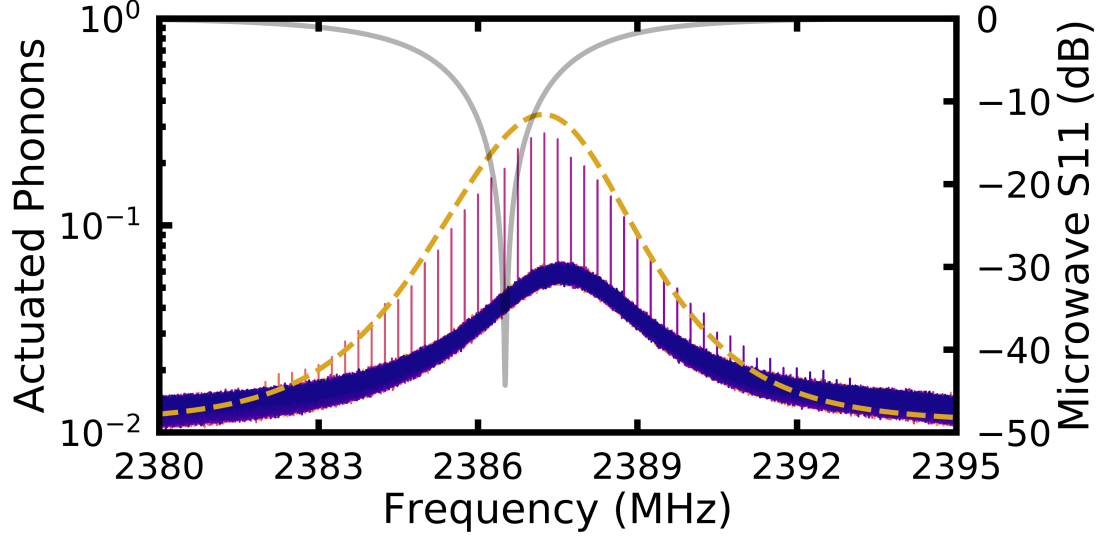
Figure 5.5: Optical measurements of the transduced 3.2 µW electrical signal as it is swept between 2380 MHz to 2395 MHz in 0.25 MHz steps. The dashed curve represents a calculation of the number of actuated phonons for the whole frequency range, using Eqn. (4.24) with experimentally measured parameters.

5.9 Frequency Dependence

Another important metric for microwave-to-telecom transduction is the bandwidth over which efficient transduction can be achieved. A large bandwidth increases the utility of the transducer by allowing it to convert a range of microwave frequencies to telecom wavelengths and permits faster transduction operations [11]. To measure the bandwidth of transduction, the electrical signal frequency is stepped across the the mechanical and microwave resonances and the mechanical spectrum is measured by optical homodyne at each step. In Fig. 5.5 the mechanical spectrum is scaled using Eqn. (5.13), such that the amplitude of each transduced peak represents the number of actuated phonons in the mechanical mode. This demonstrates that the maximum number of actuated phonons is achieved for a frequency between the microwave and mechanical peaks at $\omega_{\max}/2\pi = 2387.25$ MHz.

To confirm the accuracy of the measured spectrum, Eqn. (4.24) is used to calculate the number of microwave actuated phonons for an arbitrary microwave signal of frequency ω_s and power P_s. In Fig. 5.5, the number of actuated phonons $\bar{n}_s(\omega_s)$ is plotted across the same region over which the electrical signal is measured to demonstrate the agreement between experiment and theory. From Eqn. (4.24),

a microwave-to-mechanics transduction bandwidth of $2\pi \times 2.16$ MHz is calculated, which exceeds the predicted bandwidth of similar piezoelectric microwave cavity to telecom transducers [103]. The large bandwidth is in part due to an efficiency-bandwidth trade-off for transduction: the high decay rate of the microwave cavity and damping rate of the mechanics increases bandwidth, but in turn limits the number of actuated phonons and therefore the efficiency of the transducer. During low-temperature experiments both the damping and decay rates will be reduced, which limit the bandwidth of future experiments, but increase transduction efficiency.

5.10   Tunable Microwave Cavities

In Fig. 5.6, the transduction efficiency is plotted as a function of signal frequency for our experiment where $\omega_{\mathrm{m}} - \omega_{\mu} \approx 1$ MHz and for the ideal transduction scenario $\omega_{\mathrm{m}} = \omega_{\mu}$. Encompassing both the experimental and ideal transduction scenarios is a calculation of efficiency which assumes a tunable 3D microwave cavity [104] with a resonance frequency set such that the input electrical signal is transduced with maximum efficiency at each considered frequency. In ideal circumstances, where the electrical signal frequency matches the mechanical resonance frequency, the efficiency of transduction is unchanged. For unmatched resonances however, the microwave cavity can be tuned to increase the transduction efficiency.

The extended range afforded by a tunable cavity has a full-width half-max of 2.91 MHz, such that the transduction efficiency of off-resonant signals improves by up to an order of magnitude. Though this is not a true increase in bandwidth, which refers to the maximum frequency spread that can be simultaneously passed by the cavity, it does increase the frequency range over which the transducer can function. For the microwave cavity under consideration in this experiment, the increased transduction range associated with a tunable microwave cavity is modest, but becomes more pronounced when the reduced decay rates of superconducting cavities are taken into account [102].
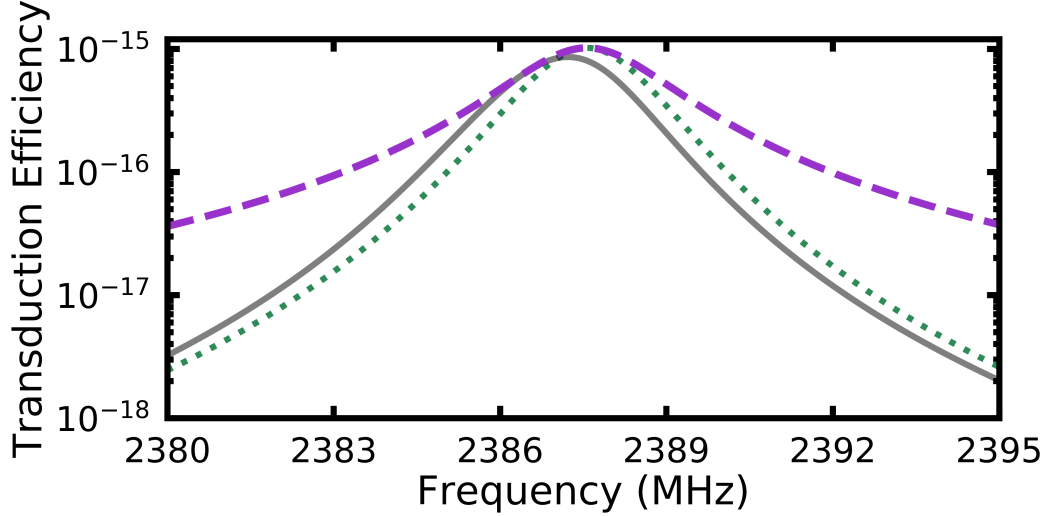
Figure 5.6: Calculations of the conversion efficiency for the transduction of electrical input signals at various frequencies ω_s using the experimental parameters outlined for this experiment (grey solid), the ideal scenario where the detuning between microwave and mechanical resonances is zero (green dotted), and the maximum transduction efficiency attained by using a tunable microwave cavity to select the microwave resonance frequency for maximum transduction efficiency at each input signal frequency (purple dashed).

5.11   Noise in Transduction Experiments

The use of homodyne or direct detection measurements requires a careful approach to noise. Since there is no optical downmixing involved, the photodetector measures a signal frequency at ω_s, which implies that the photodetector itself, any SMA cables, filters, and amplifiers prior to electronic downmixing are susceptible to noise at the signal frequency. In Fig. 5.7, we demonstrate a bandwidth sweep that was taken prior to protecting the system from noise. The transduced peaks in this case appear to be suppressed in the region of the microwave resonance. In contrast, the mechanical resonance and calibration tone appear properly in the measured power spectral density, which suggests that the optical measurement was performed correctly.

The noise peaks evident in Fig. 5.7 were confirmed to be noise by subsequently turning off the laser and repeating the measurement. In this case, the thermal noise and calibration tone were not measured, but the microwave peaks were still visible. Additionally, the noise peaks were responsive to changing the microwave input power,
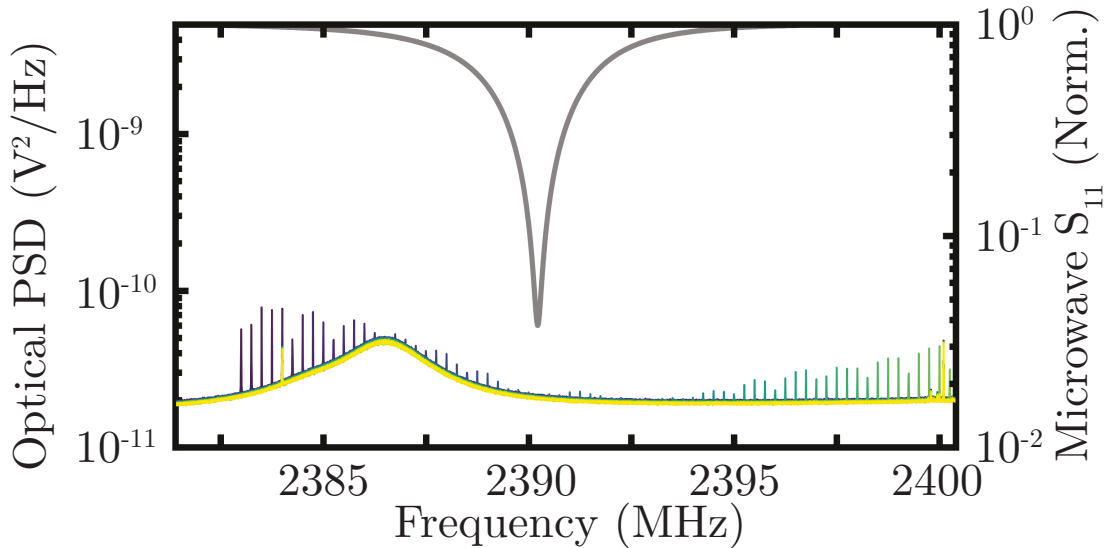
Figure 5.7: Transduction measurement demonstrating system noise. Each colour is represents a measurement of the optical power spectral density, between which the microwave input frequency was stepped by 0.25 MHz. Thermal noise and a calibration tone ($\omega_{\mathrm{CAL}}/2\pi = 2384$ MHz) appear as expected in every trace. The transduction peaks however appear to be suppressed instead of amplified by the microwave resonance (grey), which is slightly more offset from the mechanical mode. Past 2400 MHz, there is additional noise that appears in every trace. This noise is thought to originate from Wi-Fi broadcasts.

with the same scaling as shown in Fig. 5.4. This implied that somewhere between the VNA and the microwave cavity the microwave tone was being broadcast, and somewhere between the photodetector and the electronic downmixer the microwave tone was being picked up, thereby completely skipping the microwave to telecom conversion process while mimicking the transduced signal.

Isolating the microwave cavity using a Faraday cage was considered as a possibility for eliminating the noise, but the complexity of building a radiation-tight enclosure around the experiment, and the possibility of isolating the system from Wi-Fi noise, made isolating the detection equipment using grounded metal enclosures a more appealing path to noise isolation. The grounded metal enclosures were successful in reducing both Wi-Fi and microwave broadcast noise, but failed to completely eliminate it. To ensure the noise was completely eliminated, the power sweep measurements in Fig. 5.4 and frequency sweep measurements in Fig. 5.5 were taken with the detection apparatus in a separate room from the microwave

cavity, connected using only a fiber-optic link that is immune to the radio frequency broadcast noise.

5.12   Experiment Summary

In conclusion, we have demonstrated gallium arsenide optomechanical crystals in a 3D microwave cavity as a promising platform for quantum state transduction. The optomechanical crystal is sensitive enough to detect an average occupancy of just $(9.0 \pm 0.4) \times 10^{-2}$ actuated phonons, and is capable of achieving high cooperativity. The piezoelectric coupling $g_\mu/2\pi = (4.3 \pm 0.8)$ Hz between the microwave and mechanical modes limits the transduction efficiency to $\eta_0 = (1.0 \pm 0.1) \times 10^{-15}$, but could be improved by reducing the microwave electric field mode volume. Finally, the 2.16 MHz transduction bandwidth of this system allows for a broad range of electrical signals to be transduced. Although this bandwidth will be reduced when the transduction experiment is performed at low temperatures, where the microwave cavity will be superconducting, we have proposed a framework using a tunable microwave cavity to allow for microwave-to-telecom transduction that is efficient, low-loss, broadband, and coherent.

Chapter 6

Ground State Mechanics

This chapter expands on the publication [2] "Elimination of thermomechanical noise in piezoelectric optomechanical crystals," *Phys. Rev. Lett.* **123**, 093603 (2018). The low-temperature experiments described here took place prior to the transduction experiment, which limited our ability to predict the operation of a complete transducer at low temperatures. Here, we update these results based on the results of the room-temperature transduction experiment, and predict the results of a final low-temperature microwave to telecom transduction experiment.

6.1 Thermal noise

In the previous chapter, we transduced a microwave signal into a telecom signal and calibrated the transduction efficiency by comparing the number of actuated microwave phonons to the room temperature population of thermal phonons in the device. This procedure highlighted thermal noise as a resource that could be used to calibrate the transduced signal, but it was clear that below a certain signal strength the thermal noise completely washed out the transduced signal. When further considering the application goal of transducing quantum states, the thermal noise presents even larger problems, as thermal phonons at the signal frequency will be indistinguishable from the desired quantum state once they are transduced to optical photons. For this reason, the thermal noise in the mechanical mode must be reduced such that the average phonon population is less than one. This limits both the chance of transducing thermal phonons, and also the decoherence rate $\Gamma_{\mathrm{m}} \bar{n}_{\mathrm{th}}$ of quantum states stored in the mechanical mode.

In this chapter, we eliminate thermomechanical noise in the gigahertz-frequency mechanical breathing mode of a piezoelectric optomechanical crystal using cryogenic cooling in a dilution refrigerator. We measure an average thermal occupancy of the mechanical mode of only 0.7 ± 0.4 phonons, providing a path towards low-noise microwave-to-optical conversion in the quantum regime. These measurements are bolstered by our measurement of the cooperativity, which we calculate to be $C = 3.7$ using a combination of continuous and pulsed measurements. We begin with a description of the low temperature apparatus and initial low temperature measurements.

6.2 Low Temperature Apparatus

Low-temperature experiments on the gallium arsenide optomechanical crystals are performed on the baseplate of an Oxford dilution refrigerator, photographed in Fig. 6.1(a), which is capable of reaching temperatures below 15 mK. The baseplate is configured to allow for flexible optical coupling while simultaneously maximizing the thermal connection between the dilution refrigerator and the device. It achieves this using braided copper cable to connect a set of positioning stages,[1] which allow the devices to be positioned in a three-dimensional space, to the mixing chamber which provides cooling power. Optical coupling to the devices is achieved using a fourth positioning stage, which allows the fiber to be moved from side to side such that the fiber dimple is in view of the endoscope optical imaging system [77]. The endoscope allows for optical access within the fridge for the purposes of positioning the device, without creating a significant source of room temperature radiation heat. An image Fig. 6.1(b) taken using the endoscope shows an optomechanical crystal coupled to the dimpled tapered fiber.

A closeup of the chip holder, Fig. 6.1(c), shows the gallium arsenide chip mounted at a 22.5° angle to allow for off-axis coupling between the fiber and the device. The gallium arsenide chip is mounted alongside a diamond chip that hosts optomechanical microdisks, which were investigated as part of a side-project. The chip holder itself is made from copper which has been annealed and gold plated to

---

[1]Attocube low temperature linear nanopositioners, models LT-UHV ANPx101, ANPz101.

(a) Endoscope

Mixing chamber

Fiber holder

Chip holder

Positioning stages

RuOx thermometer

Copper braids

(b) Optomechanical crystals

Fiber Dimple

(c)
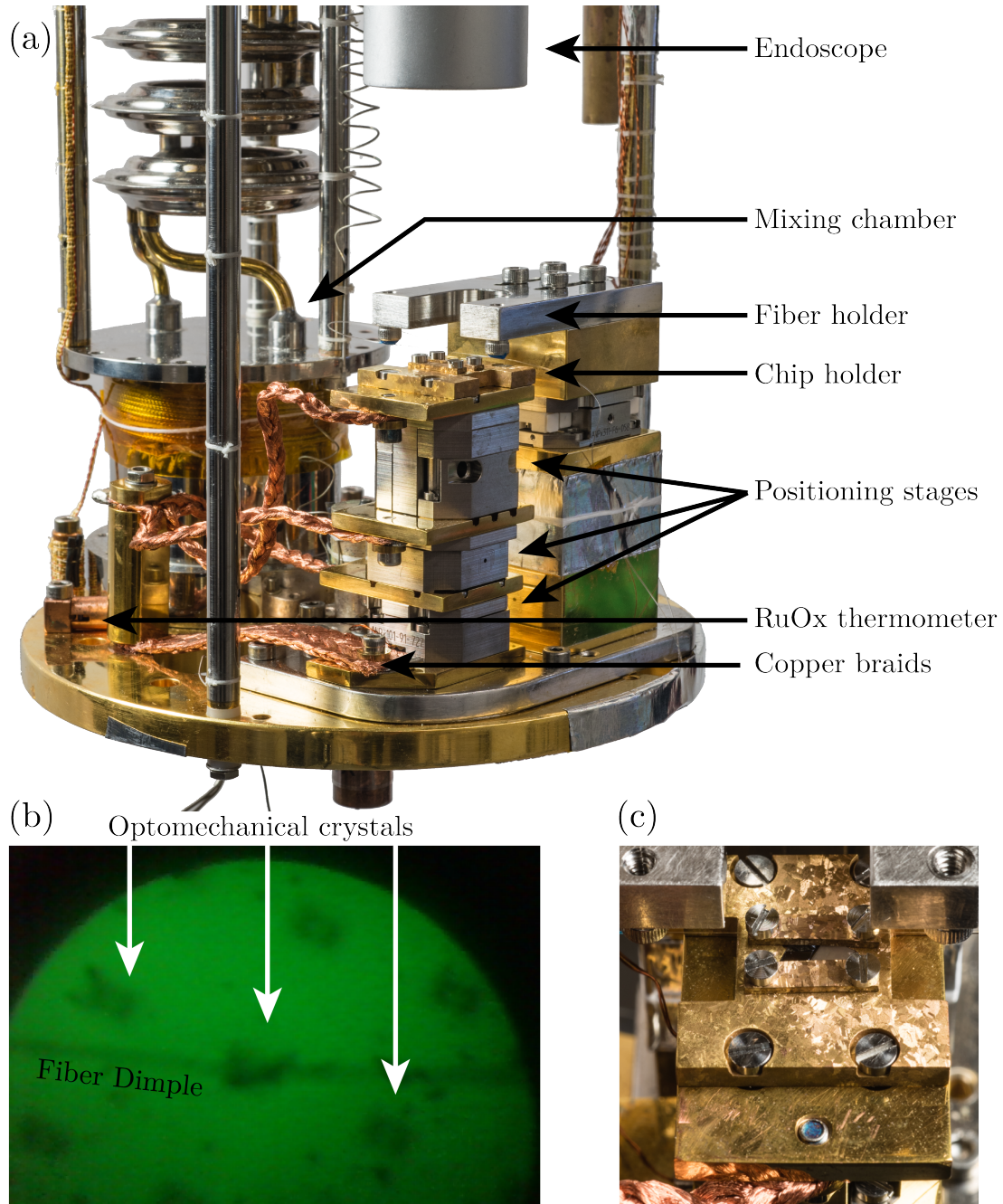
Figure 6.1: (a) Base plate of the dilution refrigerator. Devices are mounted in a chip holder, placed on a stack of piezoelectric positioning stages. Copper braids provide thermal anchoring between the chip holder and the mixing chamber. A high-efficiency dimpled tapered fiber is mounted on a fiber holder next to the positioning stack. The endoscope optical imaging system above the chip holder allows for real-time optical access to the device to facilitate coupling. A ruthenium oxide (RuOx) thermometer measures the temperature of the mixing chamber. (b) Endoscope image of optomechanical crystals while coupled to a dimpled tapered fiber. (c) Close up of holder with GaAs chip (black).

provide a malleable surface. The chip is screwed in tightly enough to deform the surface of the chip holder, which creates a high surface area mechanical connection for thermal conduction at millikelvin temperatures. This mechanical connection is advantageous over other methods of securing the chip, such as silvered epoxy or varnish, both of which are capable of conducting heat at 4 K but become insulators at millikelvin temperatures.

Thermometry is achieved using a ruthenium oxide (RuOx) thermometer which is attached to the base plate of the dilution refrigerator. The RuOx thermometer accurately measures the temperature of the mixing chamber above $T_{\mathrm{MC}} = 20$ mK, and is sensitive to temperature changes, but is not necessarily accurate, for colder temperatures.

6.3   Continuous Measurement

Initial low-temperature experiments were carried out with the intention of replicating the room temperature characterization results. The optical resonance of the optomechanical crystals had no significant changes, with the mode frequency and damping rate remaining near the values measured in Chapter 3. The mechanical resonance, however, changed significantly. Both the mechanical resonance frequency and mechanical damping rate are temperature dependent through the Young's modulus (and thus the elasticity coefficients) of gallium arsenide [105].   As temperature decreases and the gallium arsenide stiffens, resonance frequency increases and the mechanical damping rate decreases.

In Fig. 6.2(a), the mechanical resonance is measured at a series of three different optical powers. At the highest measurement power, the mechanical resonance exhibits a frequency shift to $\omega_{\mathrm{m}}/2\pi \approx 2397.5$ MHz, with a damping rate $\Gamma_{\mathrm{m}}/2\pi \approx 0.5$ MHz extracted from a fit to Eqn. (3.28). In Chapter 3, the power in the mechanical peak was shown to be proportional to both the measurement strength α and the number of thermal phonons through β_{m}, such that

$$\mathcal{P}(\omega_{\mathrm{m}}) = \int_{\omega_{\mathrm{m}}} \left(S_{VV}(\omega) - S_{VV}^{w} \right) d\omega \tag{6.1}$$

$$= \frac{2\alpha g_0^2}{\omega_{\mathrm{m}}^2} \bar{n}_{\mathrm{th}}. \tag{6.2}$$
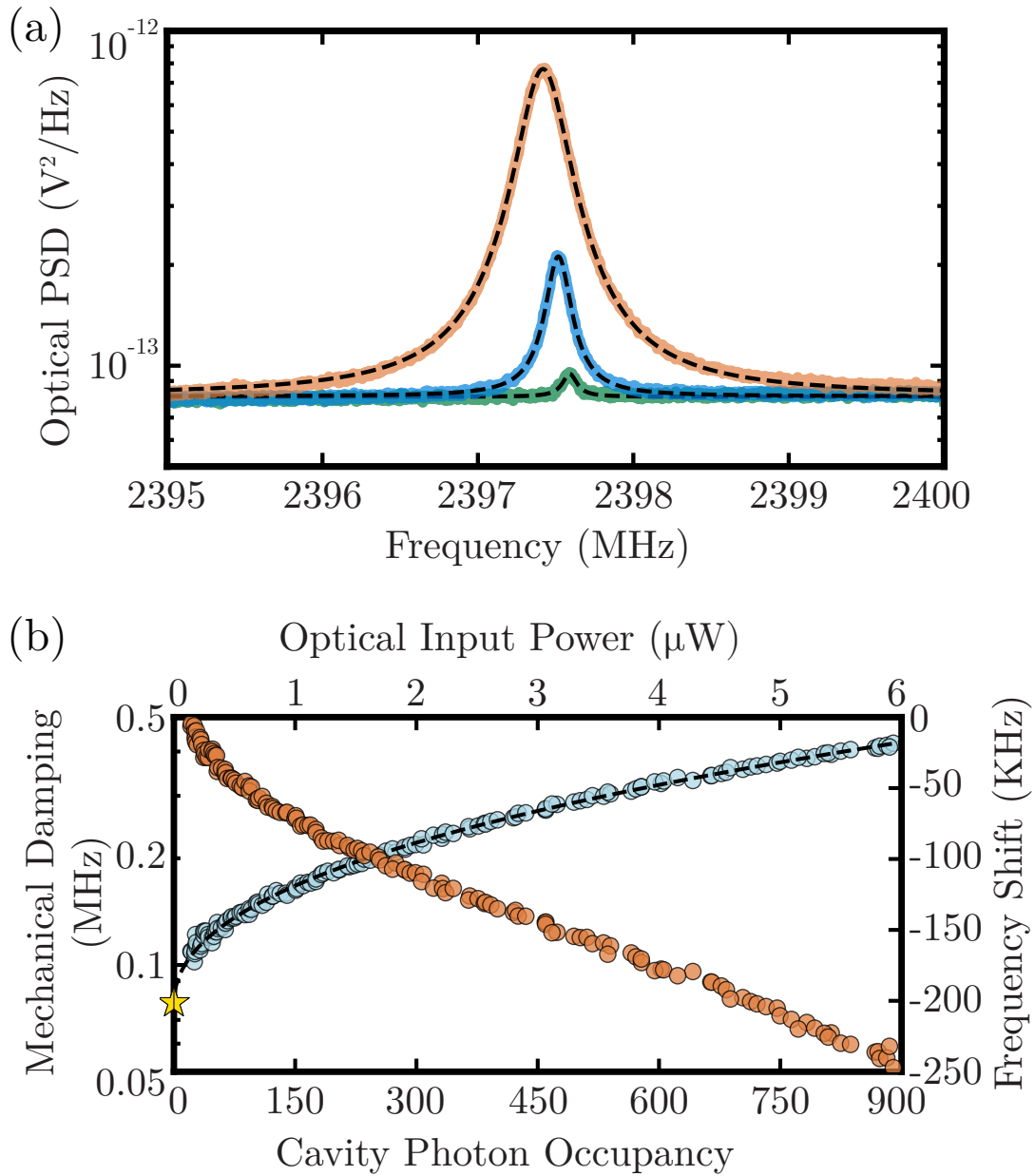
Figure 6.2: (a) Mechanical breathing mode resonance at $T_{mc} \approx 20$ mK, fit and measured with high optical power (orange, 6.43 µW → 938 photons), moderate optical power (blue, 2.25 µW → 336 photons), and low optical power (green, 0.43 µW → 66 photons). (b) Mechanical damping (blue) and frequency shift (orange) as a function of measurement power.

Reducing the cavity photon population results in reduced measurement strength α, which manifests as the smaller mechanical resonances in Fig. 6.2(a). However, the reduced measurement strength does not explain the frequency shift between the three measured peaks. Fitting the peaks, we further observe that the mechanical damping rate changes as a function of optical power. In Fig 6.2(b), we expand on these measurements and plot the mechanical damping rate and shift in mechanical frequency as a function of cavity photon occupancy. Clear trends emerge in both cases, demonstrating that the mechanical mode depends on the population of photons in the cavity. We suspect that this is the result of the absorption of photon in the optical mode causing device heating.

To provide a better understanding of the mechanical damping of the optomechanical crystals at low temperature, the measured damping is heuristically fit to an exponential function

$$\Gamma_{\mathrm{m}}(\bar{n}_{\mathrm{cav}}) = \Gamma_{\mathrm{m}}(0)e^{a\sqrt{\bar{n}_{\mathrm{cav}}}}, \tag{6.3}$$

from which we extract a zero-photon mechanical damping $\Gamma_{\mathrm{m}}(0)/2\pi = 79.9$ kHz (often simply written Γ_{m}), and a scaling factor $a = 5.3 \times 10^{-2}$.

Repeating the experiment at a range of temperatures from 20 mK to 6 K and using the heuristic fit to find the zero-photon mechanical damping rate at each temperature produces Fig. 6.3. The zero-photon damping rates are also fit heuristically to be linearly dependent on the fridge temperature, allowing us to calculate an intrinsic zero-temperature, zero-photon damping rate $\Gamma_{\mathrm{m}}/2\pi = 78.8$ kHz, which increases at a rate 2.5 kHz/K. The scaling factor a was consistent throughout the dataset, however when the experiment was later repeated with slightly different measurement conditions, we found that the scaling factor a had changed. This suggests that the scaling factor is at least partially dependent on measurement conditions and makes it difficult to use it to extract physical parameters.

Further evidence that the mechanical mode is heated by the presence of photons in the optical cavity is attained from a low-temperature phase calibration measurement, Fig. 6.4, wherein the mechanical resonance demonstrably shifts to lower frequencies near the center-frequency of the optical resonance. This can

91
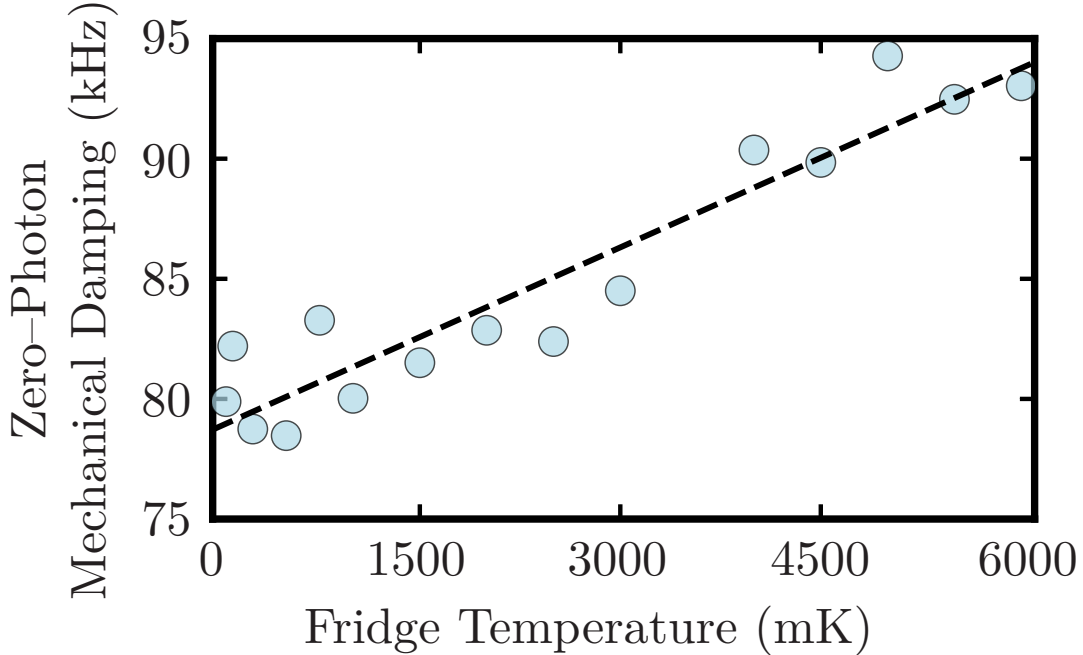
Figure 6.3: Mechanical damping at zero-photon occupancy for a range of Fridge temperatures. A linear fit is used to extract an intrinsic mechanical damping rate $\Gamma_{\mathrm{m}}/2\pi = 78.8$ kHz.

be explained using Eqn. (2.25), where the number of steady state photons $\bar{n}_{\mathrm{cav}}$ is a function of optical resonance detuning, which is maximized on resonance. Repeating the room-temperature phase calibration calculations using the data presented in Fig. 6.4, we calculated the optomechanical coupling using Eqn. (3.42) to be $g_0/2\pi = (1.3 \pm 0.3)$ MHz, where the larger error reflects the effect of the optical heating.

Despite the presence of optical heating acting as a source of error for our measurement of the optomechanical coupling, we use this result to calculate theoretical values for optomechanical effects throughout this thesis. The true value of the optomechanical coupling is likely on the lower end of the error, near $g_0/2\pi = 1.1$ MHz, which is what it is calculated to be near the edge of the optical resonance (see Fig. 6.5). Attempts to repeat this measurement using less optical power were met with poor results as the reduced signal-to-noise ratio resulted in high measurement variance, similar to the outlier points shown at the edges of Fig. 6.5. In future experiments, it may be pragmatic to use homodyne measurements to calculate the optomechanical coupling. The low-power nature of homodyne
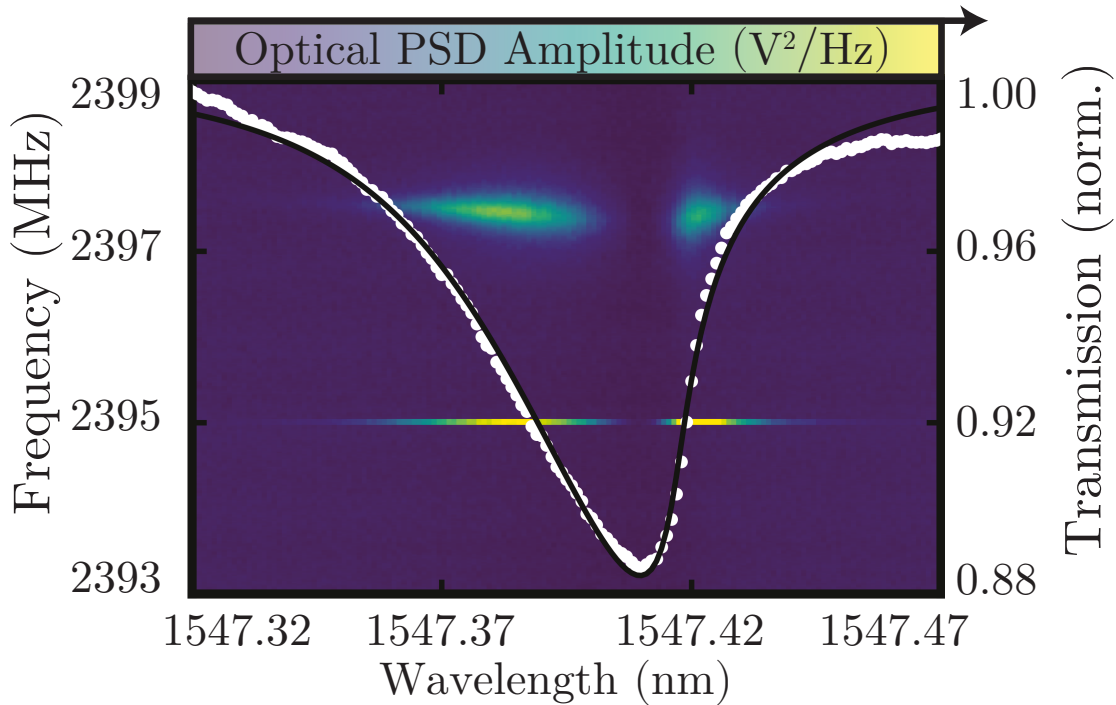
Figure 6.4: Optomechanical coupling measurement at 4 K. DC transmission (white) of the optical resonance (fit in black) and measured AC frequency spectrum at each 1 pm laser wavelength step (plot background with colour-scale spectrum amplitude). The mechanical mode appears at $\omega_{\mathrm{m}}/2\pi \approx 2397$ MHz, and an electro-optic phase modulator calibration tone is visible at $\omega_{\mathrm{EOM}}/2\pi = 2395$ MHz.

would permit measurements with less optical heating, and the measurement would additionally be performed with the laser tuned to the optical resonance frequency, which would eliminate any potential error from optical back-action effects.

The goal of this experiment is to demonstrate that the cooling power of our dilution refrigerator is enough to cool the optomechanical crystal into the thermal ground state, where the phonon occupation of the mechanical breathing mode is less than one $\bar{n}_{\mathrm{th}} < 1$, which would allow the mechanics to be used as a low-noise bridge for transducing microwave photons to telecom frequencies. A secondary goal is to determine the optomechanical cooperativity, to determine if the device is capable of reaching $C > 1$ at low temperature for high-efficiency transduction. Optical heating of the mechanical mode makes both of these goals challenging to realize, since heating increases both the thermal phonon occupation of the mechanical mode and the mechanical damping rate, which we recall to be a component of the
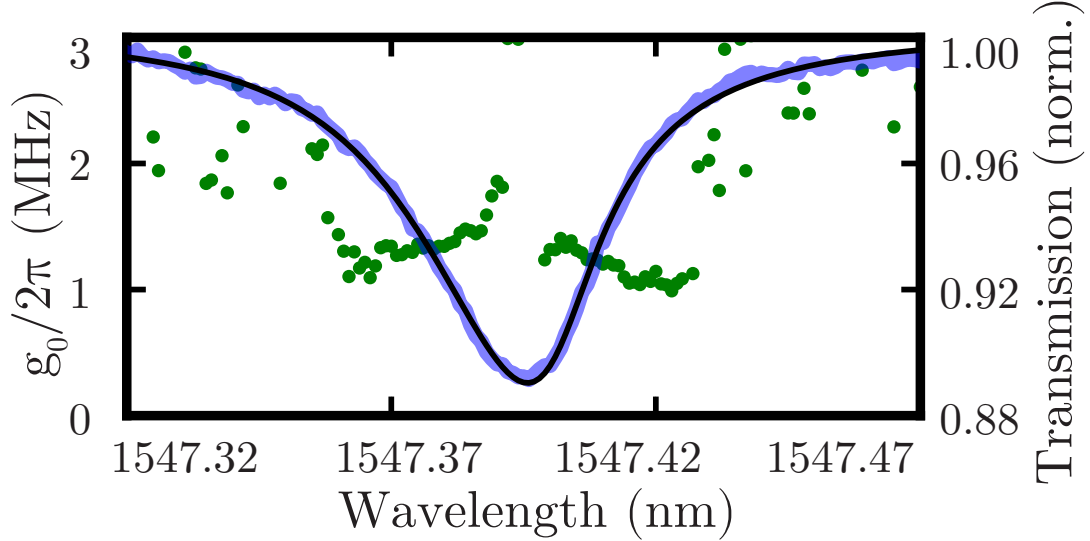
Figure 6.5: Calculation of the optomechanical coupling using phase calibration (green dots), with the optical resonance (blue) as reference for the detuning at which each calculation is made. The trend towards higher g_0 at the center of the optical resonance reflects the temperature dependent nature of Eqn. (3.42) in the presence of optical photon absorption. The outlier points below 1547.36 nm and above 1547.43 nm are shown to demonstrate the variance of low-signal measurements, but are not used in the calculation of g_0.

cooperativity. This problem of optical heating is not unique to our experiment, and was first characterized for silicon optomechanical crystals [106, 107], where the rate and magnitude of heating was measured using optical pulses and single photon counters. The optical pulsing techniques were then adapted to measure heating in optical microdisks with megahertz-frequency mechanical cantilevers using conventional photodetectors [108]. Here, we adapt the optical pulsing technique to measure our gigahertz mechanical mode using optical heterodyne detection.

6.4 Pulsed Measurement

Optical pulses are created using a high-speed acousto-optic modulator[2] (AOM), which is shown in a simplified schematic of the optical measurement system Fig. 6.6(a). The AOM is switched to an 'on' state when a 2 W, 200 MHz sinusoidal signal is applied to the RF input port. Otherwise it blocks light from being

---

[2]Gooch & Housego 200 MHz Longitudinal acousto-optic modulator

transmitted. The pulses are created prior to the phase detection beamsplitter (here labelled as a variable coupler to reflect the ability to tune the amount of light in each arm). Another option is to insert the AOM into the signal arm, so that the local oscillator is on continuously. The primary advantage of placing the AOM outside of the phase detection system is that the photodetector receives no light between pulses, which makes it easy to distinguish when an optical pulse is measuring the optomechanical crystal.

The RF signal used to drive the AOM is generated by a linear chain of electronics that begins with a computer-controlled data acquisition card[3] which outputs a trigger to a pulse generator.[4] The pulse generator in turn is used to gate a signal generator[5] which outputs a 200 MHz sinusoidal signal during the pulse. The sinusoid is then amplified using a high-speed amplifier[6] to a 2 W output to provide sufficient power to drive the AOM, which converts the electrical pulse into the optical pulse used to measure the optomechanical crystal. In addition to this linear pulse generation chain, the data acquisition card is used to simultaneously send a trigger signal to the high-speed analog-to-digital converter, which allows data to be taken for only a brief period of time around each measured pulse. This is crucial to limit the size of data files taken and allows for faster analysis of the data captured in the pulsed experiments.

The pulsed data presented in the following sections represents averages over many repetitions, which is necessary to accommodate phase drift between the signal and local oscillator arms. In continuous measurements, we were able to lock the phase of the arms together using the DC difference signal from the balanced photodetector. Because of the discrete nature of pulses, however, the arms cannot be locked during pulsed measurement. Instead, up to $20,000$ repetitions are used to ensure the data is taken over an average of all possible phase shifts between the signal and local oscillator arms.

The use of the high-speed analog-to-digital converter instead of the real-time spectrum analyser, which was used for the majority of the continuous

---

[3]National Instruments USB-6259 multifunction IO
[4]Hewlett Packard 8131A 500 MHz pulse generator
[5]Stanford Research Systems SG382 2 GHz RF signal generator
[6]ENI 403L 37dB 250 MHz RF amplifier
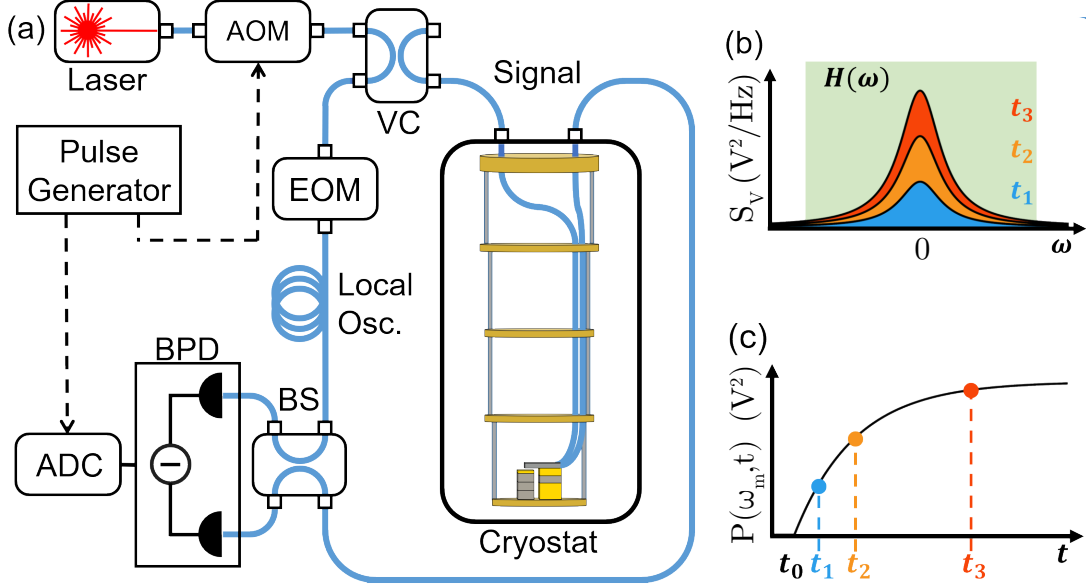
Figure 6.6: (a) Simplified schematic of optical heterodyne detection. AOM: acousto-optic modulator, VC: variable coupler, EOM: electro-optic modulator, BS: beamsplitter, BPD: balanced photodiode, ADC: analog-digital converter. (b) Cartoon of frequency-domain mechanical signal at three different times during a pulse. The mechanical signal is convolved with the green filter $H(\omega)$ to obtain (c) the time-dependent mechanical area.

measurement experiments in this chapter, reflects the need for high-speed time-domain measurements to capture the dynamics of mechanical heating. The spectrum analyser excels at frequency-domain measurements due to the presence of an internal mixer that downmixes the signal of interest to within the 40 MHz sample rate of the spectrum analyser. However, this sample rate is slower than the AOM switching time and could result in the pulse-edge being smoothed over several data points. Additionally, software limitations of the real-time spectrum analyser made it difficult to measure and process time-domain data.

In Fig. 6.6(a), a simplified picture of the heterodyne detection scheme used for pulsed measurement is demonstrated. The mechanical signal is optically downmixed by the electro-optic modulator tone to approximately 30 MHz. To analyse the time domain behaviour of the mechanical motion, a voltage signal $V(t)$, which carries mechanical information at the heterodyne downmixed frequency $\omega_{\mathrm{m}} - \omega_{\mathrm{EOM}}$, is digitally downmixed (demodulated) such that the center frequency of mechanical mode is set to zero: $\omega_{\mathrm{m}} - \omega_{\mathrm{EOM}} - \omega_{\mathrm{demod}} = 0$. We expect, due to optical absorption

heating, the mechanical power spectral density peak to grow in area over the duration of the optical pulse. To measure the peak area as a function of time, we digitally filter the downmixed signal using a 6.25 MHz filter window[7] $H(\omega)$ that is centered around zero frequency. In Fig. 6.6(b), a cartoon of the mechanical resonance at three points in time is shown to demonstrate the growth in peak area. The peak is wholly encapsulated by the filter function, here shown as a rectangular window. The convolution[8] of the window function with the demodulated pulse signal $V(t)e^{-i\omega_{\text{demod}}t}$, produces the area overlap of the mechanical resonance and the window, which is the time-dependent power spectral density area:

$$\mathcal{P}(\omega_{\text{m}}, t) = \left[V(t)e^{-i\omega_{\text{demod}}t}\right] * H(t) \tag{6.4}$$

The convolution effectively slides the filter window across the measured pulse, providing a time-domain record of the mechanical peak area over the duration of the optical pulse.[9] A cartoon example of this measurement is shown in Fig. 6.6(c), which shows the power spectral density growing from some initial area at t_0 to progressively larger values.

6.4.1 Two Bath System

To describe the transition that occurs over the duration of an optical pulse, we consider a two-bath system. The first bath is that of the dilution refrigerator, which is dominant prior to the onset of the pulse at $t = t_0$. The dilution refrigerator bath is coupled to the mechanical mode at the zero-phonon damping rate Γ_{m} and populates the mechanical mode with some number of thermal phonons $\bar{n}_{\text{th}}$. By turning on the laser and populating the optical mode with photons, we induce a second bath, which was introduced in Ref. [107] as the laser-induced hot-phonon bath. The hot-phonon bath consists of n_{p} phonons which couple to the mechanical mode at a rate Γ_{p}. The simplest model to which one could fit the transition from

---

[7]The filter function used for the data analysed in Ref. [2] was a Blackman window. Other options, such as a Hamming or Han window can also be used. Further research is required to determine what the ideal filtering window, but one interesting option for future exploration is to use the (normalized) mechanical lineshape from continuous measurements as a filtering function.

[8]Using the fftconvolve function in SciPy library [109].

[9]The demodulation and convolution procedure was developed by Doolin and is detailed in his thesis [78]

the dilution refrigerator bath to a combined bath is an instantaneous onset of the hot-phonon bath at the beginning of the optical pulse (at time t_0). The mechanical mode phonon occupancy $n(t)$ then increases from its initial occupancy $n(t_0)$ to the thermal equilibrium $n_{\mathrm{eq}} = (\Gamma_{\mathrm{m}} n_{\mathrm{th}} + \Gamma_{\mathrm{p}} n_{\mathrm{p}})/\Gamma$ at a rate $\Gamma = \Gamma_{\mathrm{m}} + \Gamma_{\mathrm{p}}$ according to

$$n(t) = n(t_0)e^{-\Gamma(t-t_0)} + n_{\mathrm{eq}} \left(1 - e^{-\Gamma(t-t_0)}\right). \tag{6.5}$$

We note that this equation does not assume that the bath necessarily start thermalized to the dilution refrigerator bath—if this is the case, then $n(t_0) = \bar{n}_{\mathrm{th}}$.

At this juncture we recall Eqn. (6.2), which implies that the phonon occupancy of the mechanical mode is proportional to the power spectral density area. Thus, the equation governing phonons in the mechanical mode also governs the time-dependent power spectral density areas $\mathcal{P}(\omega_{\mathrm{m}}, t)$ cartooned in Fig. 6.6(c). In the following sections we will use the two-bath model describing the mechanical dynamics created using optical pulses first to corroborate the zero-photon damping rate measured from the heuristic fit in Fig. 6.2(b), and second to create a calibration metric that can be used to calculate the number of phonons in our device.

6.4.2 Measurement in the Dark

In prior measurements, the mechanical damping rate was calculated by fitting the mechanical resonance and extracting the linewidth. This is based on our model of the mechanical motion as a harmonic oscillator and is a result of the assumptions made from input-output theory in deriving the mechanical equation of motion Eqn. (2.12). Although this theory is generally a robust description of our mechanical motion, it is limited in its ability to distinguish between different modes of dissipation, and thus cannot separate dissipation that arises from optical absorption and other, non-measurement-induced sources.

A more physical approach to determining the mechanical damping rate is to directly observe the length of time required for mechanical energy to dissipate. This is an impossible experiment in a continuous measurement scheme where the mechanics is in equilibrium, but by using one optical pulse to excite the mechanical motion and then capturing the mechanical motion as it rings down using a second measurement a variable amount time later, the rate at which the mechanics dissipate
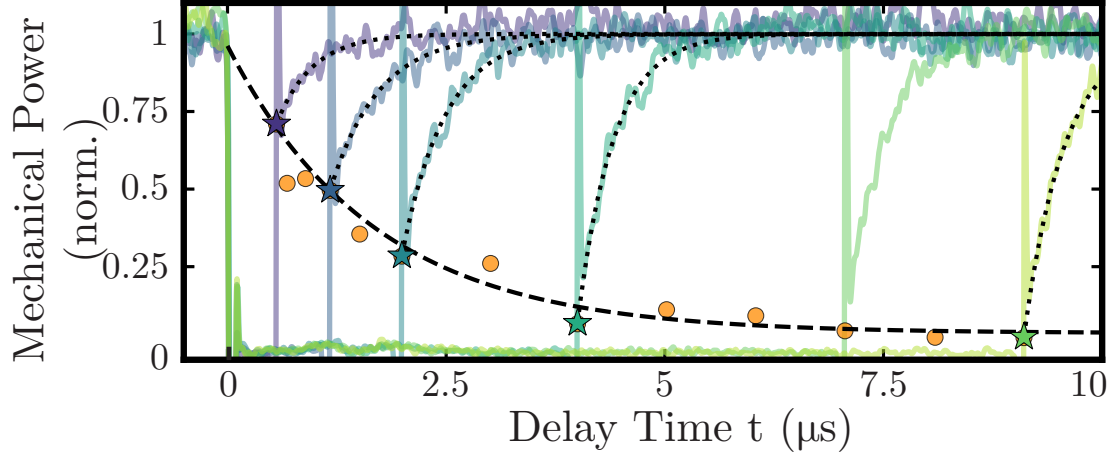
Figure 6.7: Measurement in the dark, or a double-pulse measurement. The power spectral density area is normalized to the equilibrium amplitude of the first pulse, and time shifted such that the falling edge of the first pulse is aligned to $t = 0$. The second pulse occurs some delay time t_0 later, and is fit (black dotted lines) using Eqn. (6.5), which is normalized by dividing by $\bar{n}_{\mathrm{eq}}$. The initial occupancy of each secondary pulse $n(t_0)$ is plotted as a star for example traces, and as an orange dot for traces not shown (one pulse is shown without a fit to elucidate the pulse itself). These initial occupancies are then fit (black dashed line) to Eqn. (6.6) to extract $\Gamma_{\mathrm{m}}/2\pi = 83$ KHz.

the energy of the first pulse can be traced out. In the time between the pulses, no photons exist within the optical cavity and as a result the mechanics are not affected by optical-absorption-induced damping. For this reason this experiment is referred to as a measurement in the dark.

In Fig. 6.7 we perform the measurement in dark, wherein two pulses are separated by a delay time that is varied from 1 μs to 9 μs. The first pulse heats the mechanics to an equilibrium state, which decays when the pulse ends. The second pulse, which begins after some delay time, captures the mechanics partway through the decay process and causes them to return to the excited state. The power spectral density area, calculated as a function of time using Eqn. (6.4), is fit to Eqn. (6.5) to describe the return to the equilibrium state. In the time between the optical pulses, the hot-phonon bath vanishes nearly instantaneously (the optical time constant is $1/\kappa \approx 32$ ps) and the mechanical mode decays back to the dilution refrigerator bath at the mechanical damping rate Γ_{m}. By increasing the delay time between the optical pulses and recording the initial phonon number $n(t_0)$, the mechanical

mode decay from the two-bath equilibrium to the dilution refrigerator bath can be captured using a series of trials. The decay from the two-bath equilibrium state to the dilution refrigerator thermal state can be described using Eqn. (6.5) with $\Gamma_{\mathrm{p}} = 0$. For clarity, the equation is re-written as

$$n(t) = \bar{n}_{\mathrm{eq}} e^{-\Gamma_{\mathrm{m}} t} + \bar{n}_{\mathrm{th}} \left(1 - e^{-\Gamma_{\mathrm{m}} t}\right). \tag{6.6}$$

Fitting the set of initial phonon occupancies to Eqn. (6.6) allows us to calculate the mechanical damping rate Γ_{m} in the absence of the hot-phonon bath. The outcome of the measurement in the dark experiment is a mechanical damping rate $\Gamma_{\mathrm{m}}/2\pi = 83$ KHz which agrees well with the heuristically fit zero-photon mechanical damping rate $\Gamma_{\mathrm{m}}(0)/2\pi = 79.9$ KHz.

6.4.3 Phonon Calibration

The next experimental step is to use optical pulses to determine the proportionality between the power spectral density area and the number of phonons in the mechanical mode. For simplicity, we absorb all proportionality constants in Eqn. (6.2) into one variable, such that $2\alpha g_0^2/\omega_{\mathrm{m}}^2 \to \alpha$. We also separate noise into three distinct sources: measurement imprecision $\mathcal{P}^{\mathrm{imp}}$, which arises from sources such as electronic noise in the photodetector and accounts for off-resonance background noise; ground state noise $\mathcal{P}^{\mathrm{gs}}$ which arises from the groundstate motion of the mechanical mode; and backaction noise $\mathcal{P}^{\mathrm{ba}}$, which represents the transfer of photon momentum into the mechanical mode. The total measured power spectral density area is then

$$\mathcal{P}^{\mathrm{meas}}(\omega_{\mathrm{m}}) = \alpha \bar{n}_{\mathrm{th}} + \left[\mathcal{P}^{\mathrm{imp}} + \mathcal{P}^{\mathrm{ba}} + \mathcal{P}^{\mathrm{gs}}\right]. \tag{6.7}$$

This expansion makes it clear that only the power in the mechanical peak $\mathcal{P}(\omega_{\mathrm{m}}) = \alpha \bar{n}_{\mathrm{th}}$ is proportional to the number of phonons. For our calibration, we must determine both the proportionality constant α and the total noise power, which is the bracketed quantity in Eqn. (6.7). To begin, we consider the measurement imprecision, which is mostly independent of frequency. In Fig. 6.8, an example of the the mechanical peak area and measurement imprecision noise floor is shown. The noise floor power is calculated by demodulating the measured
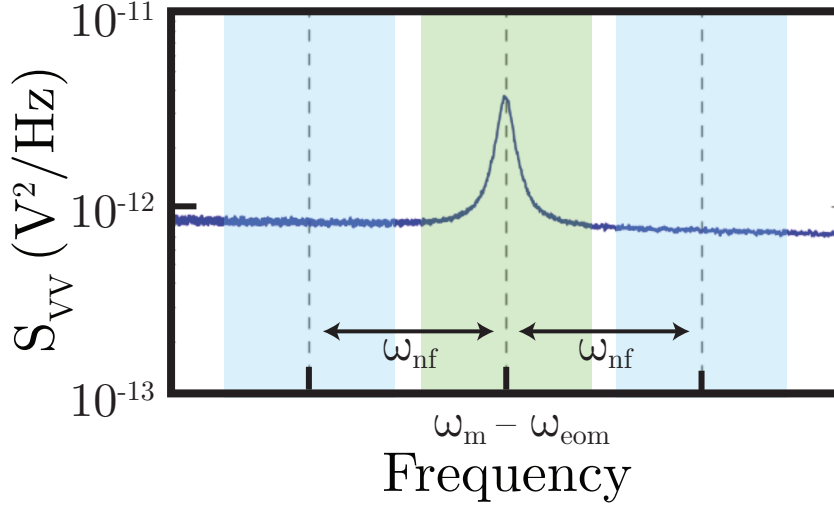
Figure 6.8: Continuous measurement of the mechanical mode with vertical dashed lines showing the demodulation frequency for calculating the mode area, and the two offset frequencies for calculating the noise floor area. Overlaid on the plot are three windows representing the filter bandwidth around the noise floor demodulations (blue) and the mechanical mode demodulation (green).

voltage signal by a frequency offset from the mechanical mode by some amount ω_{nf}, which is set such that the filter window surrounding the noise floor demodulation frequency does not include the mechanical mode, and moreover, does not include any peaks from other noise sources. By calculating noise floors on either side of the mechanical resonance we can account for slight tilts in the imprecision noise floor by averaging the measured powers. From the measurement shown in Fig. 6.8 we find $\mathcal{P}^{\mathrm{imp}} = 0.726$ mV^2.

After subtracting off the imprecision noise floor, the calibration of the remaining mechanical peak area proceeds by taking single-pulse measurements at a variety of dilution refrigerator temperatures. As previously noted, at high temperatures $T_{\mathrm{MC}} > 1.5$ K, we assume that the thermal coupling between the mixing chamber thermometer and the optomechanical crystal is sufficient for the device to be thermalized. We can therefore use pulsed measurements above this temperature to provide our calibration.

The phonon calibration measurement data is presented in Fig. 6.9, where we use Eqn. (6.5) to fit the mechanical area growth over the duration of a pulse for a broad range of temperatures between $T_{\mathrm{MC}} = 20$ mK ~ 6.5 K. For this experiment, a
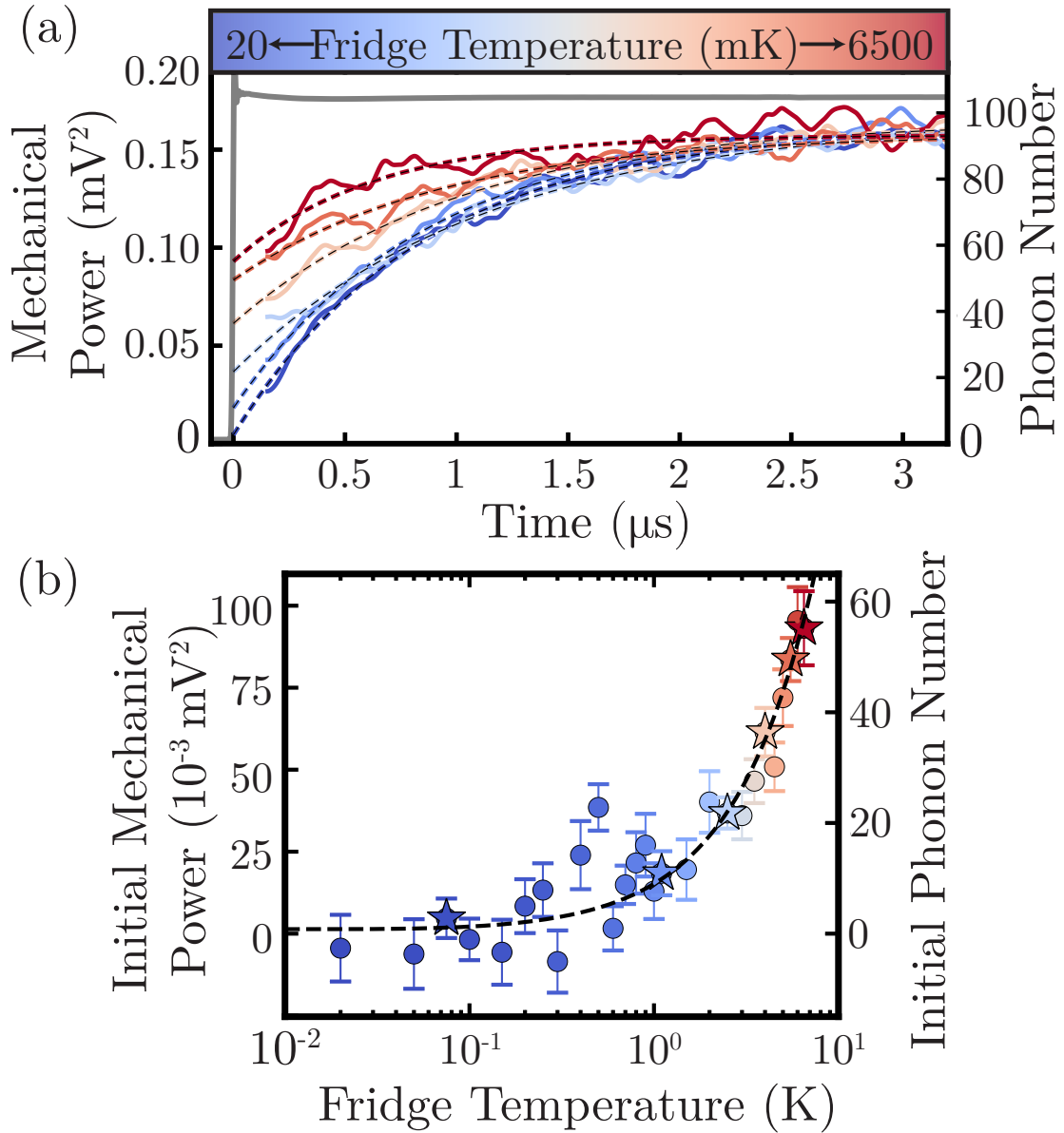
Figure 6.9: (a) Heterodyne pulsed measurements showing the thermomechanical noise of the mechanical mode as a function of time. Measurements are truncated to begin at 0.25 μs after the optical pulse (grey) due to the 6.25 MHz bandwidth of the filter function. Fits to Eqn. (6.5) (dashed lines) are used to extrapolate the pulses back to $t = 0$. Left axis presents the data in terms of power spectral density peak area. Right axis shows recalibrated data in terms of phonon number. (b) The peak areas at the onset of the optical pulse, color-coded to match the fridge temperature scale, with stars to denote the example traces from (a). Peak areas from high temperature data $T \geq 1.5$ K are used to calibrate the initial peak area to phonon number. The complete data set is fit to the Bose-Einstein distribution with an offset (black dashed) to determine the average number of phonons in the mechanical mode at 20 mK.

1.5 µW laser pulse (set by the minimum power needed for adequate signal-to-noise) is turned on at $t = 0$ and populates the optical mode with $\bar{n}_{\mathrm{cav}} \approx 230$ photons on a timescale of $1/\kappa = 32$ ps. Absorption of photons in the optical mode causes the device to consistently heat to a temperature above 6.5 K regardless of the initial starting temperature. Each trace of the peak area is fit to Eqn. (6.5) to extract the initial and final mechanical peak areas. In addition, a total damping rate $\Gamma/2\pi = 1.05$ MHz is calculated for the combined two-bath system.[10]

At high temperatures, we assume that the device is thermalized to the dilution refrigerator when the measurement begins, which is supported by the linear relationship in Fig. 6.9(b). However, we do not assume that the device is thermalized at millikelvin temperatures, where the GaAs thermal conductivity drops significantly due to T^3 scaling [73]. For this reason only temperatures $T \geq 1.5$ K are used in the phonon number calibration. We fit the initial peak areas of the high temperature data using Eqn. (6.7) to determine the conversion factor α as well as the total noise $\mathcal{P}^{\mathrm{imp}} + \mathcal{P}^{\mathrm{ba}} + \mathcal{P}^{\mathrm{gs}} = 1.18$ mV^2. Using the prior imprecision measurement, we find $\mathcal{P}^{\mathrm{imp}}/(\mathcal{P}^{\mathrm{ba}} + \mathcal{P}^{\mathrm{gs}}) = 1.6$, which suggests these measurements are performed near the standard quantum limit measurement power where $\mathcal{P}^{\mathrm{ba}} = \mathcal{P}^{\mathrm{imp}}$ [33].

In Fig. 6.9(b), the initial peak areas are plotted with noise terms subtracted (left axis) and recalibrated to initial phonon number (right axis) using the conversion factor α. The initial phonon numbers are then fit using the Bose-Einstein distribution to find the thermal offset between the device and the fridge at base temperature. At a fridge temperature of 20 mK we find that the mean phonon occupancy is initially $n(t_0) = 0.7 \pm 0.4$, with 95% confidence from the fit. This implies that the mechanical mode thermalizes to 0.13 ± 0.05 K when the fridge thermometry reads 0.02 K. Applying the calibration to the time-resolved measurements in Fig. 6.9(a) shows that the mechanical mode saturates to a thermal occupancy of 95 phonons in 3 µs.

---

[10]This differs from the value that can be read off of Fig. 6.2(b), possibly due to a change in the fiber coupling. Further investigation is required to understand this discrepancy.

6.5 Low Temperature Cooperativity

In calculating the optomechanical cooperativity at low temperatures we must take care to discern between the intrinsic cooperativity that is set entirely by device properties and an effective cooperativity [107], which includes measurement-induced heating—the hot-phonon bath. The effective cooperativity supersedes the intrinsic optomechanical cooperativity as the relevant figure for quantum-state transduction experiments, as it exchanges the damping rate Γ_{m}, which describes the loss of phonons to the environment, for $\Gamma \bar{n}_{\mathrm{eq}}$, which describes at which the mechanical mode decoheres due to thermal noise. Decoherence was not a relevant factor for our room-temperature demonstration of classical signal transduction in Chapter 5, but it will become crucial in the eventual application of quantum state transduction. We begin by considering the intrinsic cooperativity [33],

$$C = \frac{4g_0^2 \bar{n}_{\mathrm{cav}}}{\kappa \Gamma_{\mathrm{m}}} = 3.7, \tag{6.8}$$

which is sufficient to achieve high-efficiency, classical-signal, microwave-to-telecom transduction, as it implies that in the absence of the hot-phonon bath phonons are probabilistically converted into optical photons rather than lost to the environment through mechanical damping.

In contrast, we now consider the hot-phonon bath created by the laser pulse, which consists of $\bar{n}_{\mathrm{eq}} = 95$ phonons which couple to the mechanical mode at a rate $\Gamma/2\pi = 1.05$ MHz to decohere the mechanical state. The resulting effective cooperativity is [23, 97, 107]

$$C_{\mathrm{eff}} = \frac{4g_0^2 \bar{n}_{\mathrm{cav}}}{\kappa \Gamma \bar{n}_{\mathrm{eq}}} = 3 \times 10^{-3}. \tag{6.9}$$

Hence we see that the effective optomechanical cooperativity is severely limited by the presence of the hot-phonon bath and that reducing the amount of heating is crucial to future quantum applications. Our hypothesis is that reducing the optical absorption will result in a corresponding reduction in the magnitude of the hot-phonon bath, which is evidenced by Fig. 6.2(b) where the measured damping rate changes with number of photons in the cavity. There are two potential approaches to mitigating optical absorption: passivating the GaAs surface to

reduce roughness [40] and the influence of mid-gap surface states [110] may result in reduced optical absorption at the surfaces of the optomechanical crystal [111], or simply migrating to a material with a larger bandgap to increase the required energy of absorption [112].

Another point of focus is the intrinsic damping rate of the mechanics, which was expected to be lower than the measured zero-photon damping rate $\Gamma_m/2\pi = 83$ kHz. The high damping rate will limit both the optomechanical and piezomechanical cooperativity unless it is significantly improved in future experiments. Discovering the limiting factor of the damping rate is tricky, as it could arise from a number of sources; once again surface roughness is a culprit [40], but other possibilities include two-level systems [113], clamping losses [114], and the need for improved phononic shielding [115].

6.6 Future Low Temperature Piezo-optomechanical Systems

At this juncture, we can compile our results in Table 6.1, which contains measured low temperature characteristics and predicted piezomechanical coupling characteristics for a future scenario where we have a piezo-optomechanical system built around the architecture of gallium arsenide optomechanical crystals in a 3D microwave cavity at low temperatures. Here we consider the immediate next step of classical signal conversion at low temperatures, for which we consider the optomechanical cooperativity instead of the effective cooperativity.

Considering a scenario where the optomechanical cooperativity is enhanced using a red-detuned pump, the efficiency of transduction, calculated using Eqn. (5.11), would be $\eta \approx 10^{-9}$, improving by four orders of magnitude from a similar room temperature experiment. Although this improvement is a step towards efficient transduction, it is clear that low temperatures alone are not sufficient.

Instead, the assertion from Chapter 4 that permanent fiber coupling is required to allow for better mode overlap between the microwave electric field and mechanical mode must be reiterated. By increasing the mode overlap, the piezomechanical coupling can be increased and the piezoemechanical cooperativity can then begin

	Optics (GHz)	Mechanics (MHz)	Microwaves (MHz)
Wavelength	$\lambda_c \approx 1543$ nm	—	—
Frequency	$\omega_c/2\pi \approx 194300$	$\omega_m/2\pi \approx 2387.5$	$\omega_\mu/2\pi \approx 2386.5$
Tot. decay rate	$\kappa/2\pi \approx 6.6$	$\Gamma_m/2\pi \approx 0.083$	$[\kappa_\mu/2\pi \approx 0.1]$
Ext. decay rate	$\kappa_e/2\pi \approx 2.3$	—	$[\kappa_{\mu,e}/2\pi \approx 0.05]$
Mode coupling	$g_0/2\pi = (1.3 \pm 0.3)$ MHz		$g_\mu/2\pi = (4.3 \pm 0.8)$ Hz
Cooperativity	$C = 3.7$		$[C_\mu \approx 10^{-8}]$

Table 6.1: Summary of low temperature piezo-optomechanical properties of the gallium arsenide optomechanical crystal used for classical microwave to telecom transduction, with predicted values [102, 104] encapsulated in square brackets. This table assumes there is no hot-phonon bath from optical absorption.

to approach a value exceeding one. Permanent fiber coupling also solves a spatial problem that becomes evident when comparing the size of the microwave cavity in photographed in Fig. 5.2(a) to the photograph of the dilution refrigerator baseplate shown in Fig. 6.1(a): the microwave cavity and the stages required for positioning the chip relative to a dimpled tapered fiber will not all fit on the baseplate! Hence, permanent fiber coupling is a requirement for this type of low-temperature transduction experiment in our dilution refrigerator.

6.7 Transduction Noise

Reaching the thermal groundstate in the mechanical breathing mode is an important benchmark when considering thermal decoherence rates for quantum state transduction. Considering that microwave-actuated phonons and thermal phonons are transduced into telecom photons identically further provides an intuitive description of how thermal noise becomes noise added to the transduced signal. To quantify this description we return to the piezo-optomechanical equations of motion, Eqn. (5.8). To find the transduction noise from the thermal population of the mechanical mode, we calculate the amount of light emmited from the telecom mode when the system is driven solely by thermomechanical motion. The number

of noise-addded photons in the telecom signal is

$$n_{\text{add}} = \kappa_{\text{e}}|\delta\hat{a}(\omega_{\text{s}})|^2 \tag{6.10}$$

$$= \kappa_{\text{e}}\Gamma_{\text{m}} \left| \frac{|\bar{\alpha}|g_0\hat{b}_{\text{in}}}{\chi_{\text{a}}^{-1}(\omega_{\text{s}})\chi_{\text{b}}^{-1}(\omega_{\text{s}})\chi_{\text{c}}^{-1}(\omega_{\text{s}}) + g_0^2|\bar{\alpha}|^2\chi_{\text{c}}^{-1}(\omega_{\text{s}}) + g_{\mu}^2\chi_{\text{a}}^{-1}(\omega_{\text{s}})} \right|^2. \tag{6.11}$$

Like the equation for transduction efficiency, we simplify the general expression for added thermal noise for our specific scenario where the transduction frequency approximately matches the microwave and mechanical mode frequencies, $\omega_{\text{s}} \approx \omega_{\text{m}} \approx \omega_{\mu}$ and the laser is set to be on the optical resonance, $\Delta = 0$. The number of added thermal noise photons then becomes[11]

$$n_{\text{add}} = \frac{\kappa_{\text{e}}}{\kappa} \frac{4Cn(t_0)}{(1 + C + C_{\mu})^2 + \frac{4\omega_{\text{m}}}{\kappa^2}(1 + C_{\mu})^2}. \tag{6.12}$$

For this simplification we have assumed no hot-phonon bath, but that can be straightforwardly calculated by exchanging the number of phonons and damping rate $n(t_0)$ from the dilution refrigerator for the continuous-limit equilibrium bath $\bar{n}_{\text{eq}}$, and the cooperativities for effective cooperativities. Using the values from Table 6.1, we find that the dilution refrigerator adds just $n_{\text{add}} = 0.2$ quanta, where a quanta is one added telecom photon in the transduced signal per second in a 1 Hz bandwidth [23].

The number of added photons intertwines two concepts: first, how many thermal phonons are in the mechanical mode, and second, how well they are transduced into the optical mode and then out to the coupling fiber. The fact that the number of added photons increases both when the phonon population increases (which is bad) and when cooperativity increases (which is good) makes the number of added photons a poor metric for how low-noise the transduced signal is, despite the fact that it literally describes how much noise is in the signal. To provide a better metric for defining "low-noise" transduction, we consider the signal-to-noise ratio [23, 97],

$$\text{SNR} = \frac{\kappa_{\mu,\text{e}}}{\kappa_{\mu}} \frac{C_{\mu}|\hat{c}_{\text{in}}|^2}{n(t_0)}, \tag{6.13}$$

---

[11]This equation differs from the calculation made in Ref. [2], where no assumption of a microwave cavity was made.

which was derived solving Eqn. (5.8) for $\hat{a}$ when $\hat{c}_{\text{in}}$ is the sole input and dividing the result by the solution to $\hat{a}$ when $\hat{b}_{\text{in}}$ is the sole input. In future transduction experiments at low temperature, this signal-to-noise ratio should be calculated to determine degree to which thermal noise of the mechanical resonator pollutes a signal as it is transduced from the microwave domain to the optical domain. For the present experiment, there was no signal transduced and therefore the signal-to-noise ratio remains undefined.

6.8 Experiment Summary

The low-temperature experiments described in this chapter were successful in showing that the millikelvin dilution refrigerator environment is sufficient to cool the gallium arsenide piezo-optomechanical crystals into the thermal ground-state at 0.7 ± 0.4 phonons. The success however came with the caveat that the measurement itself induced a hot-phonon bath, which in Fig. 6.7(b) heats the mechanical mode to phonon occupations well outside the thermal groundstate at $\bar{n}_{\text{eq}} \approx 95$ phonons. The hot-phonon bath is similarly responsible for damping the mechanical mode at a rate which, judging from Fig. 6.2(b), appears to depend on the number of photons in the optical cavity. Unfortunately the phonon calibration measurement was only done for a single optical power, which prevents us from using the calibrated measurements to confirm the relation between optical photons and the hot-phonon bath. This could provide the basis for a future investigation, although the experiment would be technically challenging due to the sheer volume of data required for a measurement that varies both fridge temperature and optical power. It was not a feasible experiment for dimple-tapered fiber coupled devices due to the limited amount of time the fiber would remain coupled to the device—often the fiber would slowly shift relative to the device over a period of a few days, changing the measurement characteristics. Future experiments with permanent fiber coupling may not have this difficulty.

We have further calculated both the classical cooperativity, $C = 3.7$, and the effective cooperativity, $C_{\text{eff}} = 3 \times 10^{-3}$, which must be improved for the application of quantum state transduction. We have also used piezo-optomechanical theory

to separate the absolute noise in the signal from the signal-to-noise ratio of the transduced signal, which will provide a metric to help guide future low-noise microwave to telecom transduction experiments.

Chapter 7

Conclusions & Future Directions

The research presented in this thesis is a small slice of the larger project that is the creation of a quantum-enabled microwave-to-telecom transducer. We have developed a unique platform—the piezoelectric optomechanical crystal in a 3D microwave cavity, and demonstrated the ability to transduce classical signals while preserving phase and amplitude information. Moreover, we performed pulsed optomechanics experiments at millikelvin temperatures to demonstrate that the mechanical mode of our transducer could be cooled to the thermal groundstate with 0.7 ± 0.4 phonons using dilution refrigeration. These results are encouraging for our prototype system, but leave a great deal of room for improvement. The measured transduction efficiency, $\eta = 10^{-15}$, must be improved to tens-of-percent to be competitive with low-frequency classical microwave-to-telecom converters [25]. Mechanical mode heating from optical absorption must also be eliminated or circumvented to reduce noise in the transduced signal.

Frequently mentioned throughout the thesis is the use of permanent fiber coupling in future iterations of piezo-optomechanical transduction devices, which will allow for increased overlap between microwave electric fields and mechanical motion and will in turn lead to increased mode coupling, cooperativity, and finally efficiency. At the same time, the redesign to allow for permanent fiber coupling provides an opportunity to examine causes of optical absorption and investigate potential solutions. Different piezoelectric materials are worthwhile investigations, especially with the recent successes of lithium niobate devices [30, 31]; if gallium

arsenide remains the material of choice, then surface passivation techniques [110] may also help incrementally.

Though the necessary addition of permanent fiber coupling and the possibility of changing materials are major optimization steps, they will not advance the precedent of microwave-to-telecom transduction experiments. For the period of time that my thesis work took place, the precedent was classical signal transduction, which provoked a competitive research field where many laboratories sought to demonstrate the best-in-class classical signal transduction system. Many of these experiments began to push the boundaries of quantum measurement by using single-photon counting techniques to characterize their transducers [29, 107], but was only during the writing of this thesis that the first actual microwave-to-telecom quantum state transduction took place in the Painter lab [70] where Rabi oscillations between the ground and excited states of a transmon qubit were detected using telecom single photon detectors. The quantum technologies (single photon detectors and transmon qubits) used in this demonstration are also available for use in the Davis lab, where they are being tested for future integration in optomechanics experiments.

This thesis provides a starting point for the development of future quantum-enabled microwave-to-telecom transducers. The measurements of phonon occupation and cooperativity in Chapter 6, and efficiency in Chapter 5, are interesting as proof-of-principle demonstrations. The true value of this work, however, comes from the measurement systems outlined in Chapter 3, which are designed for use with gigahertz-frequency mechanical modes. In particular, the heterodyne and homodyne downmixing schemes will remain crucial for the characterization of future devices, and the digital processing techniques used for the low-IF receiver will likely be a cornerstone of future quantum measurements [84, 116]. In addition, the piezo-optomechanical theory outlined in Chapter 5, and the piezomechanical background developed in Chapter 4 should serve as a starting point for the development of new and improved microwave-to-telecom transduction devices.

References

[1] H. Ramp, T. J. Clark, B. D. Hauer, C. Doolin, K. C. Balram, K. Srinivasan, and J. P. Davis, "Wavelength transduction from a 3D microwave cavity to telecom using piezoelectric optomechanical crystals," Applied Physics Letters **116**, 174005 (2020).

[2] H. Ramp, B. D. Hauer, K. C. Balram, T. J. Clark, K. Srinivasan, and J. P. Davis, "Elimination of thermomechanical noise in piezoelectric optomechanical crystals," Phys. Rev. Lett. **123**, 093603 (2019).

[3] F. Arute et al., "Quantum supremacy using a programmable superconducting processor," Nature **574**, 505–510 (2019).

[4] S. Krinner, S. Storz, P. Kurpiers, P. Magnard, J. Heinsoo, R. Keller, J. Lütolf, C. Eichler, and A. Wallraff, "Engineering cryogenic setups for 100-qubit scale superconducting circuit systems," EPJ Quantum Technology **6**, 2 (2019).

[5] A. J. Wallraff, "Microwave quantum network linking cryogenic systems for superconducting-circuit-based quantum computing (conference presentation)," in Quantum technologies 2020, edited by S. Ducci, E. Diamanti, N. Treps, and S. Whitlock (Mar. 2020).

[6] E. Saglamyurek, T. Hrushevskyi, L. Cooke, A. Rastogi, and L. J. LeBlanc, "Single-photon-level light storage in cold atoms using the Autler-Townes splitting protocol," Physical Review Research **1**, 022004 (2019).

[7] P. Kómár, E. M. Kessler, M. Bishof, L. Jiang, A. S. Sørensen, J. Ye, and M. D. Lukin, "A quantum network of clocks," Nature Physics **10**, 582–587 (2014).

[8] F. Marsili, V. B. Verma, J. A. Stern, S. Harrington, A. E. Lita, T. Gerrits, I. Vayshenker, B. Baek, M. D. Shaw, R. P. Mirin, and S. W. Nam, "Detecting single infrared photons with 93% system efficiency," Nature Photonics **7**, 210–214 (2013).

[9] S. Barzanjeh, S. Guha, C. Weedbrook, D. Vitali, J. H. Shapiro, and S. Pirandola, "Microwave quantum illumination," Physical Review Letters **114**, 080503 (2015).

[10] S. Kumar, N. Lauk, and C. Simon, "Towards long-distance quantum networks with superconducting processors and optical links," Quantum Science and Technology **4**, 045003 (2019).

[11] N. Lauk, N. Sinclair, S. Barzanjeh, J. P. Covey, M. Saffman, M. Spiropulu, and C. Simon, "Perspectives on quantum transduction," Quantum Science and Technology **5**, 020501 (2019).

[12] N. J. Lambert, A. Rueda, F. Sedlmeir, and H. G. L. Schwefel, "Coherent conversion between microwave and optical photons—an overview of physical implementations," Advanced Quantum Technologies **3**, 1900077 (2020).

[13] M. Tsang, "Cavity quantum electro-optics. II. input-output relations between traveling optical and microwave fields," Physical Review A **84**, 043845 (2011).

[14] A. Rueda, F. Sedlmeir, M. C. Collodo, U. Vogl, B. Stiller, G. Schunk, D. V. Strekalov, C. Marquardt, J. M. Fink, O. Painter, G. Leuchs, and H. G. L. Schwefel, "Efficient microwave to optical photon conversion: an electro-optical realization," Optica **3**, 597 (2016).

[15] C. Javerzac-Galy, K. Plekhanov, N. R. Bernier, L. D. Toth, A. K. Feofanov, and T. J. Kippenberg, "On-chip microwave-to-optical quantum coherent converter based on a superconducting resonator coupled to an electro-optic microresonator," Physical Review A **94**, 10.1103/physreva.94.053815 (2016).

[16] L. Fan, C.-L. Zou, R. Cheng, X. Guo, X. Han, Z. Gong, S. Wang, and H. X. Tang, "Superconducting cavity electro-optics: a platform for coherent photon conversion between superconducting and photonic circuits," Science Advances **4**, eaar4994 (2018).

[17] J. Han, T. Vogt, C. Gross, D. Jaksch, M. Kiffner, and W. Li, "Coherent microwave-to-optical conversion via six-wave mixing in Rydberg atoms," Physical Review Letters **120**, 093201 (2018).

[18] D. Petrosyan, K. Mølmer, J. Fortágh, and M. Saffman, "Microwave to optical conversion with atoms on a superconducting chip," New Journal of Physics **21**, 073033 (2019).

[19] A. A. Morgan and S. D. Hogan, "Coupling Rydberg atoms to microwave fields in a superconducting coplanar waveguide resonator," Physical Review Letters **124**, 10.1103/physrevlett.124.193604 (2020).

[20] R. Hisatomi, A. Osada, Y. Tabuchi, T. Ishikawa, A. Noguchi, R. Yamazaki, K. Usami, and Y. Nakamura, "Bidirectional conversion between microwave and light via ferromagnetic magnons," Physical Review B **93**, 174427 (2016).

[21] J. D. Teufel, D. Li, M. S. Allman, K. Cicak, A. J. Sirois, J. D. Whittaker, and R. W. Simmonds, "Circuit cavity electromechanics in the strong-coupling regime," Nature **471**, 204–208 (2011).

[22] J. D. Teufel, T. Donner, D. Li, J. W. Harlow, M. S. Allman, K. Cicak, A. J. Sirois, J. D. Whittaker, K. W. Lehnert, and R. W. Simmonds, "Sideband cooling of micromechanical motion to the quantum ground state," Nature **475**, 359–363 (2011).

[23] R. W. Andrews, R. W. Peterson, T. P. Purdy, K. Cicak, R. W. Simmonds, C. A. Regal, and K. W. Lehnert, "Bidirectional and efficient conversion between microwave and optical light," Nat. Phys. **10**, 321–326 (2014).

[24] T. Bagci, A. Simonsen, S. Schmid, L. G. Villanueva, E. Zeuthen, J. Appel, J. M. Taylor, A. Sørensen, K. Usami, A. Schliesser, and E. S. Polzik, "Optical detection of radio waves through a nanomechanical transducer," Nature **507**, 81–85 (2014).

[25] A. P. Higginbotham, P. S. Burns, M. D. Urmey, R. W. Peterson, N. S. Kampel, B. M. Brubaker, G. Smith, K. W. Lehnert, and C. A. Regal, "Harnessing electro-optic correlations in an efficient mechanical converter," Nature Physics **14**, 1038–1042 (2018).

[26] J. Bochmann, A. Vainsencher, D. D. Awschalom, and A. N. Cleland, "Nanomechanical coupling between microwave and optical photons," Nat. Phys. **9**, 712–716 (2013).

[27] K. C. Balram, M. I. Davanco, J. D. Song, and K. Srinivasan, "Coherent coupling between radiofrequency, optical and acoustic waves in piezo-optomechanical circuits," Nature Photonics **10**, 346–352 (2016).

[28] A. Vainsencher, K. J. Satzinger, G. A. Peairs, and A. N. Cleland, "Bi-directional conversion between microwave and optical frequencies in a piezoelectric optomechanical device," Applied Physics Letters **109**, 033107 (2016).

[29] M. Forsch, R. Stockill, A. Wallucks, I. Marinković, C. Gärtner, R. A. Norte, F. van Otten, A. Fiore, K. Srinivasan, and S. Gröblacher, "Microwave-to-optics conversion using a mechanical oscillator in its quantum ground state," Nat. Phys. **16**, 69–74 (2020).

[30] W. Jiang, R. N. Patel, F. M. Mayor, T. P. McKenna, P. Arrangoiz-Arriola, C. J. Sarabalis, J. D. Witmer, R. V. Laer, and A. H. Safavi-Naeini, "Lithium niobate piezo-optomechanical crystals," Optica **6**, 845 (2019).

[31] W. Jiang, C. J. Sarabalis, Y. D. Dahmani, R. N. Patel, F. M. Mayor, T. P. McKenna, R. V. Laer, and A. H. Safavi-Naeini, "Efficient bidirectional piezo-optomechanical transduction between microwave and optical frequency," Nature Communications **11**, 1166 (2020).

[32] C. Gardiner and P. Zoller, *Quantum Noise: A Handbook of Markovian and Non-Markovian Quantum Stochastic Methods with Applications to Quantum Optics*, 3rd edition, Springer Series in Synergetics (Springer, Berlin, 2004).

[33] M. Aspelmeyer, T. J. Kippenberg, and F. Marquardt, "Cavity optomechanics," Rev. Mod. Phys. **86**, 1391–1452 (2014).

[34] M. H. Bitarafan, H. Ramp, T. W. Allen, C. Potts, X. Rojas, A. J. R. MacDonald, J. P. Davis, and R. G. DeCorby, "Thermomechanical characterization of on-chip buckled dome Fabry–Perot microcavities," Journal of the Optical Society of America B **32**, 1214 (2015).

[35] M. H. Bitarafan, H. Ramp, C. Potts, T. W. Allen, J. P. Davis, and R. G. DeCorby, "Bistability in buckled dome microcavities," Optics Letters **40**, 5375 (2015).

[36] C. A. Potts, A. Melnyk, H. Ramp, M. H. Bitarafan, D. Vick, L. J. LeBlanc, J. P. Davis, and R. G. DeCorby, "Tunable open-access microcavities for on-chip cavity quantum electrodynamics," Applied Physics Letters **108**, 041103 (2016).

[37] M. Wu, A. C. Hryciw, C. Healey, D. P. Lake, H. Jayakumar, M. R. Freeman, J. P. Davis, and P. E. Barclay, "Dissipative and dispersive optomechanics in a nanocavity torque sensor," Phys. Rev. X **4**, 021052 (2014).

[38] S. G. Johnson, M. Ibanescu, M. A. Skorobogatiy, O. Weisberg, J. D. Joannopoulos, and Y. Fink, "Perturbation theory for Maxwell's equations with shifting material boundaries," Phys. Rev. E **65**, 066611 (2002).

[39] C. Baker, W. Hease, D.-T. Nguyen, A. Andronico, S. Ducci, G. Leo, and I. Favero, "Photoelastic coupling in gallium arsenide optomechanical disk resonators," Opt. Express **22**, 14072–14086 (2014).

[40] K. C. Balram, M. Davanco, J. Y. Lim, J. D. Song, and K. Srinivasan, "Moving boundary and photoelastic coupling in GaAs optomechanical resonators," Optica **1**, 414 (2014).

[41] R. Rivière, S. Deléglise, S. Weis, E. Gavartin, O. Arcizet, A. Schliesser, and T. J. Kippenberg, "Optomechanical sideband cooling of a micromechanical oscillator close to the quantum ground state," Phys. Rev. A **83**, 063835 (2011).

[42] J. D. Thompson, B. M. Zwickl, A. M. Jayich, F. Marquardt, S. M. Girvin, and J. G. E. Harris, "Strong dispersive coupling of a high-finesse cavity to a micromechanical membrane," Nature **452**, 72–75 (2008).

[43] D. Kleckner, B. Pepper, E. Jeffrey, P. Sonin, S. M. Thon, and D. Bouwmeester, "Optomechanical trampoline resonators," Opt. Express **19**, 19708–19716 (2011).

[44] A. Schliesser, P. Del'Haye, N. Nooshi, K. J. Vahala, and T. J. Kippenberg, "Radiation pressure cooling of a micromechanical oscillator using dynamical backaction," Phys. Rev. Lett. **97**, 243905 (2006).

[45] B. D. Hauer, P. H. Kim, C. Doolin, A. J. R. MacDonald, H. Ramp, and J. P. Davis, "On-chip cavity optomechanical coupling," EPJ Tech. Instrum. **1**, 4 (2014).

[46] B. Khanaliloo, M. Mitchell, A. C. Hryciw, and P. E. Barclay, "High-q/v monolithic diamond microdisks fabricated with quasi-isotropic etching," Nano Letters **15**, 5131–5136 (2015).

[47] M. Mitchell, B. Khanaliloo, D. P. Lake, T. Masuda, J. P. Hadden, and P. E. Barclay, "Single-crystal diamond low-dissipation cavity optomechanics," Optica **3**, 963 (2016).

[48] M. J. Rudd, P. H. Kim, C. A. Potts, C. Doolin, H. Ramp, B. D. Hauer, and J. P. Davis, "Coherent magneto-optomechanical signal transduction and long-distance phase-shift keying," Phys. Rev. Appl. **12**, 034042 (2019).

[49] J. D. Teufel, T. Donner, M. A. Castellanos-Beltran, J. W. Harlow, and K. W. Lehnert, "Nanomechanical motion measured with an imprecision below that at the standard quantum limit," Nat. Nanotechnol. **4**, 820–823 (2009).

[50] T. A. Palomaki, J. W. Harlow, J. D. Teufel, R. W. Simmonds, and K. W. Lehnert, "Coherent state transfer between itinerant microwave fields and a mechanical oscillator," Nature **495**, 210–214 (2013).

[51] M. Eichenfield, R. Camacho, J. Chan, K. J. Vahala, and O. Painter, "A picogram- and nanometre-scale photonic-crystal optomechanical cavity," Nature **459**, 550–555 (2009).

[52] A. H. Safavi-Naeini, T. P. Mayer Alegre, M. Winger, and O. Painter, "Optomechanics in an ultrahigh-Q two-dimensional photonic crystal cavity," Appl. Phys. Lett. **97**, 181106 (2010).

[53] J. Chan, T. P. Mayer Alegre, A. H. Safavi-Naeini, J. T. Hill, A. Krause, S. Gröblacher, M. Aspelmeyer, and O. Painter, "Laser cooling of a nanomechanical oscillator into its quantum ground state," Nature **478**, 89–92 (2011).

[54] E. Yablonovitch, T. Gmitter, and K. Leung, "Photonic band structure: the face-centered-cubic case employing nonspherical atoms," Physical Review Letters **67**, 2295–2298 (1991).

[55] M. Trigo, A. Bruchhausen, A. Fainstein, B. Jusserand, and V. Thierry-Mieg, "Confinement of acoustical vibrations in a semiconductor planar phonon cavity," Physical Review Letters **89**, 227402 (2002).

[56] M. Eichenfield, J. Chan, R. M. Camacho, K. J. Vahala, and O. Painter, "Optomechanical crystals," Nature **462**, 78–82 (2009).

[57] N. W. Ashcroft and N. D. Mermin, *Solid State Physics*, 1st edition (Brooks Cole, Belmont, 1976).

[58] A. H. Safavi-Naeini and O. Painter, "Design of optomechanical cavities and waveguides on a simultaneous bandgap phononic-photonic crystal slab," Optics Express **18**, 14926 (2010).

[59] S. Noda, K. Tomoda, N. Yamamoto, and A. Chutinan, "Full three-dimensional photonic bandgap crystals at near-infrared wavelengths," Science **289**, 604–606 (2000).

[60] K. H. Matlack, A. Bauhofer, S. Krödel, A. Palermo, and C. Daraio, "Composite 3D-printed metastructures for low-frequency and broadband vibration absorption," Proceedings of the National Academy of Sciences **113**, 8386–8390 (2016).

[61] K. Sakoda, *Optical properties of photonic crystals* (Springer Berlin Heidelberg, 2005).

[62] S.-i. Inoue, "Photonic crystals: manipulating light with periodic structures," in *Optical properties of advanced materials* (Springer Berlin Heidelberg, 2013), pages 39–65.

[63] B. D. Hauer, C. Doolin, K. S. D. Beach, and J. P. Davis, "A general procedure for thermomechanical calibration of nano/micro-mechanical resonators," Ann. Phys. **339**, 181–207 (2013).

[64] M. Davanco, S. Ates, Y. Liu, and K. Srinivasan, "Si3n4 optomechanical crystals in the resolved-sideband regime," Applied Physics Letters **104**, 041101 (2014).

[65] M. J. Burek, J. D. Cohen, S. M. Meenehan, N. El-Sawah, C. Chia, T. Ruelle, S. Meesala, J. Rochman, H. A. Atikian, M. Markham, D. J. Twitchen, M. D. Lukin, O. Painter, and M. Loncar, "Diamond optomechanical crystals," Optica **3**, 1404 (2016).

[66] J. V. Cady, O. Michel, K. W. Lee, R. N. Patel, C. J. Sarabalis, A. H. Safavi-Naeini, and A. C. Bleszynski Jayich, "Diamond optomechanical crystals with embedded nitrogen-vacancy centers," Quantum Science and Technology **4**, 024009 (2019).

[67] L. Fan, X. Sun, C. Xiong, C. Schuck, and H. X. Tang, "Aluminum nitride piezo-acousto-photonic crystal nanocavity with high quality factors," Applied Physics Letters **102**, 153507 (2013).

[68] R. Stockill, M. Forsch, G. Beaudoin, K. Pantzas, I. Sagnes, R. Braive, and S. Gröblacher, "Gallium phosphide as a piezoelectric platform for quantum optomechanics," Physical Review Letters **123**, 163602 (2019).

[69] K. Schneider, Y. Baumgartner, S. Hönl, P. Welter, H. Hahn, D. J. Wilson, L. Czornomaz, and P. Seidler, "Optomechanics with one-dimensional gallium phosphide photonic crystal cavities," Optica **6**, 577 (2019).

[70] M. Mirhosseini, A. Sipahigil, M. Kalaee, and O. Painter, "Quantum transduction of optical photons from a superconducting qubit," arXiv:2004.04838 (2020).

[71] *RefractiveIndex.info*, https://www.RefractiveIndex.info.

[72] *COMSOL Multiphysics®*, v. 5.4 (2018), https://www.comsol.com/, COMSOL AB, Stockholm, Sweden.

[73] J. S. Blakemore, "Semiconducting and other major properties of gallium arsenide," Journal of Applied Physics **53**, R123–R181 (1982).

[74] C.-L. Zou, X. Han, L. Jiang, and H. X. Tang, "Cavity piezomechanical strong coupling and frequency conversion on an aluminum nitride chip," Physical Review A **94**, 013812 (2016).

[75] R. S. Weis and T. K. Gaylord, "Lithium niobate: summary of physical properties and crystal structure," Applied Physics A Solids and Surfaces **37**, 191–203 (1985).

[76] C. Doolin, B. D. Hauer, P. H. Kim, A. J. R. MacDonald, H. Ramp, and J. P. Davis, "Nonlinear optomechanics in the stationary regime," Phys. Rev. A **89**, 053838 (2014).

[77] A. J. R. MacDonald, G. G. Popowich, B. D. Hauer, P. H. Kim, A. Fredrick, X. Rojas, P. Doolin, and J. P. Davis, "Optical microscope and tapered fiber coupling apparatus for a dilution refrigerator," Rev. Sci. Instrum. **86**, 013107 (2015).

[78] C. Doolin, "Integrated optical and mechanical resonators for evanescent field sensing," PhD thesis (University of Alberta, 2019).

[79] A. J. R. MacDonald, B. D. Hauer, X. Rojas, P. H. Kim, G. G. Popowich, and J. P. Davis, "Optomechanics and thermometry of cryogenic silica microresonators," Phys. Rev. A **93**, 013836 (2016).

[80] M. L. Gorodetksy, A. Schliesser, G. Anetsberger, S. Deleglise, and T. J. Kippenberg, "Determination of the vacuum optomechanical coupling rate using frequency noise calibration," Opt. Express **18**, 23236–23246 (2010).

[81] A. MacDonald, "Cryogenic Optomechanics with Silica Microresonators," Master's thesis (University of Alberta, 2015).

[82] Y. Hadjar, P. F. Cohadon, C. G. Aminoff, M. Pinard, and A. Heidmann, "High-sensitivity optical measurement of mechanical Brownian motion," Europhys. Lett. **47**, 545–551 (1999).

[83] A. Schliesser, G. Anetsberger, R. Rivière, O. Arcizet, and T. J. Kippenberg, "High-sensitivity monitoring of micromechanical vibration using optical whispering gallery mode resonators," New J. Phys. **10**, 095015 (2008).

[84] T. P. Purdy, K. E. Grutter, K. Srinivasan, and J. M. Taylor, "Quantum correlations from a room-temperature optomechanical cavity," Science **356**, 1265–1268 (2017).

[85] A. Abidi, "Direct-conversion radio transceivers for digital communications," in Proceedings ISSCC '95 - international solid-state circuits conference (1995).

[86] J. Crols and M. Steyaert, "A single-chip 900 MHz CMOS receiver front-end with a high performance low-IF topology," IEEE Journal of Solid-State Circuits **30**, 1483–1492 (1995).

[87] S. Mirabbasi and K. Martin, "Classical and modern receiver architectures," IEEE Communications Magazine **38**, 132–139 (2000).

[88] J. Glas, "Digital iq imbalance compensation in a low-IF receiver," in IEEE GLOBECOM 1998 (cat. NO. 98ch36250) ().

[89] B. D. Hauer, J. Maciejko, and J. P. Davis, "Nonlinear power spectral densities for the harmonic oscillator," Ann. Phys. **361**, 148–183 (2015).

[90] D. Damjanovic, "Ferroelectric, dielectric and piezoelectric properties of ferroelectric thin films and ceramics," Reports on Progress in Physics **61**, 1267–1324 (1998).

[91] J. Yang, *An introduction to the theory of piezoelectricity* (Springer, 2005).

[92] K.-y. Hasimoto, *Rf bulk acoustic wave filters for communications* (Artech Houes, 2009).

[93] M. de Jong, W. Chen, H. Geerlings, M. Asta, and K. A. Persson, "A database to enable discovery and design of piezoelectric materials," Scientific Data **2**, 150053 (2015).

[94] K. Hjort, J. Soderkvist, and J. .-A. Schweitz, "Gallium arsenide as a mechanical material," Journal of Micromechanics and Microengineering **4**, 1–13 (1994).

[95] N. C. Carvalho, J. Bourhill, M. Goryachev, S. Galliou, and M. E. Tobar, "Piezo-optomechanical coupling of a 3D microwave resonator to a bulk acoustic wave crystalline resonator," Applied Physics Letters **115**, 211102 (2019).

[96] M. Eichenfield, J. Chan, A. H. Safavi-Naeini, K. J. Vahala, and O. Painter, "Modeling dispersive coupling and losses of localized optical and mechanical modes in optomechanical crystals," Opt. Express **17**, 20078–20098 (2009).

[97] J. T. Hill, A. H. Safavi-Naeini, J. Chan, and O. Painter, "Coherent optical wavelength conversion via cavity optomechanics," Nat. Commun. **3**, 1196 (2012).

[98] X. Han, C. Xiong, K. Y. Fong, X. Zhang, and H. X. Tang, "Triply resonant cavity electro-optomechanics at x-band," New Journal of Physics **16**, 063060 (2014).

[99] M. Reagor, "Superconducting cavities for circuit quantum electrodynamics" (Yale University, 2015).

[100] S. C. Masmanidis, R. B. Karabalin, I. D. Vlaminck, G. Borghs, M. R. Freeman, and M. L. Roukes, "Multifunctional nanomechanical systems via tunably coupled piezoelectric actuation," Science **317**, 780–783 (2007).

[101] T. P. McKenna, R. N. Patel, J. D. Witmer, R. V. Laer, J. A. Valery, and A. H. Safavi-Naeini, "Cryogenic packaging of an optomechanical crystal," Optics Express **27**, 28782 (2019).

[102] M. Reagor, H. Paik, G. Catelani, L. Sun, C. Axline, E. Holland, I. M. Pop, N. A. Masluk, T. Brecht, L. Frunzio, M. H. Devoret, L. Glazman, and R. J. Schoelkopf, "Reaching 10ms single photon lifetimes for superconducting aluminum cavities," Applied Physics Letters **102**, 192604 (2013).

[103] M. Wu, E. Zeuthen, K. C. Balram, and K. Srinivasan, "Microwave-to-optical transduction using a mechanical supermode for coupling piezoelectric and optomechanical resonators," Physical Review Applied **13**, 014027 (2020).

[104] T. J. Clark, V. Vadakkumbatt, F. Souris, H. Ramp, and J. P. Davis, "Cryogenic microwave filter cavity with a tunability greater than 5 GHz," Review of Scientific Instruments **89**, 114704 (2018).

[105] C. W. Garland and K. C. Park, "Low-temperature elastic constants of gallium arsenide," Journal of Applied Physics **33**, 759–760 (1962).

[106] S. M. Meenehan, J. D. Cohen, S. Gröblacher, J. T. Hill, A. H. Safavi-Naeini, M. Aspelmeyer, and O. Painter, "Silicon optomechanical crystal resonator at millikelvin temperatures," Phys. Rev. A **90**, 011803 (2014).

[107] S. M. Meenehan, J. D. Cohen, G. S. MacCabe, F. Marsili, M. D. Shaw, and O. Painter, "Pulsed excitation dynamics of an optomechanical crystal resonator near its quantum ground state of motion," Phys. Rev. X **5**, 041002 (2015).

[108] B. D. Hauer, T. J. Clark, P. H. Kim, C. Doolin, and J. P. Davis, "Dueling dynamical backaction in a cryogenic optomechanical cavity," Phys. Rev. A **99**, 053803 (2019).

[109] "SciPy 1.0: fundamental algorithms for scientific computing in python," Nature Methods **17**, 261–272 (2020).

[110] B. Guha, F. Marsault, F. Cadiz, L. Morgenroth, V. Ulin, V. Berkovitz, A. Lemaitre, C. Gomez, A. Amo, S. Combrie, B. Gerard, G. Leo, and I. Favero, "Surface-enhanced gallium arsenide photonic resonator with quality factor of 6×10^6," Optica **4**, 218 (2017).

[111] C. P. Michael, M. Borselli, T. J. Johnson, C. Chrystal, and O. Painter, "An optical fiber-taper probe for wafer-scale microphotonic device characterization," Opt. Express **15**, 4745–4752 (2007).

[112] P. Rath, S. Khasminskaya, C. Nebel, C. Wild, and W. H. Pernice, "Diamond-integrated optomechanical circuits," Nature Communications **4**, 1690 (2013).

[113] M. Hamoumi, P. E. Allain, W. Hease, E. Gil-Santos, L. Morgenroth, B. Gérard, A. Lemaître, G. Leo, and I. Favero, "Microscopic nanomechanical dissipation in gallium arsenide resonators," Phys. Rev. Lett. **120**, 223601 (2018).

[114] D. T. Nguyen, C. Baker, W. Hease, S. Sejil, P. Senellart, A. Lemaitre, S. Ducci, G. Leo, and I. Favero, "Ultrahigh Q-frequency product for optomechanical disk resonators with a mechanical shield," Applied Physics Letters **103**, 241112 (2013).

[115] H. Ren, M. H. Matheny, G. S. MacCabe, J. Luo, H. Pfeifer, M. Mirhosseini, and O. Painter, "Two-dimensional optomechanical crystal cavity with high quantum cooperativity," Nature Communications **11**, 3373 (2020).

[116] S. Barzanjeh, S. Pirandola, D. Vitali, and J. M. Fink, "Microwave quantum illumination using a digital receiver," Science Advances **6**, eabb0451 (2020).

[117] K. F. Riley, M. P. Hobson, and S. J. Bence, *Mathematical methods for physics and engineering* (Cambridge University Press, Aug. 2002).

Appendix A

Phase Modulation of an Optical Field

The purpose of this Appendix is two-fold; first, we derive the equations that dictate how mechanical modulation affects the optical field inside of a cavity to demonstrate that optomechanical devices act as phase modulators. Second, we use the equation describing phase modulated light to describe and calibrate electro-optic phase modulators.

A.1   Mechanical Modulation of an Optical Cavity

The complete dynamic phase response due to mechanical motion can be found by solving the optical equation of motion Eqn. (2.32),

$$\dot{\hat{a}}(t) = -i\Delta\hat{a}(t) - ig_0\frac{\hat{x}}{x_{\mathrm{zpf}}}\hat{a}(t) - \frac{\kappa}{2}\hat{a}(t) - \sqrt{\kappa_{\mathrm{e}}}\hat{a}_{\mathrm{in}} \tag{A.1}$$

in the nonlinear regime, which rotates with the input laser frequency such that $\hat{a}_{\mathrm{in}}(t) = \hat{a}_{\mathrm{in}}$ is the constant laser input. Here we follow the work of Refs. [80] and [81].

The homogenous solution to the Eqn. (A.1) is found by considering the response when $\hat{a}_{\mathrm{in}} = 0$, such that

$$\dot{\hat{a}}_{\mathrm{h}}(t) = -\left(i\Delta + \frac{\kappa}{2} + ig_0\frac{x(t)}{x_{\mathrm{zpf}}}\right)\hat{a}_{\mathrm{h}}(t) \tag{A.2}$$

$$\Rightarrow \hat{a}_{\mathrm{h}}(t) = \hat{a}_0 e^{-(i\Delta+\frac{\kappa}{2})t - i\frac{g_0}{x_{\mathrm{zpf}}}\int x(t)dt}. \tag{A.3}$$

121

The complete response can be found by assuming a form

$$\hat{a}(t) = \hat{a}_{\mathrm{h}}(t)(1 + f(t)), \tag{A.4}$$

$$\Rightarrow \dot{\hat{a}}(t) = \dot{\hat{a}}_{\mathrm{h}}(t)(1 + f(t)) + \hat{a}_{\mathrm{h}}\dot{f}(t), \tag{A.5}$$

where $\hat{a}_{\mathrm{h}}(t)f(t)$ is the particular response. By comparing Eqn. (A.5) to Eqn. (A.1), we identify

$$\hat{a}_{\mathrm{h}}(t)\dot{f}(t) = \sqrt{\kappa_{\mathrm{e}}}\hat{a}_{\mathrm{in}}, \tag{A.6}$$

$$\Rightarrow \dot{f}(t) = \frac{\sqrt{\kappa_{\mathrm{e}}}\hat{a}_{\mathrm{in}}}{a_0} e^{(i\Delta + \frac{\kappa}{2})t + i\frac{g_0}{x_{\mathrm{zpf}}}\int x(t)dt}. \tag{A.7}$$

For our discussion we will restrict ourselves to a derivation where we consider simplified mechanics $x(t) = x_0 \cos(\omega_{\mathrm{m}}t)$, such that

$$\dot{f}(t) = \frac{\sqrt{\kappa_{\mathrm{e}}}\hat{a}_{\mathrm{in}}}{a_0} e^{(i\Delta + \frac{\kappa}{2})t + i\frac{g_0 x_0}{x_{\mathrm{zpf}}\omega_{\mathrm{m}}}\sin(\omega_{\mathrm{m}}t)}. \tag{A.8}$$

Here we can identify $\exp(i\beta_{\mathrm{m}}\sin(\omega_{\mathrm{m}}t))$ as a modulation of the optical phase, which has a mechanical modulation index

$$\beta_{\mathrm{m}} = \frac{g_0 x_0}{x_{\mathrm{zpf}}\omega_{\mathrm{m}}} \tag{A.9}$$

that describes the strength of the phase modulations. The next consideration is that for the specific case of mechanical motion the modulation index is typically small, which allows us to Taylor expand the exponential and integrate

$$\dot{f}(t) = \frac{\sqrt{\kappa_{\mathrm{e}}}\hat{a}_{\mathrm{in}}}{a_0} e^{(i\Delta + \frac{\kappa}{2})t} \left[1 + \frac{\beta_{\mathrm{m}}}{2}(e^{i\omega_{\mathrm{m}}t} - e^{-i\omega_{\mathrm{m}}t}) \right], \tag{A.10}$$

$$\Rightarrow f(t) = \frac{\sqrt{\kappa_{\mathrm{e}}}\hat{a}_{\mathrm{in}}}{a_0} e^{(i\Delta + \frac{\kappa}{2})t} \left[\frac{1}{i\Delta + \frac{\kappa}{2}} + \frac{\beta_{\mathrm{m}}}{2} \left(\frac{e^{i\omega_{\mathrm{m}}t}}{i(\Delta + \omega_{\mathrm{m}}) + \frac{\kappa}{2}} - \frac{e^{-i\omega_{\mathrm{m}}t}}{i(\Delta - \omega_{\mathrm{m}}) + \frac{\kappa}{2}} \right) \cdot \right] \tag{A.11}$$

The particular response can now be found by making the same approximations for $\hat{a}_{\mathrm{h}}(t)$, to find

$$\hat{a}_{\mathrm{h}}(t)f(t) = \sqrt{\kappa_{\mathrm{e}}}\hat{a}_{\mathrm{in}} \left[1 - \frac{\beta_{\mathrm{m}}}{2} \left(e^{i\omega_{\mathrm{m}}t} - e^{-i\omega_{\mathrm{m}}t} \right) \right]$$
$$\left[\frac{1}{i\Delta + \frac{\kappa}{2}} + \frac{\beta_{\mathrm{m}}}{2} \left(\frac{e^{i\omega_{\mathrm{m}}t}}{i(\Delta + \omega_{\mathrm{m}}) + \frac{\kappa}{2}} - \frac{e^{-i\omega_{\mathrm{m}}t}}{i(\Delta - \omega_{\mathrm{m}}) + \frac{\kappa}{2}} \right) \right]. \tag{A.12}$$

By assumning β_m^2 is small enough to be neglected and that $f(t) \gg 1$, the cavity field is

$$\hat{a}(t) = \frac{\sqrt{\kappa_e}\hat{a}_{in}}{i\Delta + \frac{\kappa}{2}} \left[1 + \frac{\beta_m}{2} \left(\frac{-i\omega_m e^{i\omega_m t}}{i(\Delta + \omega_m) + \frac{\kappa}{2}} - \frac{i\omega_m e^{-i\omega_m t}}{i(\Delta - \omega_m) + \frac{\kappa}{2}} \right) \right]. \tag{A.13}$$

When the laser is tuned to cavity frequency such that $\Delta = 0$, and if the optomechanical crystal is close to the sideband resolved regime where $\omega_m \gtrsim \kappa/2$, the cavity field can be simplified to

$$\hat{a}(t) = \hat{a} \left[1 - \frac{\beta_m}{2}(e^{i\omega_m t} - e^{-i\omega_m t}) \right], \tag{A.14}$$

which includes the previously derived steady-state response at the laser frequency and two mechanical sidebands spaced by $\pm\omega_m$. Note that we have returned to the form that we obtained using the Taylor expansion, which suggests that a more complete description of the mechanically phase modulated optical field in the cavity is

$$\hat{a}(t) = \hat{a} e^{-i\beta_m \sin(\omega_m t)}. \tag{A.15}$$

A.2 Electro-optic Phase Modulators

Phase modulating the laser source to create sidebands is useful for both heterodyne detection of mechanical modes and for phase calibration of the optomechanical coupling. For laser input $\hat{a}_{in}$ in the rotating frame, an electro-optic phase modulator (EOM) contributes time dependent phase modulation $\phi(t) = \beta_{EOM} \sin(\omega_{EOM} t)$ such that,

$$\hat{a}_{in}(t) = \hat{a}_{in} e^{-i\beta_{EOM}\sin(\omega_{EOM}t)}, \tag{A.16}$$

which represents an EOM driven at frequency ω_{EOM}. The electro-optic modulation index $\beta_{EOM} = \frac{\pi V_{EOM}}{V_\pi}$ represents the strength of modulation, which is determined by the ratio of the voltage applied to the EOM V_{EOM} to the half-wave voltage V_π, which is the voltage necessary to phase shift the light by π.

The Taylor expansion applied in Eqn. (A.10) requires that the modulation index is small, which is generally true for mechanical modulation, but not necessarily

the case for EOMs, which can be driven with strong microwave sources. For large β_{EOM} we consider the Jacobi-Anger expansion in terms of Bessel functions [117]

$$e^{-i\beta_{\mathrm{EOM}}\sin(\omega_{\mathrm{EOM}}t)} = -\sum_{n=-\infty}^{\infty} J_n(\beta_{\mathrm{EOM}})e^{in\omega_{\mathrm{EOM}}t}. \tag{A.17}$$

Expanding the sums for $n = 0, \pm 1$, the modulated laser field to first order is

$$\hat{a}_{\mathrm{EOM}}(t) \approx \hat{a}_{\mathrm{in}}\left(J_0(\beta_{\mathrm{EOM}}) - (J_1(\beta_{\mathrm{EOM}})e^{i\omega_{\mathrm{EOM}}t} + J_{-1}(\beta_{\mathrm{EOM}})e^{-i\omega_{\mathrm{EOM}}t})\right), \tag{A.18}$$

where $J_0(\beta_{\mathrm{EOM}})$ is the amplitude of the carrier and $J_1(\beta_{\mathrm{EOM}}) = -J_{-1}(\beta_{\mathrm{EOM}})$ are the amplitudes of the first sidebands generated by the EOM.
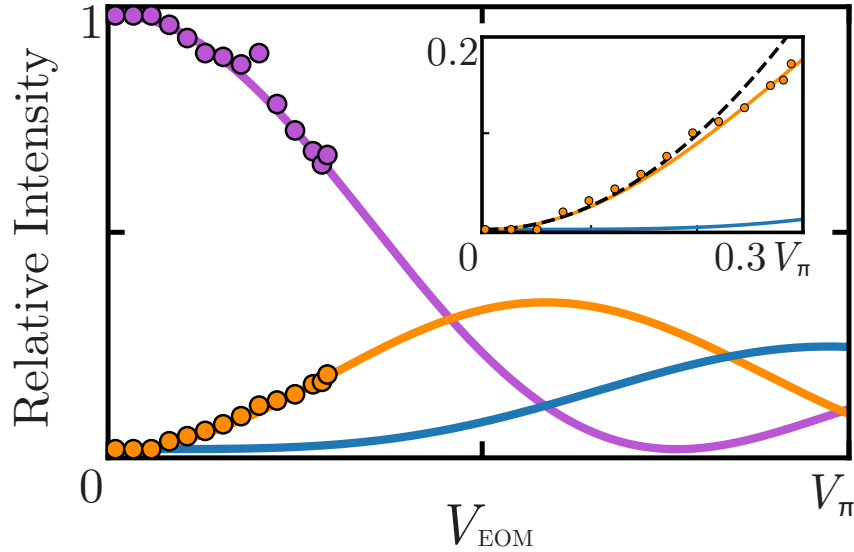
Figure A.1: Calibration of an electro-optic phase modulator. The amplitudes of the carrier (purple markers) and first sideband (orange markers) are measured relative to the carrier amplitude in absence of modulation ($V_{\mathrm{EOM}} = 0$) for voltage inputs in the range $V_{\mathrm{EOM}} = (0, 1.1)$ V. The data is fit to the relative intensity of the carrier (purple) and first sideband (orange). The calculated relative intensity of the second order sideband is also plotted (blue). The inset shows a close-up for small applied voltages, where the relative amplitude of the first sideband is compared to the small-voltage approximation $|\beta_{\mathrm{EOM}}/2|^2$ (black dashed).

Measuring V_π of an EOM can be achieved using a tunable Fabry Pérot cavity[1] with narrow linewidth (≈ 5 MHz). The power transmitted through the cavity is monitored as the cavity resonance frequency is swept across the laser frequency.

---

[1]Micron Optics FFP-SI scanning interferometer

The maximum transmission measured for $V_{\mathrm{EOM}} < 0.4V_\pi$ represents the amplitude of the carrier, while the next largest peaks on either side of the carrier represent the amplitudes of the first order modulation sidebands. Using the unmodulated signal amplitude as a reference, the relative intensities of the spectral components can be measured as β_{EOM} is varied by changing the voltage applied to the EOM.

In Fig. A.1, the carrier and sideband amplitudes relative to the unmodulated signal amplitude are measured for applied voltages between 0 V and 1.1 V at $\omega_{\mathrm{EOM}} = 2.35$ GHz. The relative intensities of the carrier and first sideband are fit to

$$\left| \frac{J_0(\beta_{\mathrm{EOM}})}{J_0(0)} \right|^2, \tag{A.19}$$

$$\left| \frac{J_1(\beta_{\mathrm{EOM}})}{J_0(0)} \right|^2, \tag{A.20}$$

respectively to extract V_π. The voltages are then scaled to units of V_π and the calculated relative intensities of the carrier and first two sidebands are plotted for applied voltages up to V_π. The inset comparison between Eqn. (A.19) and $|\beta_{\mathrm{EOM}}/2|^2$ suggests that the Taylor expansion approximation is good for voltages up to $0.1V_\pi$. From the fits, we find $V_\pi = 4.1$ V for the EOM used for phase calibration in our experiments.

A.3   Phase Modulation & Mechanics

We now consider the case of a phase-modulated signal being used to measure the mechanical motion, which is the case during phase calibration experiments. Because the voltage used for phase calibration is small $V_{\mathrm{CAL}} \ll V_\pi$, we use the Taylor expansion of Eqn. (A.16) to describe the optical input field in the equation of motion, Eqn. (A.5). In this scenario, the solution to the homogeneous equation remains the same, but the remainder of the equation becomes more complicated,

$$\hat{a}_{\mathrm{h}}(t)\dot{f}(t) = \sqrt{\kappa_{\mathrm{e}}}\hat{a}_{\mathrm{in}} \left[1 - \frac{\beta_{\mathrm{EOM}}}{2} \left(e^{i\omega_{\mathrm{EOM}}t} - e^{-i\omega_{\mathrm{EOM}}t} \right) \right], \tag{A.21}$$

such that

$$\dot{f}(t) = \frac{\sqrt{\kappa_{\mathrm{e}}}\hat{a}_{\mathrm{in}}}{a_0} e^{(i\Delta + \frac{\kappa}{2})t} \left[1 - \frac{\beta_{\mathrm{EOM}}}{2} \left(e^{i\omega_{\mathrm{EOM}}t} - e^{-i\omega_{\mathrm{EOM}}t} \right) \right] \left[1 + \frac{\beta_{\mathrm{m}}}{2} \left(e^{i\omega_{\mathrm{m}}t} - e^{-i\omega_{\mathrm{m}}t} \right) \right]. \tag{A.22}$$

The particular response can then be found by integrating Eqn. (A.22) and calculating

$$\hat{a}_{\mathrm{h}}f(t) \approx \sqrt{\kappa_{\mathrm{e}}}\hat{a}_{\mathrm{in}}\left[\frac{1}{i\Delta + \frac{\kappa}{2}} - \frac{\beta_{\mathrm{EOM}}}{2}\left(\frac{e^{i\omega_{\mathrm{EOM}}t}}{i(\Delta + \omega_{\mathrm{EOM}}) + \frac{\kappa}{2}} - \frac{e^{-i\omega_{\mathrm{EOM}}t}}{i(\Delta - \omega_{\mathrm{EOM}}) + \frac{\kappa}{2}}\right)\right.$$
$$+ \frac{\beta_{\mathrm{m}}}{2}\left(\frac{e^{i\omega_{\mathrm{m}}t}}{i(\Delta + \omega_{\mathrm{m}}) + \frac{\kappa}{2}} - \frac{e^{-i\omega_{\mathrm{m}}t}}{i(\Delta - \omega_{\mathrm{m}}) + \frac{\kappa}{2}}\right)$$
$$\left. - \frac{\beta_{\mathrm{m}}}{2}\left(\frac{e^{i\omega_{\mathrm{m}}t}}{i\Delta + \frac{\kappa}{2}} - \frac{e^{-i\omega_{\mathrm{m}}t}}{i\Delta + \frac{\kappa}{2}}\right)\right], \tag{A.23}$$

where we have ignored terms of size less than β^2. This equation, which we recognise as the cavity optical field with phase and mechanical modulation, can then be further simplified

$$\hat{a}(t) = \sqrt{\kappa_{\mathrm{e}}}\hat{a}_{\mathrm{in}}\left[\frac{1}{i\Delta + \frac{\kappa}{2}} - \frac{\beta_{\mathrm{EOM}}}{2}\left(\frac{e^{i\omega_{\mathrm{EOM}}t}}{i(\Delta + \omega_{\mathrm{EOM}}) + \frac{\kappa}{2}} - \frac{e^{-i\omega_{\mathrm{EOM}}t}}{i(\Delta - \omega_{\mathrm{EOM}}) + \frac{\kappa}{2}}\right)\right.$$
$$\left. - \frac{i\omega_{\mathrm{m}}\beta_{\mathrm{m}}}{2(i\Delta + \frac{\kappa}{2})}\left(\frac{e^{i\omega_{\mathrm{m}}t}}{i(\Delta + \omega_{\mathrm{m}}) + \frac{\kappa}{2}} + \frac{e^{-i\omega_{\mathrm{m}}t}}{i(\Delta - \omega_{\mathrm{m}}) + \frac{\kappa}{2}}\right)\right]. \tag{A.24}$$

We now recall that optical field after the cavity is described by

$$\hat{a}_{\mathrm{out}}(t) = \hat{a}_{\mathrm{in}}(t) + \frac{\sqrt{\kappa_{\mathrm{e}}}}{2}\hat{a}(t), \tag{A.25}$$

which becomes

$$\hat{a}_{\mathrm{out}}(t) = \hat{a}_{\mathrm{in}}\left(1 + \frac{\beta_{\mathrm{EOM}}}{2}(e^{i\omega_{\mathrm{EOM}}t} - e^{-i\omega_{\mathrm{EOM}}t})\right)$$
$$+ \frac{\kappa_{\mathrm{e}}}{2}\hat{a}_{\mathrm{in}}\left[\frac{1}{i\Delta + \frac{\kappa}{2}} - \frac{\beta_{\mathrm{EOM}}}{2}\left(\frac{e^{i\omega_{\mathrm{EOM}}t}}{i(\Delta + \omega_{\mathrm{EOM}}) + \frac{\kappa}{2}} - \frac{e^{-i\omega_{\mathrm{EOM}}t}}{i(\Delta - \omega_{\mathrm{EOM}}) + \frac{\kappa}{2}}\right)\right.$$
$$\left. - \frac{i\omega_{\mathrm{m}}\beta_{\mathrm{m}}}{2(i\Delta + \frac{\kappa}{2})}\left(\frac{e^{i\omega_{\mathrm{m}}t}}{i(\Delta + \omega_{\mathrm{m}}) + \frac{\kappa}{2}} + \frac{e^{-i\omega_{\mathrm{m}}t}}{i(\Delta - \omega_{\mathrm{m}}) + \frac{\kappa}{2}}\right)\right]. \tag{A.26}$$

We now consider direct detection, where the high-frequency component of the optical intensity measured on the photodetector is

$$|\hat{a}_{\mathrm{out}}(t)|^2_{\mathrm{AC}} = \frac{|\hat{a}_{\mathrm{in}}|^2\kappa_{\mathrm{e}}}{2}\left(\beta_{\mathrm{m}}\mathcal{K}(\Delta, \omega_{\mathrm{m}})\frac{x(t)}{x_0} - \beta_{\mathrm{EOM}}\mathcal{K}(\Delta, \omega_{\mathrm{EOM}})\phi(t)\right), \tag{A.27}$$

where $\mathcal{K}(\Delta, \omega)$ describes the detuning and frequency dependence of the transmitted field. If $\omega_{\mathrm{EOM}} \approx \omega_{\mathrm{m}}$, then at any particular detuning the ratio of the signal intensities should depend on the ratio of modulation indices.

126

Appendix B

Low-IF Receiver

This Appendix details the implementation of a low-IF receiver which digitally compensates for imbalances in the analog IQ mixer. The methodology described here closely follows the work of Ref. [88], and was implemented as a python script for the purposes of measuring the phase of the microwave-to-telecom transduced signal. Using this implementation, we were able to demonstrate phase coherence, but the accuracy of the phase measurement was limited by phase digitization errors that came from a low-frequency clock input. Using this implementation of a low-IF receiver with an analog-to-digital converter which has an extra high-speed channel that can be used as a clock will allow for the rapid acquisition of high-quality phase data for future experiments.
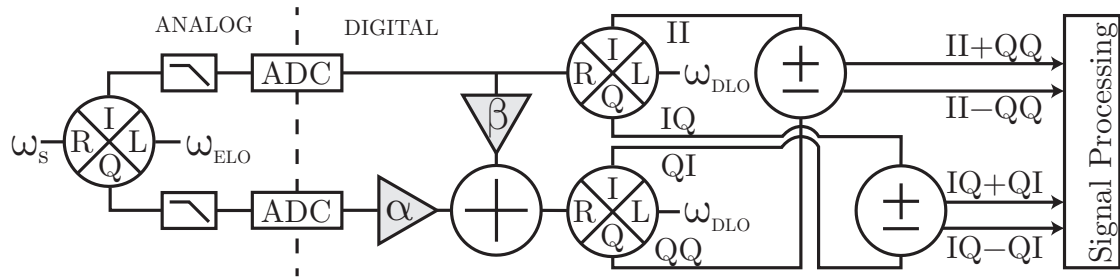

Figure B.1:   Low-IF receiver with compensation for phase and amplitude imbalances.

The implementation of a low-IF receiver with digital compensation is illustrated in Fig. B.1. Imbalances in the IQ mixer can be modelled by introducing phase and

amplitude offsets Δ and θ respectively to the electronic local oscillator,

$$\text{ELO}_\text{I} = (1 + \Delta)\cos(\omega_\text{ELO}t + \theta), \tag{B.1}$$

$$\text{ELO}_\text{Q} = (1 - \Delta)\sin(\omega_\text{ELO}t - \theta). \tag{B.2}$$

These offsets are compensated for digitally by assuming the I quadrature has the correct amplitude and phase. The Q quadrature is then corrected using amplitude compensation α and phase compensation β. Determining these compensation factors requires a pilot tone which is used to measure the imbalances. We will consider the pilot tone $A\cos(\omega_\text{s}t + \phi)$, which is mixed with the local oscillator and subsequently low-pass filtered. The pilot I and Q signals measured on the analog-to-digital converter are

$$\text{I} = +\frac{A(1+\Delta)}{2}\cos((\omega_\text{s} - \omega_\text{ELO})t + \phi - \theta), \tag{B.3}$$

$$\text{Q} = -\frac{A(1-\Delta)}{2}\sin((\omega_\text{s} - \omega_\text{ELO})t + \phi + \theta). \tag{B.4}$$

The signal is now at the intermittent frequency $\omega_\text{IF} = \omega_\text{s} - \omega_\text{ELO}$. To digitally mix it down to DC, a digital local oscillator at frequency $\omega_\text{DLO} = \omega_\text{IF}$ is created and mixed with both of the measured signals to produce a set of four signals:

$$\text{II} = +\frac{A(1+\Delta)}{4}[\cos(\phi - \theta) + \cos(2\omega_\text{IF}t + \phi - \theta], \tag{B.5}$$

$$\text{IQ} = -\frac{A(1+\Delta)}{4}[\sin(\phi - \theta) - \sin(2\omega_\text{IF}t + \phi - \theta], \tag{B.6}$$

$$\text{QI} = -\frac{A(1-\Delta)}{4}[\sin(\phi + \theta) + \sin(2\omega_\text{IF}t + \phi + \theta], \tag{B.7}$$

$$\text{QQ} = -\frac{A(1-\Delta)}{4}[\cos(\phi + \theta) + \cos(2\omega_\text{IF}t + \phi + \theta]. \tag{B.8}$$

Using these, we calculate the DC signal in-phase and quadrature components as well as their images,

$$\text{I}_2 = \text{II} - \text{QQ} = \frac{A}{2}[\cos(\theta)\cos(\phi) + \Delta\sin(\theta)\sin(\phi)], \tag{B.9}$$

$$\text{Q}_2 = \text{IQ} + \text{QI} = \frac{A}{2}[\Delta\sin(\theta)\cos(\phi) - \cos(\theta)\sin(\phi)], \tag{B.10}$$

$$\text{I}_{2i} = \text{II} + \text{QQ} = \frac{A}{2}[\Delta\cos(\theta)\cos(\phi) + \sin(\theta)\sin(\phi)], \tag{B.11}$$

$$\text{Q}_{2i} = \text{IQ} - \text{QI} = \frac{A}{2}[\sin(\theta)\cos(\phi) - \Delta\cos(\theta)\sin(\phi)], \tag{B.12}$$

which in turn can be used to find the amplitude and phase offsets,

$$\Delta = \frac{I_2 I_{2i} + Q_2 Q_{2i}}{I_2^2 + Q_2^2}, \tag{B.13}$$

$$\theta = \frac{I_2 Q_{2i} + I_{2i} Q_2}{I_2^2 + Q_2^2}. \tag{B.14}$$

We now use our knowledge of the IQ mixer imbalances to determine correction factors for amplitude and phase,

$$\alpha = \frac{1}{(1 - \Delta)\cos(\theta)}, \tag{B.15}$$

$$\beta = -\tan(\theta). \tag{B.16}$$

If we consider an experimental signal which we wish to be accurately measured, we can, without loss of generality, shift the IQ imbalance errors into the quadrature signal, such that the signal measured on the analog-to-digital converter is

$$I = \frac{A}{2}\cos(\omega_{IF} t + \phi), \tag{B.17}$$

$$Q = \frac{A(1 - 2\Delta)}{2}\sin(\omega_{IF} t + \phi + 2\theta). \tag{B.18}$$

We can apply our calibration by transforming the signals such that

$$I \to I = +\frac{A}{2}\cos((\omega_s - \omega_{ELO})t + \phi), \tag{B.19}$$

$$Q \to \beta I + \alpha Q = -\frac{A}{2}\sin((\omega_s - \omega_{ELO})t + \phi), \tag{B.20}$$

which is the output of an ideal IQ mixer. Thus, using this algorithm, we can digitally compensate for amplitude and phase imbalances in the analog IQ mixer. The balanced quadratures can then be digitally downmixed to DC, with quadratures derived from Eqns. (B.9-B.10) where $\Delta = \theta = 0$, such that

$$I_2 = +\cos(\phi), \tag{B.21}$$

$$Q_2 = -\sin(\phi). \tag{B.22}$$

Rewriting the equation to solve for the signal phase, we recover Eqn. (3.26):

$$\phi = -\arctan\left(\frac{Q_2}{I_2}\right) \tag{B.23}$$

Appendix C

Microwave to Mechanical Transduction

The Appendix contains a detailed derivation of Eqn. 4.24, the relation between microwave input power and the number of microwave-actuated phonons in the mechanical mode.

To begin the derivation, recall the piezomechanical Hamiltonian derived in Section 4.3, Eqn. 4.15, where the operators are implicitly time dependent:

$$\mathcal{H}_{\mathrm{pm}} = \hbar\omega_{\mathrm{m}}\hat{b}^{\dagger}\hat{b} + \hbar\omega_{\mu}\hat{c}^{\dagger}\hat{c} + \hbar g_{\mu}(\hat{c}^{\dagger} + \hat{c})(\hat{b}^{\dagger} + \hat{b}), \tag{C.1}$$

which represents harmonic oscillators coupled by the piezomechanical interaction g_{μ}. The equations of motions are derived from the Hamiltonian using the Heisenberg equation [32]

$$\dot{\hat{O}} = \frac{i}{\hbar}\left[\mathcal{H}, \hat{O}\right]. \tag{C.2}$$

For the mechanical mode, the explicit derivation makes use of the identity $\left[\hat{b}^{\dagger}, \hat{b}\right] = -1$, such that

$$\dot{\hat{b}} = \frac{i}{\hbar}\left[\mathcal{H}, \hat{b}\right] \tag{C.3}$$

$$\dot{\hat{b}} = i\omega_{\mathrm{m}}\left[\hat{b}^{\dagger}, \hat{b}\right]\hat{b} + ig_{\mu}\left(\hat{c}^{\dagger} + \hat{c}\right)\left[\hat{b}^{\dagger}, \hat{b}\right] \tag{C.4}$$

$$\dot{\hat{b}} = -i\omega_{\mathrm{m}}\hat{b} - ig_{\mu}\left(\hat{c}^{\dagger} + \hat{c}\right). \tag{C.5}$$

To add coupling to the external environment, terms from input-output theory [33, 89] are added to account for mechanical damping and thermal noise input,

$$\dot{\hat{b}} = i\omega_{\mathrm{m}}\hat{b} + ig_{\mu}\left(\hat{c}^{\dagger} + \hat{c}\right) + i\frac{\Gamma_{\mathrm{m}}}{2}\hat{b} + \sqrt{\Gamma_{\mathrm{m}}}\hat{b}_{\mathrm{in}}. \tag{C.6}$$

Similarly, the equation of motion for the microwave mode is:

$$\dot{\hat{c}} = i\omega_\mu \hat{c} + ig_\mu \left(\hat{b}^\dagger + \hat{b} \right) + i\frac{\kappa_\mu}{2}\hat{c} + \sqrt{\kappa_{\mu,e}}\hat{c}_{in}, \tag{C.7}$$

where $\hat{c}_{in}$ is the microwave input, and κ_μ and $\kappa_{\mu,e}$ are the total and external microwave cavity damping rates respectively. The equations of motion are transformed into the frequency domain using the Fourier transform $\hat{O}(\omega) = \int_{-\infty}^{\infty} e^{-i\omega t}\hat{O}(t)dt$,

$$i\omega\hat{b}(\omega) = (i\omega_m + \frac{\Gamma_m}{2})\hat{b}(\omega) + ig_\mu(\hat{c}^\dagger(\omega) + \hat{c}(\omega)) + \sqrt{\Gamma_m}\hat{b}_{in}(\omega) \tag{C.8}$$

$$i\omega\hat{c}(\omega) = (i\omega_\mu + \frac{\kappa_\mu}{2})\hat{c}(\omega) + g_\mu(\hat{b}^\dagger(\omega) + \hat{b}(\omega)) + \sqrt{\kappa_{\mu,e}}\hat{c}_{in}(\omega). \tag{C.9}$$

Next, we make the simplifying assumption of unidirectional microwave to mechanical transduction, which implies the microwave cavity is predominantly populated with photons from a strong microwave input signal $\hat{c}_{in}$ and that the piezomechanical coupling term can therefore be eliminated:

$$i\omega\hat{c}(\omega) = (i\omega_\mu + \frac{\kappa_\mu}{2})\hat{c}(\omega) + \sqrt{\kappa_{\mu,e}}\hat{c}_{in}(\omega). \tag{C.10}$$

From here, the equations of motion are solved for their respective boson operators

$$\hat{b}(\omega) = -\frac{ig_\mu \left(\hat{c}^\dagger(\omega) + \hat{c}(\omega) \right) + \sqrt{\Gamma_m}\hat{b}_{in}(\omega)}{\chi_b^{-1}(\omega)} \tag{C.11}$$

$$\hat{c}(\omega) = -\frac{\sqrt{\kappa_{\mu,e}}\hat{c}_{in}(\omega)}{\chi_c^{-1}(\omega)}, \tag{C.12}$$

where the inverse susceptibilities are defined as

$$\chi_b^{-1}(\omega) = i\left(\omega_m - \omega \right) + \Gamma_m/2, \tag{C.13}$$

$$\chi_c^{-1}(\omega) = i\left(\omega_\mu - \omega \right) + \kappa_\mu/2. \tag{C.14}$$

Similarly the conjugate operators are found using the relation $(\hat{O}^\dagger)(\omega) = \left[\hat{O}(-\omega) \right]^\dagger$:

$$\hat{b}^\dagger(\omega) = -\frac{-ig_\mu \left(\hat{c}(\omega) + \hat{c}^\dagger(\omega) \right) + \sqrt{\Gamma_m}\hat{b}_{in}^\dagger(\omega)}{[\chi_b^{-1}(-\omega)]^*} \tag{C.15}$$

$$\hat{c}^\dagger(\omega) = -\frac{\sqrt{\kappa_{\mu,e}}\hat{c}_{in}^\dagger(\omega)}{[\chi_c^{-1}(-\omega)]^*}, \tag{C.16}$$

Replacing $\hat{c}^\dagger(\omega)$, $\hat{c}(\omega)$ in Eqns. (C.11,C.15) with Eqns. (C.12,C.16), the mechanical mode is described in terms of microwave-actuated phonons from the microwave drive $\hat{c}_{\text{in}}(\omega)$ and thermal phonons $\hat{b}_{\text{in}}(\omega)$,

$$\hat{b}(\omega) = \frac{-ig_\mu}{\chi_{\text{b}}^{-1}(\omega)} \left[\frac{-\sqrt{\kappa_{\mu,\text{e}}}\hat{c}_{\text{in}}^\dagger(\omega)}{[\chi_{\text{c}}^{-1}(-\omega)]^*} + \frac{-\sqrt{\kappa_{\mu,\text{e}}}\hat{c}_{\text{in}}(\omega)}{\chi_{\text{c}}^{-1}(\omega)} \right] - \frac{\sqrt{\Gamma_{\text{m}}}\hat{b}_{\text{in}}(\omega)}{\chi_{\text{b}}^{-1}(\omega)} \tag{C.17}$$

$$\hat{b}^\dagger(\omega) = \frac{ig_\mu}{[\chi_{\text{b}}^{-1}(-\omega)]^*} \left[\frac{-\sqrt{\kappa_{\mu,\text{e}}}\hat{c}_{\text{in}}^\dagger(\omega)}{[\chi_{\text{c}}^{-1}(-\omega)]^*} + \frac{-\sqrt{\kappa_{\mu,\text{e}}}\hat{c}_{\text{in}}(\omega)}{\chi_{\text{c}}^{-1}(\omega)} \right] - \frac{\sqrt{\Gamma_{\text{m}}}\hat{b}_{\text{in}}^\dagger(\omega)}{[\chi_{\text{b}}^{-1}(-\omega)]^*}. \tag{C.18}$$

The power spectral density function associated with the negative-frequency sideband of the microwave-driven mechanical mode is given by [89]

$$S_{\hat{b}^\dagger\hat{b}}(\omega) = \frac{1}{2\pi} \int \langle \hat{b}^\dagger(\omega)\hat{b}(\omega') \rangle \, d\omega'. \tag{C.19}$$

The spectral density can be split into two components: microwave driven and thermal. The thermal power spectral density is well known, and can be obtained using the correlator [33, 89]

$$\langle \hat{b}_{\text{in}}^\dagger(\omega)\hat{b}_{\text{in}}(\omega') \rangle = 2\pi\bar{n}_{\text{b}}(\omega_{\text{m}})\delta(\omega + \omega'), \tag{C.20}$$

where $\delta(\omega + \omega')$ is the Dirac delta function. The thermal power spectral density is then

$$S_{b^\dagger b}^{\text{th}}(\omega) = \frac{\Gamma_{\text{m}}n_{\text{b}}(\omega_{\text{m}})}{(\omega_{\text{m}} + \omega)^2 + \Gamma_{\text{m}}^2/4}. \tag{C.21}$$

To determine the power spectral density of the microwave-actuated phonons, we must first develop similar correlators for $\hat{c}_{\text{in}}(\omega)$. To do this, we begin by defining the input signal itself,

$$\hat{c}_{\text{in}}(t) = \bar{c}_{\text{in}}e^{i\omega_{\text{s}}t}.$$

By Fourier transforming the input signal, we find the the frequency-space annihilation and creation operators for the microwave input to be

$$\hat{c}_{\text{in}}(\omega) = 2\pi\bar{c}_{\text{in}}\delta(\omega - \omega_{\text{s}}), \tag{C.22}$$

$$\hat{c}_{\text{in}}^\dagger(\omega) = 2\pi\bar{c}_{\text{in}}^*\delta(\omega + \omega_{\text{s}}). \tag{C.23}$$

Hence, we can write a complete set of noise correlators for the microwave input:

$$\langle \hat{c}_{in}^\dagger(\omega)\hat{c}_{in}(\omega')\rangle = (2\pi)^2 \, |\bar{c}_{in}|^2 \, \delta(\omega + \omega_s)\delta(\omega' - \omega_s) \tag{C.24}$$

$$\langle \hat{c}_{in}(\omega)\hat{c}_{in}^\dagger(\omega')\rangle = (2\pi)^2 \, |\bar{c}_{in}|^2 \, \delta(\omega - \omega_s)\delta(\omega' + \omega_s) \tag{C.25}$$

$$\langle \hat{c}_{in}(\omega)\hat{c}_{in}(\omega')\rangle = (2\pi)^2 \, (\bar{c}_{in})^2 \, \delta(\omega - \omega_s)\delta(\omega' - \omega_s) \tag{C.26}$$

$$\langle \hat{c}_{in}^\dagger(\omega)\hat{c}_{in}^\dagger(\omega')\rangle = (2\pi)^2 \, (\bar{c}_{in}^*)^2 \, \delta(\omega + \omega_s)\delta(\omega' + \omega_s). \tag{C.27}$$

Note that there is no correlation between the microwave input signal and mechanical thermal noise, and thus the correlator of cross terms is zero. This allows us to write the spectral density function of the microwave-actuated component of the mechanical mode,

$$S_{\hat{b}^\dagger\hat{b}}^s(\omega) = \frac{g_\mu^2 \kappa_{\mu,e}}{2\pi} \int d\omega' \Bigg[\frac{\langle \hat{c}_{in}^\dagger(\omega)\hat{c}_{in}(\omega')\rangle}{[\chi_c^{-1}(-\omega)]^*[\chi_b^{-1}(-\omega)]^*\chi_c^{-1}(\omega')\chi_b^{-1}(\omega')}$$
$$+ \frac{\langle \hat{c}_{in}(\omega)\hat{c}_{in}^\dagger(\omega')\rangle}{\chi_c^{-1}(\omega)[\chi_b^{-1}(-\omega)]^*[\chi_c^{-1}(-\omega')]^*\chi_b^{-1}(\omega')}$$
$$+ \frac{\langle \hat{c}_{in}(\omega)\hat{c}_{in}(\omega')\rangle}{\chi_c^{-1}(\omega)[\chi_b^{-1}(-\omega)]^*\chi_c^{-1}(\omega')\chi_b^{-1}(\omega')}$$
$$+ \frac{\langle \hat{c}_{in}^\dagger(\omega)\hat{c}_{in}^\dagger(\omega')\rangle}{[\chi_c^{-1}(-\omega)]^*[\chi_b^{-1}(-\omega)]^*[\chi_c^{-1}(-\omega')]^*\chi_b^{-1}(\omega')} \Bigg]. \tag{C.28}$$

Then, replacing the correlators,

$$S_{\hat{b}^\dagger\hat{b}}^s(\omega) = 2\pi g_\mu^2 \kappa_{\mu,e} \int d\omega' \Bigg[\frac{(2\pi)^2 \, |\bar{c}_{in}|^2 \, \delta(\omega + \omega_s)\delta(\omega' - \omega_s)}{[\chi_c^{-1}(-\omega)]^*[\chi_b^{-1}(-\omega)]^*\chi_c^{-1}(\omega')\chi_b^{-1}(\omega')}$$
$$+ \frac{(2\pi)^2 \, |\bar{c}_{in}|^2 \, \delta(\omega - \omega_s)\delta(\omega' + \omega_s)}{\chi_c^{-1}(\omega)[\chi_b^{-1}(-\omega)]^*[\chi_c^{-1}(-\omega')]^*\chi_b^{-1}(\omega')}$$
$$+ \frac{(2\pi)^2 \, (\bar{c}_{in})^2 \, \delta(\omega - \omega_s)\delta(\omega' - \omega_s)}{\chi_c^{-1}(\omega)[\chi_b^{-1}(-\omega)]^*\chi_c^{-1}(\omega')\chi_b^{-1}(\omega')}$$
$$+ \frac{(2\pi)^2 \, (\bar{c}_{in}^*)^2 \, \delta(\omega + \omega_s)\delta(\omega' + \omega_s)}{[\chi_c^{-1}(-\omega)]^*[\chi_b^{-1}(-\omega)]^*[\chi_c^{-1}(-\omega')]^*\chi_b^{-1}(\omega')} \Bigg]. \tag{C.29}$$

The integral over the delta function has the affect of setting $\omega' \to \pm\omega_s$, the resulting

function is the power spectral density of the microwave-actuated phonons:

$$S_{\hat{b}^\dagger\hat{b}}^s(\omega) = g_\mu^2 \kappa_{\mu,e} \left[\frac{(2\pi)\,|\bar{c}_{in}|^2\,\delta(\omega+\omega_s)}{[\chi_c^{-1}(-\omega)]^*[\chi_b^{-1}(-\omega)]^*\chi_c^{-1}(\omega_s)\chi_b^{-1}(\omega_s)} \right.$$
$$+ \frac{(2\pi)\,|\bar{c}_{in}|^2\,\delta(\omega-\omega_s)}{\chi_c^{-1}(\omega)[\chi_b^{-1}(-\omega)]^*[\chi_c^{-1}(\omega_s)]^*\chi_b^{-1}(-\omega_s)}$$
$$+ \frac{(2\pi)\,(\bar{c}_{in})^2\,\delta(\omega-\omega_s)}{\chi_c^{-1}(\omega)[\chi_b^{-1}(-\omega)]^*\chi_c^{-1}(\omega_s)\chi_b^{-1}(\omega_s)}$$
$$\left. + \frac{(2\pi)\,(\bar{c}_{in}^*)^2\,\delta(\omega+\omega_s)}{[\chi_c^{-1}(-\omega)]^*[\chi_b^{-1}(-\omega)]^*[\chi_c^{-1}(\omega_s)]^*\chi_b^{-1}(-\omega_s)} \right]. \tag{C.30}$$

Taking the next step of calculating the number of microwave actuated phonons in the mechanical mode helps simplify this equation significantly. The number of phonons in the mechanical mode is calculated as

$$\bar{n}_s(\omega_s) = \frac{1}{2\pi}\int S_{\hat{b}^\dagger\hat{b}}^s(\omega)d\omega, \tag{C.31}$$

such that

$$\bar{n}_s(\omega_s) = g_\mu^2 \kappa_{\mu,e} \left[\frac{|\bar{c}_{in}|^2}{[\chi_c^{-1}(\omega_s)]^*[\chi_b^{-1}(\omega_s)]^*\chi_c^{-1}(\omega_s)\chi_b^{-1}(\omega_s)} \right.$$
$$+ \frac{|\bar{c}_{in}|^2}{\chi_c^{-1}(\omega_s)[\chi_b^{-1}(-\omega_s)]^*[\chi_c^{-1}(\omega_s)]^*\chi_b^{-1}(-\omega_s)}$$
$$+ \frac{(\bar{c}_{in})^2}{\chi_c^{-1}(\omega_s)[\chi_b^{-1}(-\omega_s)]^*\chi_c^{-1}(\omega_s)\chi_b^{-1}(\omega_s)}$$
$$\left. + \frac{(\bar{c}_{in}^*)^2}{[\chi_c^{-1}(\omega_s)]^*[\chi_b^{-1}(\omega_s)]^*[\chi_c^{-1}(\omega_s)]^*\chi_b^{-1}(-\omega_s)} \right]. \tag{C.32}$$

Which, using the identity $\frac{a}{z^*} + \frac{a^*}{z} = \frac{2\text{Re}\{az\}}{|z|^2}$, further simplifies to

$$\bar{n}_s(\omega_s) = g_\mu^2 \kappa_{\mu,e} \left[\frac{|\bar{c}_{in}|^2}{|\chi_c^{-1}(\omega_s)|^2|\chi_b^{-1}(\omega_s)|^2)} + \frac{|\bar{c}_{in}|^2}{|\chi_c^{-1}(\omega_s)|^2|\chi_b^{-1}(-\omega_s)|^2} \right.$$
$$\left. + \frac{2\text{Re}\{(\bar{c}_{in}^*)^2\chi_c^{-1}(\omega_s)[\chi_b^{-1}(-\omega_s)]^*\chi_c^{-1}(\omega_s)\chi_b^{-1}(\omega_s)\}}{|\chi_c^{-1}(\omega_s)|^4|\chi_b^{-1}(-\omega_s)|^2|\chi_b^{-1}(\omega_s)|^2} \right]. \tag{C.33}$$

The terms containing susceptibilities with negative frequency arguments are termed counter-rotating, and cause the second and third terms in Eqn. C.33 to contribute negligibly to the final phonon number for signal near resonance frequency ω_s. The inverse susceptibilities of the first term, in contrast, become small when $\omega_s \approx \omega_m \approx \omega_\mu$, resulting in a non-negligible number of microwave-actuated phonons:

$$\bar{n}_s(\omega_s) = \frac{P_s}{\hbar\omega_s} \frac{g_\mu^2 \kappa_{\mu,e}}{\left[(\omega_m-\omega_s)^2 + \Gamma_m^2/4\right]\left[(\omega_\mu-\omega_s)^2 + \kappa_\mu^2/4\right]}. \tag{C.34}$$

where $|\bar{c}_{in}|^2 = P_s/\hbar\omega_s$ is the input microwave photon flux.